Gas-Phase Epoxidation of Ethylene and Propylene

Jason Gaudet

Dissertation submitted to the faculty of Virginia Polytechnic Institute and State University in partial fulfillment of the requirements for the degree of

Doctor of Philosophy

In

Chemical Engineering

S. Ted Oyama, Chairman

David F. Cox

Rick M. Davis

Brian E. Hanson

October 21, 2010

Blacksburg, Virginia

Keywords: Ethylene oxidation, Silver, Alumina, Silicon Carbide, Ethylene; Ethylene oxide, Propylene, Catalyst, TS-1, Au/TS-1, XANES, EXAFS, Raman

Gas-Phase Epoxidation of Ethylene and Propylene

Jason Gaudet

Abstract

Catalysts consisting of silver on α-Al_2O_3, α -SiC, and β-SiC supports were synthesized and tested for catalytic performance in the gas-phase direct oxidation of ethylene to ethylene oxide. For this study, which used no promoters, ethylene oxidation selectivity of SiC-supported catalysts ranged from 10 to 60% and conversion from 0-4.5%. Silicon carbide supported catalysts exhibited poor performance except for a surface-modified β-SiC-supported catalyst, which demonstrated conversion and selectivity similar to that of an α-Al_2O_3-supported catalyst. This Ag/β-SiC catalyst was further investigated with a kinetic study, and the reaction orders were found to be 0.18 with respect to ethylene and 0.34 with respect to oxygen. The kinetic results were consistent with Langmuir-Hinshelwood rate expressions developed from single-site and dual-site reaction mechanisms.

Gold nanoparticles on titanium oxide and titania-silica supports are active for the formation of propylene oxide by the oxidation of propylene with hydrogen and oxygen mixtures. This study investigates the effect of cyanide treatment on gold supported on titanosilicate zeolite supports (Au/TS-1). Catalysts treated with weak solutions of sodium cyanide resulted in preferential removal of small gold particles, while catalysts treated with strong solutions resulted in dissolution of the gold and re-precipitation as gold (+1)

cyanide. X-ray absorption spectroscopy demonstrated that catalysts which produce propylene oxide in the presence of hydrogen and oxygen mixtures had supported gold (+3) oxide nanoparticles of 3 nm size after synthesis, which were reduced to gold metal at reaction conditions. Samples treated with strong solutions of sodium cyanide resulted in supported gold (+1) cyanide particles of large size, 9-11 nm. These particles did not produce propylene oxide but, surprisingly, showed high selectivity toward propylene hydrogenation. Increasing gold (+1) cyanide particle size resulted in a decrease in hydrogenation activity.

TS-1 and Au/TS-1 surfaces were studied with laser Raman spectroscopy. Surface fluorescence was substantially reduced with a low-temperature ozone treatment, allowing observation of titanosilicate framework bands. Hydrocarbon vibrations are observed for TS-1 and Au/TS-1 under propylene. Density functional theory models indicated that propylene adsorbed to a metal site along the π bond would show a Raman spectrum very similar to gas-phase propylene except for out-of-plane C-H vibrations, which would be moved to higher energy. This adsorption spectrum, with out-of-plane vibrations shifted to higher energy, was observed for both TS-1 and Au/TS-1. Langmuir adsorption isotherms were generated for both TS-1 and Au/TS-1, and a scaling factor derived from propylene uptake experiments allowed these isotherms to be scaled to propylene coverage of titanium.

Lovingly dedicated to

Arthur F. and Yvonne Gaudet

Acknowledgments

I am very fortunate for the direction of my advisor, Dr. S. Ted Oyama, who has offered me invaluable guidance throughout my time at Virginia Tech, and given me opportunities both here and abroad to expand my understanding of oxidative catalysis and scientific research in general. I would also like to thank my committee members Dr. David Cox, Dr. Richey Davis, and Dr. Brian Hanson for their help throughout my graduate career.

I would also like to thank the many students and postdoctoral researchers in our lab, who have expanded my understanding and appreciation of the world and who have made my time at Virginia Tech both scientifically and culturally fulfilling, Specifically, I thank Corey Reed, Yong-Kul Lee, Yan Xi, Yunfeng Gu, Hankwon Lim, Travis Gott, Pelin Hacarlioglu, Haiyan Zhao, Phuong Bui, Samhun Yun, Dan Li, Dmitri Iarkov, and Sheima Jatib Khatib. Much of my work would not have been possible except for the administrative assistance of Diane Cannaday, and in the lab, critical electrical equipment design by Riley Chan and fantastic metal fabrication work by Michael Vaught.

I would also like to thank my colleagues Kyoko K. Bando, Juan Bravo, and Jiqing Lu, who were kind enough to guide me during my work at the National Institute of Advanced Industrial Science and Technology in Tsukuba, Japan.

Finally, I would like to thank my family, who have been a source of unwavering support, with most sincere gratitude to my parents, Tom and Kellie Gaudet, and my sister Caitlyn. Most of all, I thank my wife Laura, whose faith in me is my greatest source of strength.

Table of Contents

Chapter 3

Raman spectroscopic adsorption study

of TS-1 and Au/TS-1 under propylene

Chapter 4

Conclusions

List of Tables

List of figures

Chapter 1

Gas-phase partial oxidation of ethylene on a surface-modified Ag/β-SiC catalyst

1.1 Introduction

Ethylene oxide (EO) is an important commodity chemical that is primarily used to produce ethylene glycol (EG) and surface active agents such as nonionic alkylphenol ethoxylates and detergent alcohol ethoxylates [1]. Several dozen important fine petroleum and chemical intermediates are derivatives of EO, and it is therefore extensively used in applications such as washing/drying, electronics, pharmaceuticals, pesticides, textiles, papermaking, automobiles, oil recovery and oil refining. The worldwide consumption of EO in 2002 was 1.47 x 10^7 metric tons per year, making it the most utilized epoxide species. Usage was divided among North America, 10%; Western Europe, 27%; Japan, 20%; other Asia, 6%; and other regions, 3% [2].

EO is mainly produced by the direct oxidation of ethylene with air or oxygen in packed-bed, multitubular reactors with recycle [3]. Catalysts for EO production are generally composed of silver (10-20 wt%) supported on a low surface area (1-2 $m^2 g^{-1}$) α-Al_2O_3 support with alkali metal (500-1200 wppm) promoters [4,5,6], especially cesium [7,8,9] and sodium [7,10]. Fluoride [11], rhenium [12], and chlorine [13,14] are also used as promoters. Chlorine is commonly introduced by injecting ppm levels of dichloroethane or vinyl chloride to the reactant stream, which inhibits total oxidation of ethylene

[8,15,16,17,18,19,20]. An Ag/α-Al_2O_3 catalyst might be improved from 37% selectivity to 80% selectivity using a 2 ppm feed of 1,2-dichloroethane [21]. Selectivity is also improved with the introduction of carbon dioxide [22,23] or methane [24].

Low surface area aluminas are typical support materials, as performance is poor with high surface area [25]. Typical reaction conditions [4,26] are 10-35 atm, 230-280 ^oC with GHSV 1500-10000 h^{-1} and contact time 0.1-5 s. Conversion is typically 10% and selectivity about 85%. The space time yield of industrial EO production is given as 0.032-0.32 $g_{EO}\ h^{-1}\ (cm^3\ cat)^{-1}$ [26], 330 $kg_{EO}\ m^{-3}h^{-1}$ [11], 2-25 $lbs_{EO}\ ft^{-3}h^{-1}$ [27]. Given that the density of typical EO catalysts is about 45 lb ft^{-3} (0.72 g cm^{-3}) [4,**Error! Bookmark not defined.**], these values translate to a space time yield of about 44-440 $g_{EO}\ kgcat^{-1}\ h^{-1}$. Assuming full coverage of the support with silver with a site density of $10^{19}\ m^{-2}$, a turnover frequency (TOF) of 0.014-0.15 s^{-1} can be calculated. The development of new catalysts for ethylene oxide production is an important area of research [28]. Approaches taken include the investigation of silver alloys [27], the addition of promoters [29], and the use of new supports.

Silicon carbide is a desirable support due to its wear resistance and heat dissipation qualities. The formation of EO is slightly exothermic (25 kcal/mol), while the total combustion of ethylene and EO are highly exothermic (>300 kcal/mol). Catalysts with high thermal conductivity are preferred, as they limit undesired temperature gradients within the reactor bed [30] or, alternatively, permit the use of larger diameter reactor tubes. Silicon carbide has a nominal thermal conductivity of 490 W $m^{-1}\ K^{-1}$ and thermal diffusivity of 230 $m^2\ s^{-1}\ 10^{-6}$, while α-Al_2O_3 has a thermal conductivity of 36 W $m^{-1}\ K^{-1}$ and

thermal diffusivity of 12 m^2 s^{-1} 10^{-6} [31]. The desirable heat transport properties of silicon carbide have spurred the development of silicon carbide supports.

Silicon carbide exists in two common morphologies. The high temperature hexagonal α structure forms large particles with low surface area (~1 m^2 g^{-1}) and sharp, sheared edges. When exposed to air, the surface of α-SiC forms a passivation layer of up to 14 mol% SiO_2. The low temperature cubic β structure forms small, rounded particles with high surface area (10-20 m^2 g^{-1}) and its surface does not form an oxide layer [32]. The high surface area β-SiC form is of particular interest. It is understood that high surface area α-Al_2O_3 is a poor support, but if this does not necessarily hold for silicon carbide, so very high silver loadings may be possible.

To investigate the suitability of β-SiC as an ethylene oxidation support, silver catalysts were synthesized using supports of α-Al_2O_3, α-SiC, and β-SiC and tested for catalytic performance. The activity and selectivity of these catalysts were compared, and a β-SiC supported catalyst with a surface modification treatment (Ag/β-SiC-mod), the most active SiC supported catalyst, was selected for study at different gold loadings. Subsequently, a kinetic study was made on the most effective SiC-supported catalyst (36% Ag/β-SiC-mod) which produced parameters for orders of reaction and mechanistic rate laws.

1.2 Experimental

Catalysts were prepared by loading supports to 6, 12, 36, and 56 wt% Ag using a wet impregnation method at room temperature. Ethylene diamine, 11.7 g, (Wako Pure

Chemical Industry, Ltd, 99.0%) was dissolved in distilled/deionized water and stirred for 5 minutes, followed by 0.47 g anhydrous oxalic acid (Wako, 98.0%) and silver (I) oxide (Wako, 99.0%) (0.686 g Ag_2O for 6% Ag/support, 1.465 g Ag_2O for 12% Ag/support, 6.042 g Ag_2O for 36% Ag/support, and 13.671 g Ag_2O for 56% Ag/support). Following the complete dissolution of the silver (I) oxide, the solution was stirred for 1 h and 2.8 g ethanolamine (Wako, 99.0%) was added. The solution was stirred for another 1 h and 10 g support material was introduced, forming a thin slurry. After 3 h the slurry was dried in an oven at 120 ^{o}C for 3 h, and subsequently calcined in air at 360 ^{o}C for 3 h. The resulting material was ground to 22/44 mesh (0.36-0.68 mm) particles.

Supports used were α-Al_2O_3 (Sumitomo AKP-3000, 5 m^2 g^{-1}), a commercially available α-SiC standard (Strem, 2 m^2 g^{-1}, α-SiC-std), a commercially available β-SiC standard (Wako, 20 m^2 g^{-1}, β-SiC-std), and two low-oxidation 30 m^2 g^{-1} β-SiC supports developed by SICAT: a low porosity β-SiC (SB0403A, β-SiC-low) and a high porosity β-SiC (SB0403B, β-SiC-high). In addition, 6%, 12%, and 36% Ag on surface-modified β-SiC (30 m^2 g^{-1}, β-SiC-mod) were provided by SICAT and used as received.

Catalytic activity was measured in a differential flow reactor consisting of a 5 mm diameter quartz tube placed vertically in a furnace assembly. Temperature monitoring and control was through a RKC REX-P24 temperature controller, using a thermocouple centered within the catalyst bed. Feed gases used were ethylene (Takachiho Chemical, >99.8%), oxygen (Tomoe Shokai, >99.5%) and argon (Suzuki Shokan, >99.9997%), which were dried and regulated by mass flow controllers.

Each catalyst was pretreated in 30 cm^3 min^{-1} Ar for 0.5 h at 200 ^oC to remove water before the introduction of the reaction gases. Reaction temperatures from 200^oC to 280^oC were investigated. Testing conditions were 0.1-0.5 g catalyst and multiple $C_2H_4/O_2/Ar$ flowrates so as to maintain 30 cm^3_{NTP} min^{-1} total flowrate (gas hourly space velocity 1800 h^{-1}) at 101 kPa.

Products were analyzed using a dual-column gas chromatograph (Shimazu GC-14). Ethylene and EO were separated from the reactant stream using an Aligent FPAP column and quantified using a flame ionization detector (FID) while carbon dioxide and water were separated using an Aligent Porapak Q column and quantified using a thermal conductivity detector (TCD). Carbon monoxide and acetaldehyde were not detected under any conditions. Effluent was sampled every 0.5 h and it was determined that 1.5 h was sufficient to establish steady state. All reported data were taken at 2 h after setting test conditions. The carbon mass balance was checked periodically and all material was accounted for to within 3% after steady-state.

Results were calculated in terms of ethylene turnover frequency (TOF), conversion of ethylene (X_E), and selectivity toward ethylene oxide (S_{EO}), which were calculated as indicated in Eqns. 1.1-3 using the molar flowrate of ethylene in the feed ($F_{E,0}$), the molar flowrate of ethylene in the effluent (F_E), the molar loading of silver in the catalyst (y_{Ag}), the dispersion of silver (D), and the molar concentration in the effluent of EO (c_{EO}) and of CO_2 (c_{CO2}). The dispersion (Eqn. 1.4) was determined using Ag loading (x, wt%) and support surface area (A, m^2 g^{-1}), the derivation of which will be explained in the following sections.

Oxygen chemisorption was determined for the 36% Ag/β-SiC-mod sample by heating in flowing O_2 to 170°C and holding 1 h, followed by purging with He for 0.5 h and reduction in flowing H_2 for 1 h. The sample was again purged with He for 0.5 and dosed with oxygen.

$$TOF_E = \frac{F_{E,0} - F_E}{y_{Ag} D} \quad (1.1)$$

$$X_E = \frac{F_{E,0} - F_E}{F_{E,0}} \quad (1.2)$$

$$S_{EO} = \frac{c_{EO}}{c_{EO} + 1/2 c_{CO_2}} \quad (1.3)$$

$$D = 0.086\left(\frac{x}{100 - x} \times \frac{5583}{A}\right)^{-0.53} \quad (1.4)$$

Initial screening of catalyst supports was completed using 0.5 g catalyst at conditions of 10/5/15 cm^3_{NTP} min^{-1} $C_2H_4/O_2/Ar$, 101 kPa (33.7 kPa C_2H_4, 16.8 kPa O_2) and reaction temperatures from 180°C to 280°C. Subsequent testing of catalysts supported on a surface-modified β-SiC (β-SiC-mod) was made at the same flowrate and pressure, temperatures of 200-280°C, and amounts loaded in the reactor of 0.6 g 6% Ag/β-SiC-mod, 0.3 g 12% Ag/β-SiC-mod, and 0.1 g 36% Ag/β-SiC-mod, so that all tests were made on catalysts containing a total of 36 mg Ag. Finally, kinetic testing of 36% Ag/β-SiC-mod catalyst was performed on 0.5 g catalyst by varying the partial pressure of feed gases from 17 to 67 KPa and temperature from 240°C to 280°C, while maintaining total flowrate of 30

cm^3_{NTP} min^{-1} and pressure 101 kPa, for a total of nine separate combinations of reactants and temperature. Testing order was randomized, except for one data point that was repeated to test for catalyst deactivation. Throughout the course of the kinetic test the percent error for EO formation rate was approximately 6%.

Kinetic model parameters were based on the concentration of reactants (kPa) and formation rate of products (g h^{-1} g_{Ag}^{-1}). The formation rate of EO, combustion rate of ethylene, and the sum of these reactions were each independently fitted to linear approximations to determine rate order and activation energy. Single-site and dual-site Langmuir-Hinshelwood models were fit to the six data points at 240°C using a nonlinear Levenberg-Marquardt least-squares algorithm (OriginPro 8.1). Parameters were constrained to the range 0-1000 and initialized by values of 0.1-10.0, and fitting was accomplished by optimizing parameters such that the sum of squares (χ^2) value, defined in Eqn. 4 as the sum of squared error between the data and theory, reached a minimum. For each model, a variety of parameter initialization values was used to thoroughly explore the $\chi^2 = f(k, \alpha, \beta)$ function and increase the likelihood of finding a global χ^2 minimum. The quality of each fit could then be considered by the final value of χ^2 (Eqn. 1.5) and the coefficient of determination (R^2) (Eqn. 1.6). The sum of squared error χ^2 indicates the deviation of the model from the data, and decreases as the model and data more closely coincide. The coefficient of determination R^2 indicates the deviation of the model from the data, scaled by the total sum of squares, or alternatively, the χ^2 divided by the number of data points and the data variance. This deviation is expressed as the difference from 1, such that the model more closely fits the data as R^2 approaches 1.

$$\chi^2 = \sum_{i=1}^{n} \left(y_i^{\,data} - y_i^{\,theory}(x_i) \right)^2 \qquad (1.5)$$

$$R^2 = 1 - \frac{\sum_{i=1}^{n} \left(y_i^{\,data} - y_i^{\,theory}(x_i) \right)^2}{\sum_{i=1}^{n} \left(y_i^{\,data} - \frac{1}{n} \sum_{i=1}^{n} y_i^{\,data} \right)^2} = 1 - \frac{\chi^2}{N\sigma^{2,data}} \qquad (1.6)$$

Under the parameter restrictions already mentioned, all nonlinear models which converged presented R^2 values (88-92%) and χ^2 values (76-113) such that, mathematically, all models appear equally valid for the conditions tested.

1.3 Results

Ag dispersion was estimated by determining the surface density of Ag on the support and calibrating this with the surface density and dispersion of similar supported Ag catalysts. Ag atoms were assumed to form spheres of average radius r on the support, such that the average center-to-center distance between adjacent spheres was R (Fig. 1.1). Using this assumption, Eqn. 1.7 can be determined, which will be derived in detail in the next section.

$$\rho_{surf} = \frac{4}{3} \rho_{sphere} f_{pack} \frac{r^3}{(r+L)^2} \qquad (1.7)$$

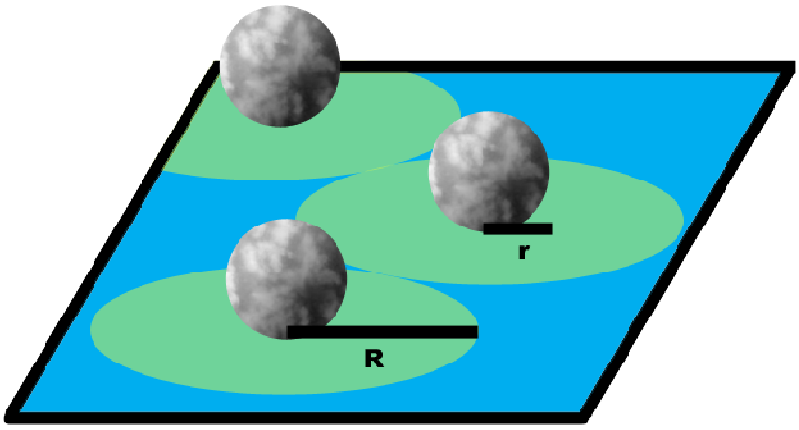

Figure 1.1. Ag spheres of radius r, spaced 2R apart on support surface.

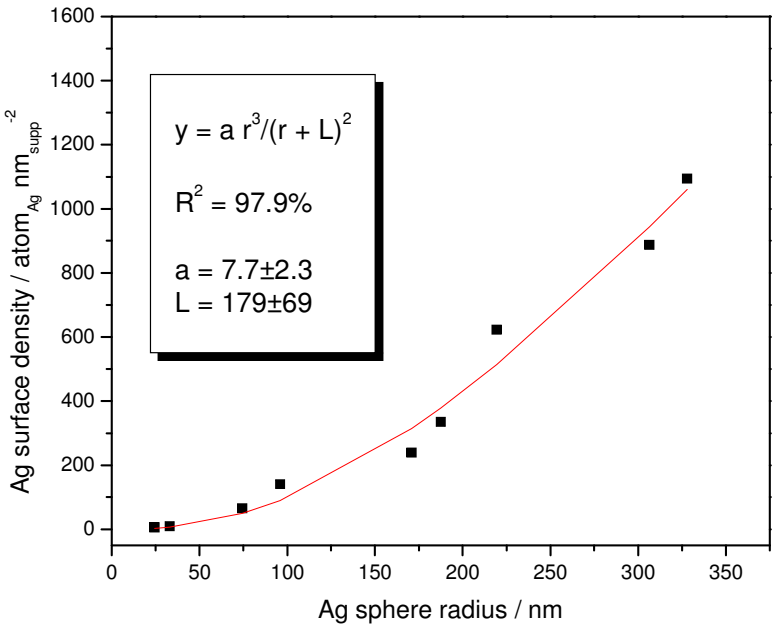

Figure 1.2. Correlation of Eqn. 1.7 to reference data

Eqn. 1.7 was fit to reference data (Fig. 1.2) [33,34] which validated the model and allowed, through further derivation, the determination of dispersion D via Ag loading (wt%) and support surface area ($m^2\ g^{-1}$) (Eqn. 1.8). Predicted oxygen uptake ($\mu mol_{O2}\ g_{cat}^{-1}$) was determined using Eqn. 9. Calculated surface properties are shown in Table 1.1.

$$D = 0.086\left(\frac{x}{100-x}\times\frac{5583}{A}\right)^{-0.53} \qquad (1.8)$$

$$Uptake = \frac{(x)(D)(10^6)}{(100)(107.87)(2)} \qquad (1.9)$$

Table 1.1. Calculated dispersion for samples

My samples	Ag Loading wt%	Support Surf Area $m^2\ g^{-1}$	D calculated	O_2 Uptake calculated $\mu mol_{O2}\ g_{cat}^{-1}$
6% Ag/α-Al2O3	6	5	0.0090	2.5
12% Ag/α-Al2O3	12	5	0.0060	3.3
36% Ag/SiC-low	36	30	0.0073	12.2
36% Ag/SiC-high	36	30	0.0073	12.2
56% Ag/β-SiC-std	56	20	0.0038	9.9
56% Ag/α-SiC-std	56	2	0.0011	2.9
36% Ag/β-SiC-mod	36	13	0.0047	7.8*
12% Ag/β-SiC-mod	12	13	0.0099	5.5
6% Ag/β-SiC-mod	6	13	0.0149	4.1

* 6.5 $\mu mol_{O2}\ g_{cat}^{-1}$ by experiment.

Ethylene turnover frequencies (TOF) of supported silver catalysts were calculated (Fig. 1.3). The 6% Ag/α-Al_2O_3 sample was the most active catalyst, and the 12% Ag/α-Al_2O_3 sample was nearly as active, with both samples producing TOFs in the range of 0.02-0.10 s^{-1}. Among the SiC supported samples the 36% Ag/β-SiC-mod sample was the most

active, with TOFs of 0.002-0.06 s^{-1} at 200-240 ^{o}C. The high-porosity 36% Ag/β-SiC-high and low-porosity 36% Ag/β-SiC-low catalysts were poor, and the high-porosity sample demonstrated significantly higher TOF at both 240^{o}C and 280^{o}C. The commercial standards, 56% Ag/α-SiC-std and 56% Ag/β-SiC-std, had very similar TOFs, however, they had a marked difference in ethylene oxide (EO) selectivity (Fig. 1.4). The 56% Ag/α-SiC sample had an EO selectivity of 60% while the 56% Ag/β-SiC sample had an activity of 8-18%. The 12% Ag/α-Al_2O_3 sample had a selectivity of 35-50% at ethylene conversion of 1-4.5%, while the selectivity of the 6% Ag/α-Al_2O_3 sample is 15-33% at ethylene conversion of 1-3%. The relationship between activity and selectivity of the 36% Ag/β-SiC-mod sample was very similar to that of the 12% Ag/α-Al_2O_3, and the performance of the 36% Ag/β-SiC-mod sample at 240^{o}C was nearly identical to that of 12% Ag/α-Al_2O_3 at 220^{o}C. The high-porosity 36% Ag/β-SiC-high and low-porosity 36% Ag/β-SiC-low catalysts produced only carbon dioxide.

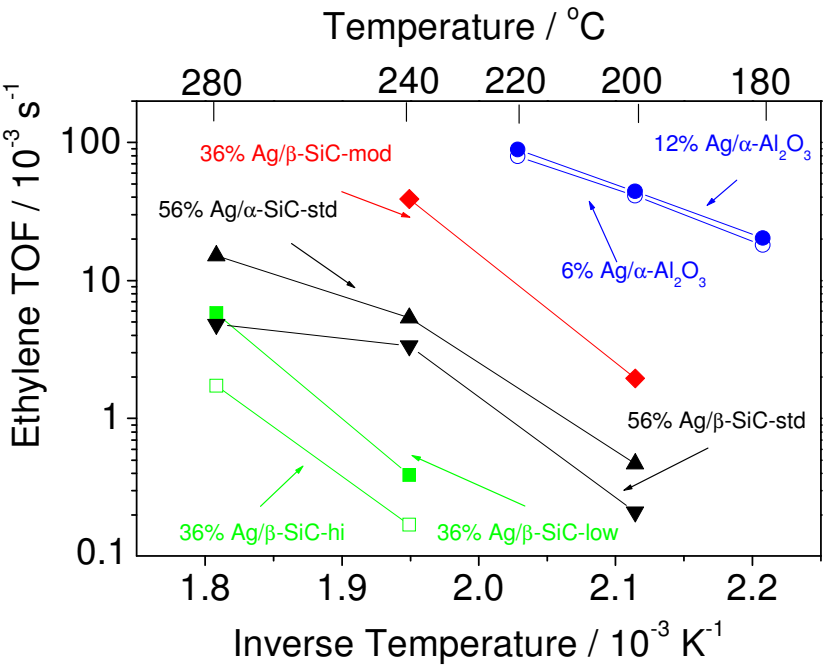

Figure 1.3. Ethylene turnover frequencies (TOF) of samples. Conditions are 10/5/15 cm^3_{NTP} min^{-1} $C_2H_4/O_2/Ar$, 101 kPa, 0.5 g catalyst. Samples are 6% Ag/α-Al_2O_3 (○),12% Ag/α-Al_2O_3 (●), 56% Ag/α-SiC-std (Strem standard) (▲), 56% Ag/β-SiC-std (Wako standard) (▼), 36% Ag/β-SiC-high (high porosity SICAT) (□), 36% Ag/β-SiC-low (low porosity SICAT) (■), 36% Ag/β-SiC-mod (surface modified SICAT) (♦).

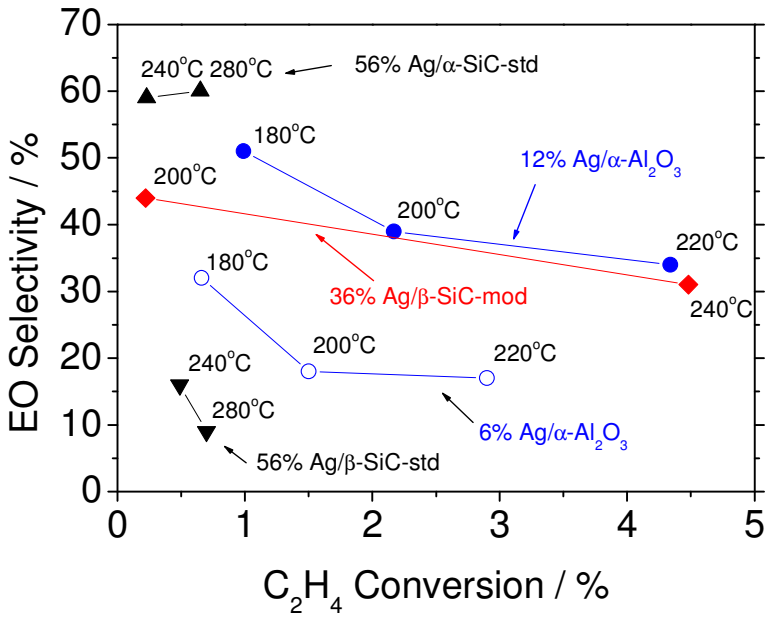

Figure 1.4. Ethylene oxide (EO) selectivity with respect to ethylene conversion. Conditions are 10/5/15 cm^3_{NTP} min^{-1} $C_2H_4/O_2/Ar$, 101 kPa, 0.5 g catalyst. Samples are 6% Ag/α-Al_2O_3 (○),12% Ag/α-Al_2O_3 (●), 56% Ag/α-SiC-std (Strem standard) (▲), 56% Ag/β-SiC-std (Wako standard) (▼), 36% Ag/β-SiC-mod (surface modified SICAT) (♦); 36% Ag/β-SiC-high (high porosity SICAT) and 36% Ag/β-SiC-low (low porosity SICAT) produce no EO and are not shown.

The surface modified β-SiC-mod support, which performed most similarly to α-Al_2O_3, was further tested at 6% and 12% Ag content, and a comparison made using amounts of catalyst containing 36 mg Ag (Fig. 5). All samples have TOFs on the order of 0.001 to 0.15 s^{-1}. The 12% Ag/β-SiC-mod sample has activity slightly above the 6% Ag/β-SiC-mod at 200-280°C, while the activity of the 36% Ag/β-SiC-mod sample is less than the others at 200°C but surpasses them at higher temperature. The 6% Ag sample produced no EO (Fig. 1.6). The 12% Ag sample had the highest EO selectivity of 37% at 200°C, but this selectivity decreases sharply with temperature and ethylene conversion. The 36% Ag

sample produced no EO at 200°C but had a 30% selectivity at 240 °C, which was reduced to 18% at 280 °C.

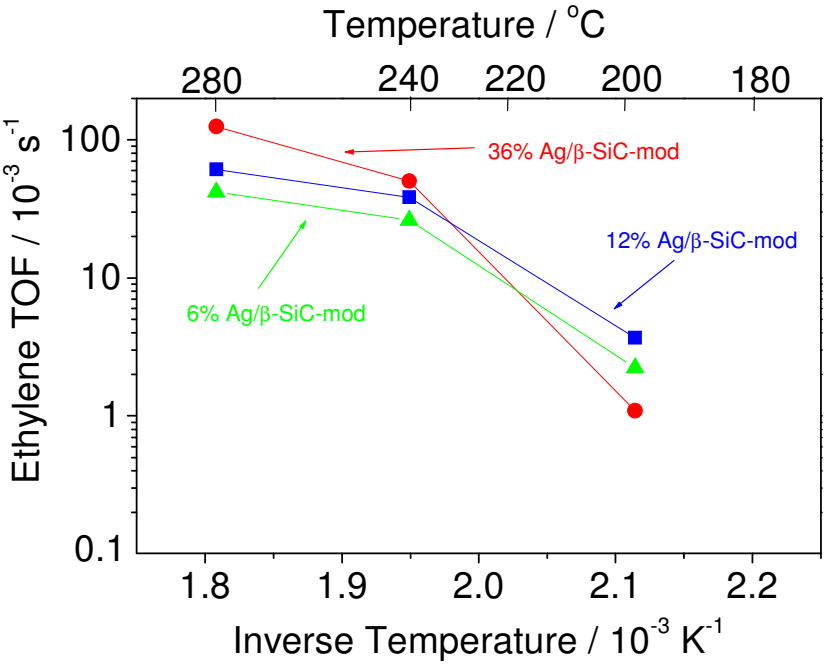

Figure 1.5. Ethylene turnover frequencies (TOF) of Ag/β-SiC-mod (surface modified SICAT) samples. Conditions are 10/5/15 cm^3_{NTP} min^{-1} $C_2H_4/O_2/Ar$, 101 kPa, and an amount of catalyst containing 36 mg Ag. Samples are 6% Ag/β-SiC-mod (▲), 12% Ag/β-SiC-mod (▲), and 36% Ag/β-SiC-mod (●).

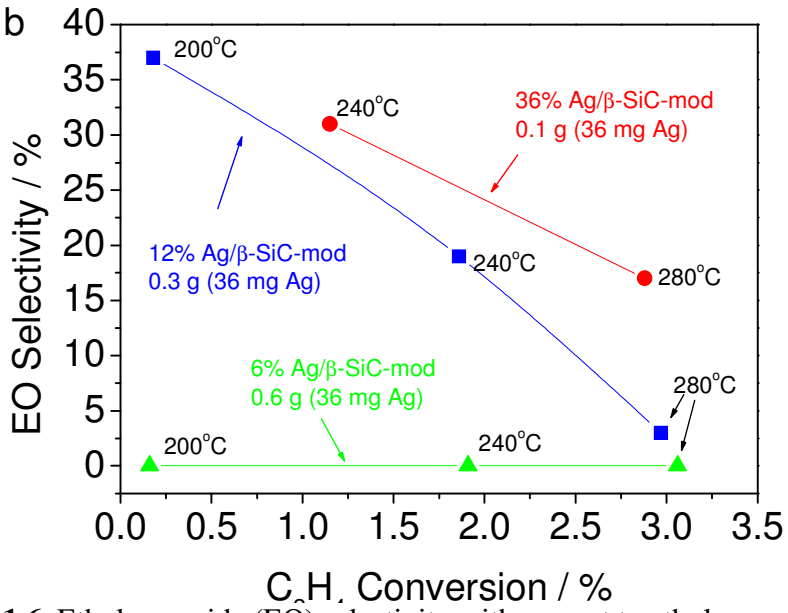

Figure 1.6. Ethylene oxide (EO) selectivity with respect to ethylene conversion. Conditions are 10/5/15 cm^3_{NTP} min^{-1} $C_2H_4/O_2/Ar$, 101 kPa, and an amount of catalyst containing 36 mg Ag. Samples are 6% Ag/β-SiC-mod (▲), 12% Ag/β-SiC-mod (▲), and 36% Ag/β-SiC-mod (●).

Table 1.2. 36% Ag/β-SiC-mod kinetic study conditions. All runs using 0.5 g catalyst, 30 cm^3_{NTP} min^{-1} total flow rate (balance Ar), 101 kPa.

Run	C_2H_4	O_2	T	Conv	Sel	Yield $g\ h^{-1}\ gAg^{-1}$	
	kPa	kPa	°C	%	%	EO	CO_2
1	33.33	16.67	240	6.13	30.4	122	279
2	33.33	33.33	240	7.36	34.5	167	316
3	33.33	66.67	240	7.94	37.7	196	324
4	33.33	16.67	240	6.37	29.5	123	294
5	66.67	16.67	240	3.48	33.6	154	303
6	16.67	16.67	240	13.05	28.1	120	307
7	33.33	16.67	240	5.57	31.2	114	251
8	33.33	16.67	260	8.29	14.8	80.7	463
9	33.33	16.67	280	8.53	0.6	3.43	555

To help investigate the nature of ethylene oxidation on β-SiC, a simple kinetic study of the 36% Ag/β-SiC-mod catalyst was performed (Table 1.2). The partial pressure of ethylene and oxygen were each varied from 17 to 67 kPa, and temperature was varied from 240°C to 280°C. The overall reactions considered were

$$C_2H_4 + ½\ O_2 \rightarrow C_2H_4O \qquad (1.10)$$

$$C_2H_4 + 3\ O_2 \rightarrow 2\ CO_2 + 2\ H_2O \qquad (1.11)$$

The reaction rates considered were the rate of EO formation r_{EO} (Eqn. 1.10), the rate of ethylene combustion r_C (Eqn. 1.11), and the sum of the two reactions (total ethylene consumption) $-r_E$) . All three reactions were approximated by a power rate law (Eqn. 1.12) which defines the rate as a function of activation energy E_A and some power of the inlet concentration of each reactant (all E_A and α, β different). The power rate law could be presented in a linear form (Eqn. 13) such that a linear least squares fit can be made.

$$r = \left(k_o e^{\frac{-E_A}{RT}} \right) (C_2H_4)^{\alpha} (O_2)^{\beta} \qquad (1.12)$$

$$\ln(r) = \ln(k_o) + \left(\frac{-E_A}{R} \right) \frac{1}{T} + \alpha \ln[(C_2H_4)] + \beta \ln[(O_2)] \qquad (1.13)$$

The reaction order with respect to ethylene (α) was 0.18 for ethylene oxidation, while combustion was zero order under these conditions (Table 1.3). The reaction order with respect to oxygen (β) was 0.34 for ethylene oxidation and 0.11 for combustion.

Overall ethylene conversion order was 0.19 with respect to oxygen, with a weak ethylene contribution. The apparent activation energy of total combustion was 47 kJ mol^{-1} but the apparent activation energy of EO was negative, as total oxidation was preferred with increasing temperature. The activation energy of 25 kJ mol^{-1} for ethylene conversion is consistent with similar work [35].

A series of mechanistic rate laws were fit to the same data using a three-dimensional surface fitting algorithm suitable for nonlinear equations. Five rate law models, including a power rate law, led to convergence (Table 4). The rate models in Table 1.3 will be discussed in detail in the following section.

Table 1.3. 36% Ag/β-SiC-SM calculated kinetic parameters for power rate law, fit to rate of EO production (r_{EO}), rate of ethylene combustion (r_C), and total rate of ethylene conversion ($-r_E$). Activation energy in kJ mol^{-1}, error given as 95% confidence interval. Linear regression using Levenberg–Marquardt algorithm (Polymath 5.1).

Parameter	r_{EO}		r_C		$-r_E$	
	Value	% R^2	Value	% R^2	Value	% R^2
α	0.18±0.08	91	0.00±0.03	31	0.05±0.05	71
β	0.34±0.06	98	0.11±0.04	94	0.19±0.05	97
E_A	-204±100	90	47.1±13.5	96	25.4±12.0	90

Table 1.4. Three-parameter rate laws determined using a nonlinear 3D surface fitting algorithm (OriginPro 8.1), [a] Pearson's chi squared test, [b] Coefficient of determination, [c] $g_{EO}\ h^{-1}\ g_{Ag}^{-1}\ kPa^{-(\alpha+\beta)}$, [d] $g_{EO}\ h^{-1}\ g_{Ag}^{-1}\ kPa^{-2}$, [e] kPa^{-1}, [f] kPa^{-2}, [g] $g_{EO}\ h^{-1}\ g_{Ag}^{-1}\ kPa^{-1.5}$, [h] $kPa^{-0.5}$, [i] $kPa^{-1.5}$. Error given as statistical standard error.

#	Model	Regression parameters			Quality of fit	
		k	α	β	χ^{2} [a]	% R^2 [b]
1	$r_{EO} = k(C_2H_4)^{\alpha}(O_2)^{\beta}$	27.7±8.1[c]	0.197±0.068	0.305±0.039	76	92
2	$r_{EO} = k\left(\frac{(C_2H_4)}{1+\alpha(C_2H_4)}\right)\left(\frac{(O_2)}{1+\beta(O_2)}\right)$	3.1±1.6[d]	0.140±0.083[e]	0.077±0.018[e]	109	89
3	$r_{EO} = k\frac{(C_2H_4)(O_2)}{1+\alpha(C_2H_4)+\beta(C_2H_4)(O_2)}$	1.3±0.7[d]	0.045±0.037[e]	0.006±0.003[f]	109	89
4	$r_{EO} = k\left(\frac{(C_2H_4)}{1+\alpha(C_2H_4)}\right)\left(\frac{(O_2)^{1/2}}{1+\beta(O_2)^{1/2}}\right)$	8.3±4.3[g]	0.141±0.084[e]	0.125±0.050[h]	113	88
5	$r_{EO} = k\frac{(C_2H_4)(O_2)^{1/2}}{1+\alpha(C_2H_4)+\beta(C_2H_4)(O_2)^{1/2}}$	5.5±2.7[g]	0.083±0.057[e]	0.014±0.008[i]	113	88

1.4 Discussion

The mechanical and heat transport properties of silicon carbide make this material a desirable support for supported silver ethylene oxidation catalysts when compared to α-Al_2O_3. Although high surface area α-Al_2O_3 is a poor support for ethylene oxidation, there is potential that the high surface area β-SiC phase may perform well, allowing higher silver dispersion and higher activity without loss of ethylene oxide (EO) selectivity. As will be discussed, while most Ag/SiC catalysts tested were poor, a catalyst of silver on surface-modified β-SiC (36% Ag/β-SiC-mod) exhibited performance similar to an α-Al_2O_3 supported catalyst. This Ag/β-SiC-mod catalyst was further studied at different silver loadings, and kinetic testing was used to determine reaction orders and rate laws.

Eqns. 7-8 illustrate a determination of Ag dispersion which will now be discussed in more detail. The surface density of silver on the support ($atom_{Ag}\ nm_{supp}^{-2}$) can be determined using Eqn. 1.14.

$$\rho_{surf} = \frac{x}{100-x} \times \frac{1}{107.87} \times \frac{6.022(10^{23})}{10^{18}} \times \frac{1}{A} = \frac{x}{100-x} \times \frac{5583}{A} \qquad (1.14)$$

Where x is the Ag loading of the catalyst (wt%) and A is the surface area of the support ($g\ m^{-2}$). Consider that Ag atoms form spheres on the surface, which may be distributed on the surface such that the average center-to-center distance between two spheres is the arbitrary length 2R, as illustrated in Fig. 1. The surface density of silver can then also be described as the number of silver atoms in each sphere divided by the area of

the support surrounding that sphere, and divided by the packing factor for the Ag on the surface. In this case, the surface density of Ag can also be described by Eqn. 1.15.

$$\rho_{surf} = \frac{V_{sphere}\rho_{sphere}}{A_{circle} f_{pack}^{-1}} = \frac{4/3\pi r^3 \rho_{sphere}}{\pi R^2 f_{pack}^{-1}} = \frac{4/3 r^3 \rho_{sphere}}{f_{pack}^{-1}(r+L)^2} \quad (1.15)$$

Assuming the distance between two Ag spheres on the surface, 2L, is constant, Eqn. 1.16 was be fit to the data using a nonlinear least squares fit.

$$\rho_{surf} = \frac{4}{3}\rho_{sphere} f_{pack} \frac{r^3}{(r+L)^2} \quad (1.16)$$

Using the density of bulk Ag of 58 atom nm^{-3}, packing is determined to be 0.1. The average distance between adjacent Ag spheres is determined to be 2L = 358 nm. Using Eqn. 1.17 it was possible to use Ag surface concentration ρ_{surf} ($atom_{Ag}$ nm_{supp}^{-2}) to determine Ag sphere radius r (nm).

$$\rho_{surf} \approx \frac{7.7 r^3}{(r+179)^2} \quad (1.17)$$

To simplify calculation, Eqn. 1.17 was approximated with an exponential function.

$$\rho_{surf} \approx 0.021 r^{1.87} \qquad (1.18)$$

The radius of an Ag sphere can be related to dispersion D [33] using Eqn. 1.19.

$$D = \frac{0.67}{r(nm)} \qquad (1.19)$$

Thus, combining Eqns. 1.14, 1.18, and 1.19 yields Eqn. 1.8, where dispersion D is wholly determined through Ag loading (wt%) and support surface area (m^2 g^{-1}).

$$D = 0.086\left(\frac{x}{100-x} \times \frac{5583}{A}\right)^{-0.53} \qquad (1.8)$$

As all testing was done at atmospheric pressure and without combustion-inhibiting promoters, the supported silver catalysts showed ethylene turnover frequencies (TOF) on the order of 10^{-6}-10^{-3} s^{-1} and EO selectivity of 30-40% for ethylene conversion of 2-4.5%. No undesirable partial oxidation product (i.e. acetaldehyde) was formed under any conditions. The Ag/α-Al_2O_3 catalysts showed the highest TOF and were also active at temperatures lower than the SiC catalysts (Fig. 1.1). Two supports, the SICAT β-SiC-high and β-SiC-low, were not active below 240°C and produced no ethylene oxide (EO) under any conditions (Fig. 1.2). The commercially available standards β-SiC-std and α-SiC-std show that while both SiC phases have similar ethylene conversion, the α phase is markedly

more selective toward EO. The surface-modified 36% Ag/β-SiC-mod catalyst has an ethylene conversion and EO selectivity most similar to 12% Ag/α-Al_2O_3, although the TOF of α-Al_2O_3 remained much higher. Reducing the silver loading of the Ag/β-SiC-mod catalyst to 12% increased the ethylene TOF (Fig. 3) but further reducing silver loading to 6% did not increase TOF further. Reducing silver loading to 6% also deactivated the catalyst for EO production (Fig. 4). Additionally, the 12% Ag/β-SiC-mod sample was less selective to EO than the 36% sample at the same temperature.

For the α-Al_2O_3 and β-SiC-mod samples decreasing gold loading increases TOF and decreases EO selectivity. For the commercial standards α-SiC-std and β-SiC-std the low surface area α-SiC-std support had the highest EO selectivity of all samples tested; this support also had the lowest surface area (2 m^2 g^{-1}) and highest silver loading per area.

The α-SiC-std, β-SiC-std, and β-SiC-mod supports had a TOF temperature dependence indicating a reduction of activation energy with increasing temperature in the range of 200-280^{o}C. This decrease in apparent activation energy was consistent with a Langmuir-Hinshelwood model, where the overall rate, and subsequently the apparent activation energy, is a combination of the kinetics of a rate-limiting surface reaction and the equilibrium between adsorbed species and the gas phase. At lower temperature, the overall rate was dominated by the surface reaction while at higher temperature the overall rate was primarily influenced by the adsorption of species to the catalyst. Conversely, the Ag/α-Al_2O_3 catalysts, which were tested at 180-220^{o}C, had a single activation energy in this range.

The highest EO production of all SiC catalysts were 36% Ag/β-SiC-mod and 12% Ag/β-SiC-mod. Although β-SiC-mod performed poorly compared to the alumina catalysts on a per-Ag basis, the performance of β-SiC-mod over all the other SiC catalysts was notable and prompted further investigation with a kinetic study of 36% Ag/β-SiC-mod (Table 1.1). The overall reactions considered were indicated previously as Eqns. 1.10-11.

A linear regression (Table 3) yielded rate constants given in Eqns. 1.5-7, with activation energies of -204 kJ mol^{-1} for ethylene oxidation, 47.1 kJ mol^{-1} for ethylene combustion, and 25.4 kJ mol^{-1} for the overall rate of ethylene consumption.

$$r_{EO} = k_{EO}(C_2H_4)^{0.18}(O_2)^{0.34} \quad (1.20)$$

$$r_C = k_C(O_2)^{0.11} \quad (1.21)$$

$$r_E = r_{EO} + r_C = k_E(O_2)^{0.19} \quad (1.22)$$

The combustion of ethylene and the conversion of ethylene were both zero order with respect to ethylene under these conditions. The formation of EO had a reaction order of 0.18 with respect to ethylene and 0.34 with respect to oxygen. A review of similar studies [36] indicated no consensus on rate orders; for both epoxidation and combustion the reaction order varied from 0-0.7 for ethylene and 0-1.5 for oxygen. This is consistent with a Langmuir-Hinshelwood model, as the mechanistic rate law is a rational function and the power rate law is an approximation as given in Eqn. 1.23.

$$x^n \approx \frac{x}{1+mx} \qquad (1.23)$$

Applying Eqn. 1.23 to the rate law for EO formation yields Eqn. 1.24.

$$r_{EO} = k\left(\frac{(C_2H_4)}{1+\alpha(C_2H_4)}\right)\left(\frac{(O_2)}{1+\beta(O_2)}\right) \qquad (1.24)$$

Eqn. 1.24 corresponds with a reaction sequence where the catalyst consists of two unique types of active sites, one which adsorbs only ethylene and one which adsorbs only oxygen. In this sequence, ethylene and oxygen each molecularly adsorb onto their active site, and the overall rate is commanded by the surface reaction of these intermediates. This dual-site mechanism, which assumes molecular adsorption of oxygen, is mathematically plausible but not necessarily physically plausible.

Many gases, including ethylene, do not adsorb onto clean silver, but will do so after silver has adsorbed oxygen [37], indicating that the EO reaction proceeds by oxygen adsorbing onto Ag, which activates adjacent Ag sites for ethylene adsorption. The adsorbed ethylene subsequently forms an oxametallacycle (-O-CH_2-CH_2-) on Ag [38,39] which is most likely anchored to a single Ag atom [9].

A likely mechanism [40] involves the dissociative adsorption of oxygen on a pair of vacant Ag sites (*), followed by ethylene adsorption and formation of an oxametallacycle, and then desorption of EO. A simple mechanism is given in Eqns 1.25-28.

$$O_2 + 2 * \leftrightarrow 2\ O* \quad (1.25)$$

$$C_2H_4 + * \leftrightarrow C_2H_4* \quad (1.26)$$

$$C_2H_4* + O* \leftrightarrow C_2H_4O* + * \quad (1.27)$$

$$C_2H_4O* \leftrightarrow C_2H_4O + * \quad (1.28)$$

A rate law can be developed from Eqns. 1.25-28 if it can be assumed that Eqn. 28 is a rate-determining step and Eqns. 1.10-12 are equilibrium-limited steps. A derivation presented in the appendix results in Eqn. 1.29.

$$r_{EO} = \frac{k(C_2H_4)(O)^{1/2}}{1 + \alpha(C_2H_4) + \beta(C_2H_4)(O)^{1/2} + \gamma(O)^{1/2}} \quad (1.29)$$

Eqn. 1.29 is a Langmuir-Hinshelwood rate law, where the terms in the numerator are the contribution of reactants in forming the reaction intermediate in the rate limiting step, and the terms in the denominator are the contribution of adsorbed species on the surface. The rate *k* and equilibrium constants α, β, and γ each have unique Arrhenius temperature dependencies, due to the activation energy of the rate determining step and the enthalpy of adsorption of the adsorbed species.

A nonlinear surface fitting algorithm was used to fit the kinetic data at 240°C to the power rate law (Eqn. 1.8) and Eqns. 1.24 and 1.29, as well as alternate versions of these latter equations so that both dissociative and molecular oxygen adsorption are considered (Table 4). A model based on Eqn. 1.29 converged only when γ=0, yielding models 3 and 5.

All models have essentially equal qualities of fit. The equations for the single site and two site model, and the dissociated and non-dissociated oxygen, were similar enough that are not mathematically distinguishable for this amount of data.

The power rate law model had the highest R^2 at 92% and lowest χ^2 at 76. The increased R^2 and decreased χ^2 are both expected, as the power rate law was the only model presented here that can be expressed as a linear function, with each dependent variable paired with its associated parameter. The four Langmuir-Hinshelwood rate laws, which are rational equations that cannot be linearized in such a way to isolate variable-parameter terms, all have R^2 values of 88-89% and χ^2 values of 109-113, indicating all four models have mathematically indistinguishable fit quality. Model 4, derived from Eqn. 1.19, is the model corresponding to the most likely mechanism, but the additional models which do not correspond to physically reasonable mechanisms are nonetheless good predictors of the data. The difference between molecular and dissociative adsorption of species may be especially difficult to identify through a reaction model, as the approximation noted in Eqn. 1.23 can be written in the form of Eqn. 1.30.

$$x^{(1/2)n} \approx \frac{x^{1/2}}{1+mx^{1/2}} \qquad (1.30)$$

1.5 Conclusions

Catalysts consisting of Ag on surface-modified β-SiC were studied alongside several α-SiC, β-SiC, and α-Al_2O_3 supports. A catalyst consisting of 36% Ag on β-SiC-mod outperformed all other SiC catalysts. A kinetic study was able to determine rate laws

for the formation of EO using power-law and Langmuir-Hinshelwood forms, finding the formation of ethylene 0.2 order with respect to ethylene and 0.3 order with respect to oxygen.

1.6 Appendix

A rate law can be developed from Eqns. 1.25-28 if it can be assumed that Eqn. 1.28 is the overall rate-determining step and Eqns. 1.25-27 are equilibrium-limited steps. If this is the case, the overall rate is simply the reaction rate of Eqn. 1.28.

$$r_{EO} = k(C_2H_4O^*) \tag{1.30}$$

The equilibrium constants for R1, R2, and R3 are K_1, K_2, and K_3, yielding the following:

$$(O^*) = K_1^{1/2}(O_2)^{1/2}(*) \tag{1.31}$$

$$(C_2H_4^*) = K_2(C_2H_4)(*) \tag{1.32}$$

$$(C_2H_4O^*) = K_3(C_2H_4^*)(O^*)(*)^{-1} = K_1^{1/2}K_2K_3(O)^{1/2}(C_2H_4)(*) \tag{1.33}$$

$$r_{EO} = kK_1^{1/2}K_2K_3(C_2H_4)(O)^{1/2}(*) \tag{1.34}$$

The concentration of vacant active sites (*) can be determined by considering that the concentration of all sites on the surface (L) is the sum of vacant and occupied sites.

$$(L) = (*) + (O^*) + (C_2H_4^*) + (C_2H_4O^*) \tag{1.35}$$

$$(L) = (*) + K_1^{1/2}(O)^{1/2}(*) + K_2(C_2H_4)(*) + K_1^{1/2}K_2K_3(C_2H_4)(O)^{1/2}(*) \tag{1.36}$$

$$(*) = \frac{(L)}{1 + K_1^{1/2}(O)^{1/2} + K_2(C_2H_4) + K_1^{1/2}K_2K_3(C_2H_4)(O)^{1/2}} \tag{1.37}$$

$$r_{EO} = \frac{kK_1^{1/2}K_2K_3(L)(C_2H_4)(O)^{1/2}}{1+K_1^{1/2}(O)^{1/2}+K_2(C_2H_4)+K_1^{1/2}K_2K_3(C_2H_4)(O)^{1/2}} \quad 1.38$$

$$r_{EO} = \frac{k(C_2H_4)(O)^{1/2}}{1+\alpha(C_2H_4)(O)^{1/2}+\beta(C_2H_4)+\gamma(O)^{1/2}} \quad 1.39$$

A two-site model can also be developed.

$$O_2 + 2\ *A \leftrightarrow 2\ O*A \quad 1.40$$

$$C_2H_4 + *B \leftrightarrow C_2H_4*B \quad 1.41$$

$$C_2H_4*B + O*A \leftrightarrow C_2H_4O*B + *A \quad 1.42$$

$$C_2H_4O*B \leftrightarrow C_2H_4O + *B \quad 1.43$$

$$r_{EO} = k(C_2H_4O*A)(O_2*B) \quad 1.44$$

$$(O*B) = K_1^{1/2}(O_2)^{1/2}(*B) \quad 1.45$$

$$(C_2H_4*A) = K_2(C_2H_4)(*A) \quad 1.46$$

$$(L_A) = (*) + (C_2H_4O*A) = (*A) + K_2(C_2H_4)(*A) \quad 1.47$$

$$(*A) = \frac{(L_A)}{1+K_2(C_2H_4)} \quad 1.48$$

$$(L_B) = (*) + (O*B) = (*B) + K_1^{1/2}(O_2)(*B) \quad 1.49$$

$$(*B) = \frac{(L_B)}{1+K_1^{1/2}(O_2)} \quad 1.50$$

$$r_{EO} = kK_1^{1/2} K_2 (L_A)(L_B)\left(\frac{(C_2H_4)}{1+K_2(C_2H_4)}\right)\left(\frac{(O_2)^{1/2}}{1+K_1^{1/2}(O_2)}\right) \quad 1.51$$

$$r_{EO} = k\left(\frac{(C_2H_4)}{1+\alpha(C_2H_4)}\right)\left(\frac{(O_2)^{1/2}}{1+\beta(O_2)}\right) \quad 1.52$$

1.7 References

[1] J.P. Dever, K. F. George, W.C. Hoffman, H. Soo, Ethylene oxide, in: Kirk-Othmer Encyclopedia of Chemical Technology, John Wiley & Sons, New York, 2001, pp. 632-673.

[2] J. Lacson, Ethylene oxide, in Chemical Economics Handbook, SRI International, Menlo Park, CA, Oct. 2003.

[3] J.P. Denver, K.F. George, W.C. Hoffman, H. Soo, Ethylene oxide, in: Kirk-Othmer Encyclopedia of Chemical Technology, John Wiley & Sons, New York, 2001, pp. 632-673.

[4] M.M. Bhasin, Catalyst composition for oxidation of ethylene to ethylene oxide, U.S. Patent 5,057,481, Oct. 15, 1991, assigned to Union Carbide Chemical and Plastics Technology Corp.

[5] W. Liu, A. Eliyas, L. Petrov, Influence of feed water vapour on the selective oxidation of ethylene over silver catalyst, Appl. Catal. 61 (1990) 265-274.

[6] Robert B. Grant, Richard M. Lambert, Alkali-metal promoters and catalysis: A single-crystal investigation of ethylene epoxidation on Cs-doped Ag(111), Langmuir 1 (1985) 29-33.

[7] R.P. Nielsen, J.H. La Rochelle, Ethylene oxide process, U.S. Patent 4,012,425, Mar. 15, 1977, assigned to Shell Oil Company.

[8] M. Atkins, J. Couves, M. Hague, B. H. Sakaniki, K. C. Waugh, On the role of Cs, Cl, and subsurface O in promoting selectivity in Ag/α-Al_2O_3 catalysed oxidation of ethene to ethene epoxide, J. Catal. 235 (2005) 103-113.

[9] S. Linic, M.A. Barteau, On the mechanism of Cs promotion in ethylene epoxidation on Ag, J. Am. Chem. Soc. 126 (2004) 8086-8087.

[10] James K. Lee, Xenophon E. Verykios, Rangasamy Pitchai, Support participation in chemistry of ethylene oxidation on silver catalysts, Appl. Catal. 44 (1988) 223-237.

[11] N. Rizkalla, Ethylene oxide catalyst, U.S. Patent 6,846,774 B2, Jan. 25, 2005, assigned to Scientific Design Co., Inc.

[12] A.M. Lauritzen, Ethylene oxide catalyst and process for the catalytic production of ethylene oxide, European Patent EP 0622015, May 4, 1988, assigned to Shell Int. Research.

[13] R.A. Von Santen, H.P.C.E. Kuipers, The mechanism of ethylene epoxidation, Advan. Catal. 35 (1987) 265-317.

[14] George H. Law, Henry C. Chitwood, Process of making olefin oxides, U.S. Patent 2,279,469, Apr. 14, 1942, assigned to Carbide and Carbon Chemicals Corporation

[15] C.T. Campbell, M.T. Paffett, The role of chlorine promoters in catalytic ethylene epoxidation over the Ag(110) surface, Appl. Surf. Sci. 19 (1984) 28-42.

[16] S.A. Tan, R.B. Grant, R.M. Lambert, Chlorine-oxygen interactions and the role of chlorine in ethylene oxidation over Ag(111), J. Catal. 100 (1986) 383-391.

[17] K.L. Yeung, A. Gavriilidis, A. Varma, M.M. Bhasin, Effects of 1,2 dichloroethane addition on the optimal silver catalyst distribution in pellets for epoxidation of ethylene, J. Catal. 174 (1988) 1-12.

[18] Emily A. Carter, William A. Goddard III, Chemisorption of oxygen, chlorine, hydrogen, hydroxide, and ethylene on silver clusters: A model for the olefin epoxidation reaction, Surf. Sci. 209 (1989) 243-289.

[19] Xenophon E. Verykios, Fred P. Stein, Robert W. Coughlin, Oxidation of ethylene over silver: Adsorption, Kinetics, Catalyst, Catal. Rev. Sci. Eng. 22 (1980) 197-234.

[20] Ostrovskii, Kul'kova, Lopatin, Temkin. Kinet. Catal. 3 (1962) 160.

[21] You-Sing Yong, Eric M. Kennedy, Noel W. Cant, Oxide catalysed reactions of ethylene oxide under conditions relevant to ethylene epoxidation over supported silver, Appl. Catal. 76 (1991) 31-48.

[22] Beulah Griffe, Ernest Blues, Dereck Bryce-Smith, Study of the effect of carbon dioxide on the catalytic properties of a silver catalyst in the oxidation of ethylene to ethylene oxide, Appl. Catal. 10 (1984) 303-312

[23] A. Eliyas, L. Petrov, Modelling of the inhibiting effect of carbon dioxide on the selective oxidation of ethene over silver catalyst, Appl. Catal. 62 (1990) 11-21.

[24] Yu Liu, Shikong Shen, Direct epoxidation of ethylene in a dilute reaction stream in oxidative coupling of methane, Appl. Catal. A: Gen. 121 (1995) 57-68.

[25] C.-F. Mao, M.A. Vannice, High surface area α-aluminas III. Oxidation of ethylene over silver dispersed on high surface area α -alumina, Appl. Catal. A: Gen. 122 (1995) 61-76.

[26] W.E. Evans, P.I. Chipman, Process for operating the epoxidation of ethylene, US Patent 6,717,001 B2, Apr. 6, 2004, To Shell Oil Company.

[27] J.R. Lockemeyer, Preparation of ethylene oxide and catalyst, U.S. Patent 5,929,259, Jul. 27, 1999, assigned to Shell Oil Company.

[28] S. T. Oyama, Rates, kinetics, and mechanisms of epoxidation: Homogeneous, heterogeneous, and biological routes, in: Mechanisms in Homogeneous and Heterogeneous Epoxidation Catalysis, S. T. Oyama, Ed., Elsevier, Amsterdam, 2008, pp. 3-99.

[29] H. Takada, M. Shima, Silver catalyst for production of ethylene oxide, method of production thereof, and method of production of ethylene oxide, U.S. Patent 6,103,916, Aug. 15, 2000, assigned to Nippon Shokubai Co., Ltd.

[30] J.V. Porcelli, Catal. Rev. Sci. Eng. 23 (1981) 151-162.

[31] Robert H. Perry, Don W. Green, Perry's Chemical Engineers' Handbook, seventh ed., McGraw-Hill, New York, 1997.

[32] Ch. Méthivier, B. Béguin, M. Brun, J. Massardier, J. C. Bertolini. Pd/SiC Catalysts: Characterization and Catalytic Activity for the Methane Total Oxidation, J. Catal. 173 (1998) 374-382.

[33] J. Lu, J.J. Bravo-Suarez, A. Takahashi, M. Haruta, S.T. Oyama, J. Catal. 232 (2005) 85.

[34] J. Lu, J.J. Bravo-Suárez, M. Haruta, S. Ted Oyama, App. Catal. A 302 (2006) 283.

[35] L. Petrov, A. Eliyas, D. Shopov, A kinetic model of steady state ethylene epoxidation over a supported silver catalyst, Appl. Catal. 18 (1985) 87-103.

[36] W.M.H. Sachtler, C. Backx, R.A. Van Santen, On the mechanism of ethylene epoxidation, Catal. Rev. Sci. Eng. 23 (1981) 127-149.

[37] Eric M. Cordi, John L. Falconer, Oxidation of volatile organic compounds on a Ag/Al_2O_3 catalyst, Appl. Catal. A: Gen 151 (1997) 179-191.

[38] G. Scott Jones, Manos Mavrikakis, Mark A. Barteau, John M. Vohs, First Synthesis, Experimental and Theoretical Vibrational Spectra of an Oxametallocycle on a Metal Surface, J. Am. Chem. Soc. 120 (1998) 3196-3204.

[39] Suljo Linic, Mark A. Barteau, Formation of a Stable Surface Oxametallocycle that Produces Ethylene Oxide, J. Am. Chem. Soc. 124 (2002) 310-317.

[40] Suljo Linic, Mark A. Barteau, Construction of a reaction coordinate and a microkinetic model for ethylene epoxidation on silver from DFT calculations and surface science experiments, J. Catal. 214 (2003) 200-212.

Chapter 2

Effect of gold oxidation state on the epoxidation and hydrogenation of propylene on Au/TS-1

2.1 Introduction

Supported gold has been a subject of great interest in heterogeneous catalysis since the discovery that nanosized gold particles oxidize carbon monoxide [1]. Heterogeneous gold catalysts show high activity, mostly for oxidation reactions [2,3,4], among which the oxidation of propylene to propylene oxide has received considerable attention [5,6,7,8,9,10]. Reviews are available on this subject [11] and on expoxidation mechanisms in general [12].

Catalysts consisting of gold nanoparticles supported on titanosilicate have demonstrated high selectivity in the oxidation of propylene to propylene oxide (PO) with hydrogen and oxygen [13,14,15]. Supports such as mesoporous Ti-TUD and nanoporous TS-1 are by themselves mild oxidation catalysts which can epoxidize propylene with hydrogen peroxide [16,17,18]. It is generally accepted that hydrogen and oxygen first react on the gold to form hydrogen peroxide, which then migrates to Ti centers to form hydroperoxide species that react with propylene to form PO and water [19,20,21].

The original objective of this study was to study finely dispersed gold in the propylene epoxidation reaction with hydrogen and oxygen to investigate a suggestion in the literature that 3-atom gold clusters might be active for the reaction [22,23]. Such small particle sizes had not been directly observed before. In order to obtain such clusters a procedure described in the literature was adopted which consisted of treating supported gold catalysts with sodium cyanide solutions [24]. This procedure was reported to produce atomically dispersed ionic gold species [25]. Instead, it was unexpectedly found that the cyanide treatment resulted in the dissolution of the gold and reprecipitation of larger Au (+1) cyanide particles. It was found that Au (+1) nanoparticles generated in this treatment were no longer active for propylene oxidation but instead were active for propylene hydrogenation. This study demonstrates that oxidizing supported gold nanoparticles to a (+1) state can fundamentally alter their catalytic behavior such that the gold takes on Pt-like behavior.

2.2 Experimental

2.2.1. Synthesis of Samples

The TS-1 zeolite was synthesized using a sol-gel method as described in the literature [21]. In a typical synthesis HCl (0.05 M, 30 g) (1.5 mmol) was stirred in an ice bath while 39.2 g (188 mmol) tetraethylorthosilicate (TEOS, Aldrich, 98%, batch 06526BC) were added dropwise, followed by 0.642 g (1.88 mmol) of titanium (+4) butoxide (Aldrich, lot 11131JE) in isopropyl alcohol. The solution was stirred for 10 minutes and 5.65 g (27.8 mmol) tetrapropylammonium hydroxide (TPAOH, 1.0 M in water, Aldrich, batch 09026ME) added, forming a gel. The gel was allowed to age for 2

h, and then was placed in a 373 K drying oven for 24 h. This material was subsequently autoclaved with 12.45 g (61.2 mmol) TPAOH at 448 K for 24 h, washed with 1 liter distilled water, and vacuum filtered. The material was dried at 393 K for 24 h, ground to a fine powder, and finally calcined in air at 773 K for 5 h. The yield based on TEOS was 93%. Powder x-ray diffraction (XDS 2000, Scintag Inc) was utilized to confirm the existence of TS-1 structure.

Gold nanoparticles were deposited on the TS-1 support using a deposition-precipitation (DP) method [26]. Gold (+3) chloride hydrate ($HAuCl_4.4H_2O$, Fluka, batch 456301/1) (30 mg, 0.0728 mmol, 14 mg Au) was dissolved in 100 ml distilled water and this solution was stirred and heated to 343 K. The solution had a pH of approximately 2.8 at this temperature (OAKTON Acorn pH-6), which was increased to 7.0 using NaOH before 1.00 g TS-1 powder was added. The solution was stirred for 1 h and then removed from heat and the solids were separated from the solution by centrifuging. The solids were re-suspended in water and centrifuged again. The remaining solids were removed and dried overnight under room-temperature vacuum without calcination.

2.2.2 Cyanide treatment

Gold was selectively removed from the samples by cyanide leaching [24]. Sodium cyanide (NaCN, 95+%, Aldrich, lot 05629PE) was dissolved in water to 0.05 wt% (0.010 M), 1.0 wt% (0.20 M), and 2.0 wt% (0.41 M), and NaOH was added to achieve a pH of 12.5. Au/TS-1 (2.0 g) was added to each 50 ml solution and stirred at room temperature for 1 h, and 100 ml water was added prior to vacuum filtration. The solids were again suspended in water and filtered, and this was repeated a total of 10 times to remove as much NaCN as possible, and the remaining solids were dried for 8 h

in room temperature vacuum. A solution of NaOH at 12.5 pH with no NaCN was used to produce a control sample. The samples were identified as Au-0.0 (no cyanide), Au-0.05 (0.05% cyanide), AuCN-1.0 (1.0% cyanide) and AuCN-2.0 (2.0% cyanide).

The gold content of the Au/TS-1 samples was determined using X-ray fluorescence spectroscopy (Rigaku ZSX mini) as well as inductively coupled plasma atomic emission spectroscopy (Spectro CirOS VISION, using aqua regia). An Au/TS-1 sample that was not further treated was determined to have a gold content of 1.12 wt%, indicating 80% of the gold in solution was deposited onto the catalyst. X-ray photoelectron spectroscopy (XPS) was obtained with a PHI-5500 spectrometer with Al K_α radiation (1253.6 eV) and referenced to the Si 2p line at 103.4 eV.

2.2.3 Transmission electron microscopy

High resolution transmission electron microscopy (TEM) images were obtained using a Philips CM200 FEG (200 kV) and a spherical aberration-corrected Titan (300kV). The Philips CM200 FEG has a point resolution of 2.0 Å, while the Titan utilizes a spherical-aberration corrector which can compensate for the delocalization of image details, which manifests itself as an extension of the perimeter of a sample beyond the actual surface in conventional TEM [27]. Particle size distributions were determined by selecting a representative image for each sample and measuring the diameter of all visible Au particles.

2.2.4 Reactivity testing

Catalytic activity was measured in a differential flow reactor consisting of a 5 mm diameter quartz tube placed vertically in a furnace assembly. Temperature monitoring and control was through a RKC REX-P24 temperature controller, using a thermocouple

centered within the catalyst bed. Feed gases used were propylene (Takachiho Chemical, >99.8%), oxygen (Tomoe Shokai, >99.5%) argon (Suzuki Shokan, >99.9997%) and hydrogen (Shimadzu OPGU-2100S hydrogen generator, >99.99%), regulated by mass flow controllers. All experiments used 0.30 g of catalyst, which was activated in reaction gases (10/10/10/70 $H_2/O_2/C_3H_6$/Ar, 35 cm^3_{NTP} min^{-1}, 7000 cm^3 h^{-1} $gcat^{-1}$) and heated from room temperature to reaction temperature at 0.5 K min^{-1}. The catalysts were held at 443 K for 2 h, then heated at 0.5 K min^{-1} to 473 K and held for a further 2 h.

The effluent was sampled every 0.5 h using a pair of two-column gas chromatographs. A FPAP column and flame ionization detector (FID) was able to separate and quantify propylene oxide, propionaldehyde, acetone, and acrolein, while a Gaskuropak column and FID was used to measure propylene and propane. A Porapak Q column and thermal conductivity detector (TCD) measured carbon dioxide, carbon monoxide and water, and a MS5A column and TCD was able to measure hydrogen and oxygen. Quantifiable amounts of propionaldehyde, acetone, acrolein, and carbon monoxide were not detected under any conditions.

2.2.5 X-ray absorption spectroscopy

In situ Au L_{III}-edge X-ray absorption spectroscopy (XAS) measurements were carried out at beamline NW10A of the Photon Factory in the Institute of Materials Structure Science, High Energy Accelerator Research Organization (PF-IMSS-KEK) in Tsukuba, Japan. A specially designed reactor cell and flow delivery system [28] was used to reproduce the pretreatment and reaction conditions used for catalyst screening. In situ measurements were taken at 443 K at 10 minute intervals using a step-scanning mode. Pretreatment and reaction conditions were monitored and controlled from outside the

radiation shielded hutch and all spectra were obtained in fluorescence mode using a solid state detector (SSD). The monochromater was calibrated against the L_{III} edge of a gold foil sample at E_0=11919 eV.

X-ray absorption near-edge structure (XANES) and extended x-ray absorption fine structure (EXAFS) were analyzed using IFEFFIT 1.2.8 [29]. For each spectrum, a pre-edge background was subtracted using a least-squares linear fit to E_0-150<E<E_0-30 eV, and the data was normalized to an edge jump of 1 using a least-squares cubic fit to E_0+150<E<E_0+763 eV. The white line area was calculated by shifting these background-subtracted and normalized spectra to the same E_0 as the bulk gold standard and integrating the area between the white line feature and bulk gold [30,31,32].

For EXAFS analysis, a post-edge background $\mu_0(E)$ was subtracted from each normalized spectrum and the wavevector k was substituted for energy E, yielding the EXAFS function $\chi(k)$. A Fourier transform on this k^3-weighted function in the range of 2<k<7 $Å^{-1}$ using a Kaiser-Bessel window with Δk=2 $Å^{-1}$ generated $\chi(R)$, the EXAFS function in real space. The background $\mu_0(E)$ was optimized using the AUTOBK algorithm [33], which fit a cubic spline [34] to the low-frequency oscillations in the spectrum such that the $\chi(R)$ function was minimized on the range 0<R<$R_{BKG,}$ using a number of knots equal to the number of independent points in this range to prevent overcorrelation. The value of R_{BKG} is the frequency below which oscillations in $\chi(k)$ are treated as noise, and the value of R_{BKG}=0.09 nm was determined to be optimal for all samples. The magnitude of the $\chi(R)$ was presented using a standard central atom phase correction so that the peaks in the Fourier transform more closely correspond with bond distances.

Additional information was extracted by fitting EXAFS $\chi(R)$ spectra to ab initio atomic models. Theoretical clusters of face-centered cubic (FCC) gold metal [35] and rhombohedral $NaAu(CN)_2$ [36] were generated using ATOMS [37] and the potential scattering paths of photoelectrons in these clusters were calculated with FEFF 6 [38,39]. A 12-fold 0.2885 nm Au-Au path was applied to the gold metal standard in the range of $0.16<R<0.34$ nm and the Au-0.0 and Au-0.05 samples after reaction on the range of $0.16<R<0.30$ nm, while a 2-fold 0.200 nm Au-CN path was applied to the AuCN-1.0 and AuCN-2.0 samples before and during reaction in the range of $0.11<R<0.21$ nm. The regression parameters studied were coordination number (N), path energy shift (ΔE), bond distance (R), and Debye-Waller factor (σ^2). As the amplitude correction factor S_0^2 and coordination number N are fully correlated in the single-shell EXAFS equations used in these fits, the amplitude correction factor could be fixed at $S_0^2=0.843$ for all samples so that N=12 for the bulk gold standard. The Au-0.0 and Au-0.05 EXAFS spectra each contained insufficient data to validate a four-parameter fit; therefore, ΔE was fixed at the ΔE of the gold standard, and σ^2 was set to the σ^2 of the gold standard with a linear temperature correction, i.e., $\sigma^2_{298\ K} = 1.49\sigma^2_{443\ K}$ [40]. The AuCN-1.0 and AuCN-2.0 samples before and after reaction were simultaneously fit to one value of ΔE, one independent value of the Debye-Waller factor (where $\sigma^2_{298\ K} = 1.49\sigma^2_{443\ K}$) and independent N and R for each set. Goodness of fit parameters were generated in accordance with current International X-ray Absorption Society (IXAS) standards. Models were selected which presented the smallest values of χ^2, R^2, and calculated error of regressed parameters.

To aid in XANES interpretation, molecular orbital analysis was carried out using Gaussian98 population analysis at the B3LYP/LANLDZ level. The structures studied were square planar $AuCl_4^-$, [41] linear $Au(CN)_2^-$, [42] and a proposed square planar $Au(CN)_4^-$. Bond distances used were Au-Cl 0.229 nm, Au-C 0.212 nm, and C-N 0.117 nm and bond angles were approximated as 180^o for Au-C-N (linear and square planar) and C-Au-C (linear) and 90^o for Cl-Au-Cl and C-Au-C (square planar).

2.3 Results

2.3.1 Catalyst characterization

Transmission electron micrographs (TEM) of the activated (post-reaction) catalysts (Fig. 2.1) show the presence of gold particles in all samples. All gold appears on the TS-1 surface as round particles. The particle size distribution is narrow for Au-0.0 and becomes progressively wider for Au-0.05, AuCN-1.0, and AuCN-2.0. The average particle size (Table 2.1) is 3 nm for the untreated Au-0.0 sample, which increases to 9 to 11 nm for the three cyanide treated samples. Treatment with progressively stronger cyanide treatment yields wider size distribution and reduced gold content. For the samples Au-0.0, Au-0.05, AuCN-1.0, and AuCN-2.0 the standard deviation of particle size grow from 1 nm to 2.5 nm, 5.6 nm, and 9.8 nm, and the gold content decreases from 0.81 wt% to 0.59 wt %, 0.29 wt%, and 0.24 wt%.

High resolution images of the particles in the Au-0.0 sample show that some have a complex multifaceted structure (Fig. 2.2) and a few of the particles appear to be twinned. Interplanar distances and angles (Fig. 2.3) indicate metallic gold for the Au-0.0 sample and $NaAu(CN)_2$ for the AuCN-1.0 sample. X-ray photoelectron spectroscopy

(XPS) indicates that the Au-0.0 sample and the AuCN-1.0 samples after reaction have oxidation states of Au (0) and Au (+1), respectively (Table 2.2).

Table 2.1. Gold content determined by x-ray fluorescence and gold particle diameter determined by transmission electron microscopy.

Sample	Cyanide treatment (wt% NaCN)	Gold content (wt%)	TEM particle diameter (nm)	
			Average	Standard Deviation
Au-0.0	0.00	0.81	3.0	1.0
Au-0.05	0.05	0.59	9.8	2.5
AuCN-1.0	1.00	0.29	9.1	5.6
AuCN-2.0	2.00	0.24	11.1	9.8

Table 2.2. X-ray photoelectron spectroscopy characterization of samples after reaction

Sample	Au $4f_{7/2}$ position /eV	Au oxidation state
Au-0.0	83.4	0
AuCN-1.0	85.5	+1
Au[a]	83.8 - 84.0	0
AuCN[a]	85.3	+1
AuCl[a]	86.2	+1
$NaAuCl_4$[a]	87.3	+3

[a] Reference values are obtained from C.D. Wagner, W.M. Riggs, L.E. Davis, J.F. Moulder, G.E. Muilenberg, Handbook of X-ray Photoelectron Spectroscopy, Perkin-Elmer Corp. Physical Electronic Div., Eden Prairie, Minnesota, 1995.

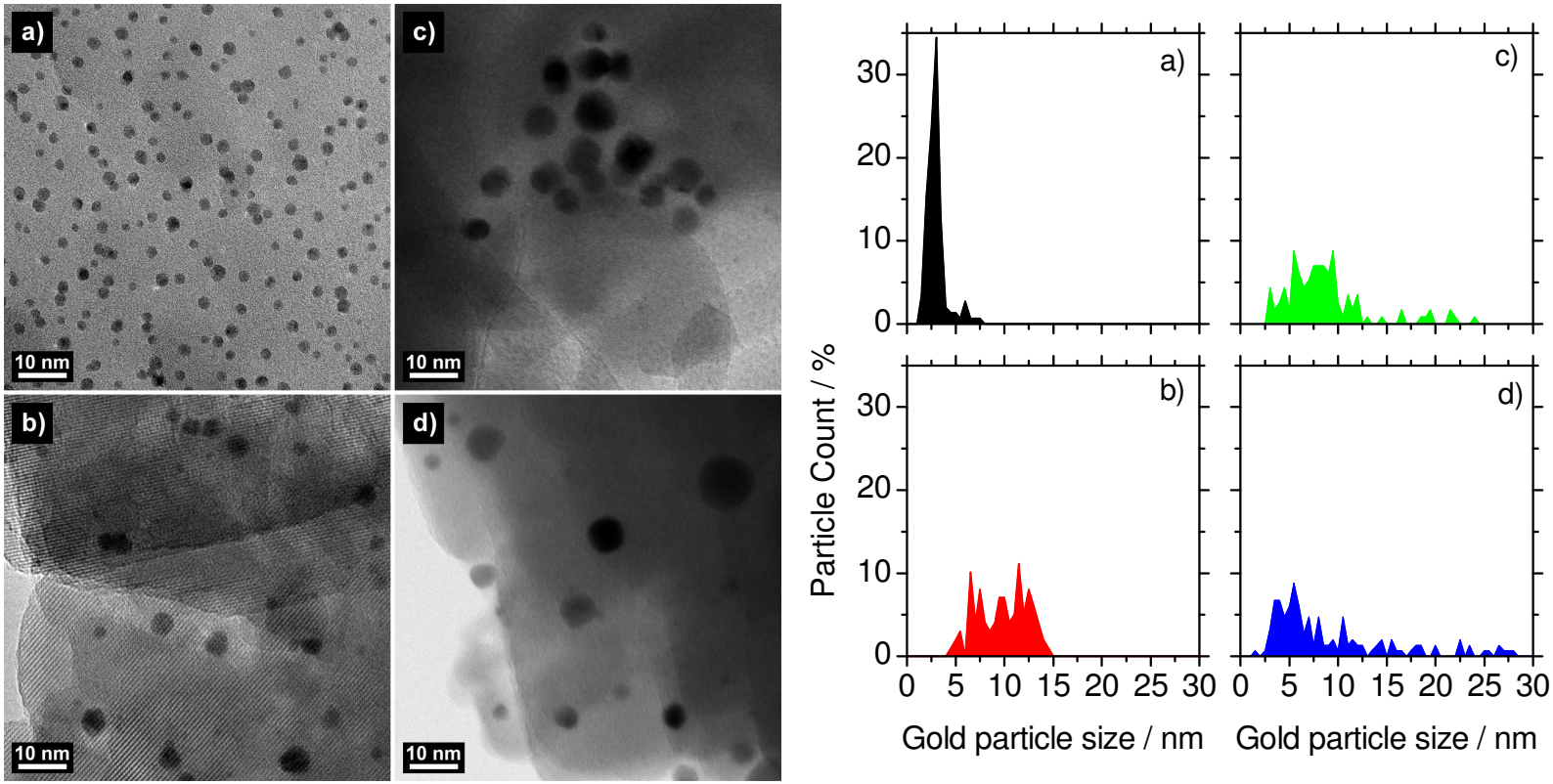

Figure 2.1. Transmission electron micrographs of Au/TS-1 catalysts after reaction (left) and calculated Au particle size distribution (right). a) Au-0.0, b) Au-0.05, c) AuCN-1.0, d) AuCN-2.0

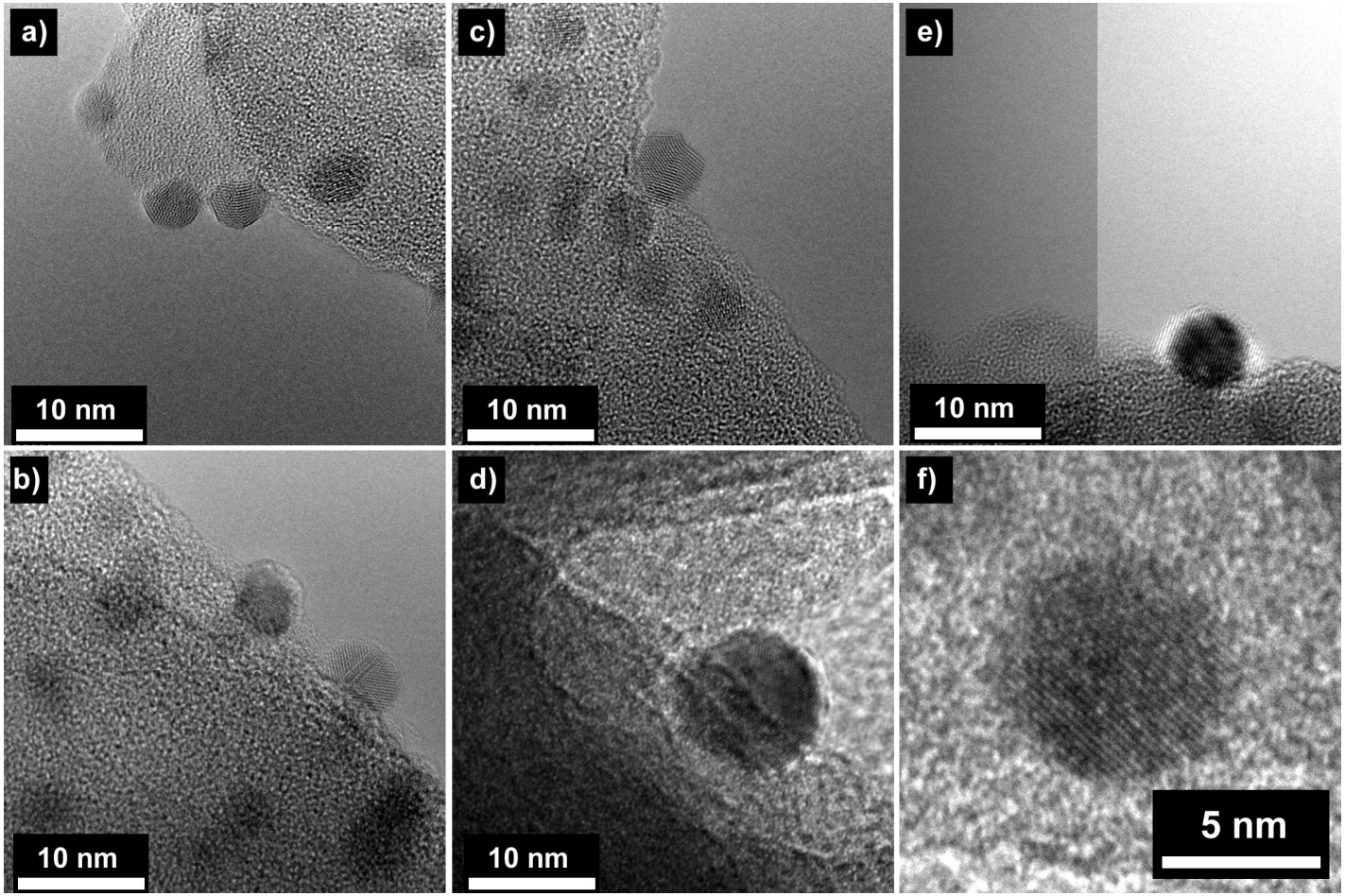

Figure 2.2. High resolution transmission electron micrographs of a)-c) Au-0.0, d) Au-0.05, e) AuCN-1.0, f) AuCN-2.0

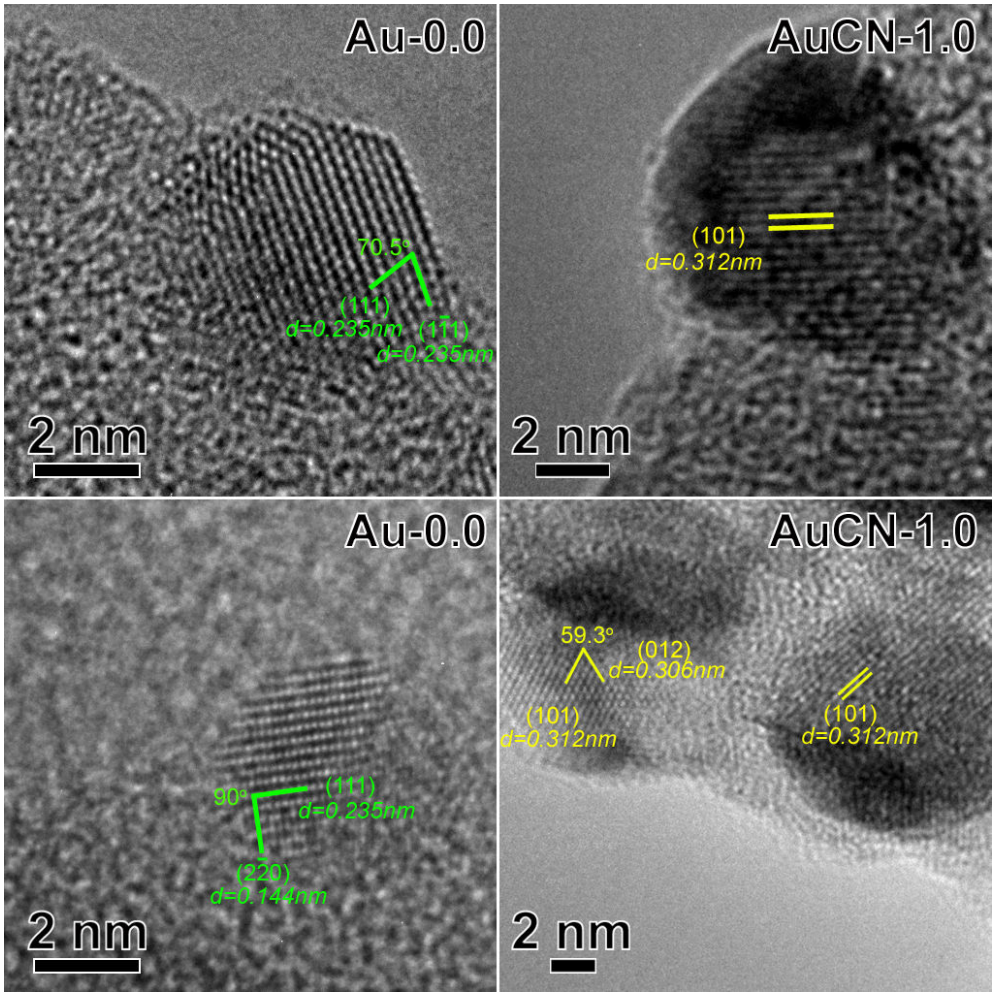

Figure 2.3. Interplanar distances and angles of gold metal and gold (+1) cyanide for Au-0.0 and AuCN-1.0 samples.

2.3.2 Reactivity Testing

Both the Au-0.0 and Au-0.05 samples produced mainly propylene oxide (PO) and propane (Fig. 2.4). At 443 K the Au-0.0 sample produced mainly PO and propane with little carbon dioxide. The Au-0.05 sample had significantly reduced activity and produced no carbon dioxide, but selectivity towards PO was very similar. Both samples demonstrated increased activity and selectivity towards PO at higher temperature. Increasing temperature to 473 K greatly reduced propane turnover frequency (TOF) for

the Au-0.0 sample from 0.0030 s^{-1} to 0.0016 s^{-1}, but had minimal effect on the propane activity of the Au-0.05 sample.

The AuCN-1.0 and AuCN-2.0 samples, which were treated with strong cyanide solutions, produced neither PO nor carbon dioxide. At 443 K the AuCN-1.0 sample produced water and propane while the AuCN-2.0 sample produced only propane. Increasing temperature to 473 K slightly reduced propane TOF of the AuCN-1.0 from 0.0038 s^{-1} to 0.0033 s^{-1}, and slightly increased propane TOF of the AuCN-2.0 sample from 0.0010 s^{-1} to 0.0012 s^{-1}.

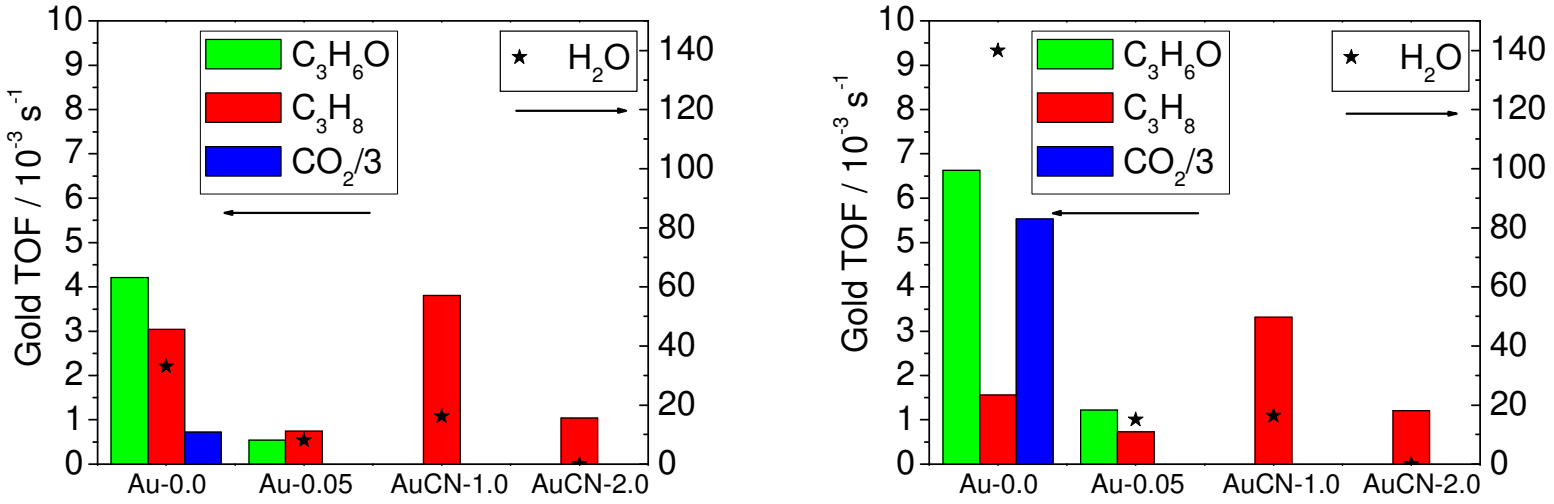

Figure 2.4. Turnover frequencies (TOF) ($mol_{product}$ mol_{Au}^{-1} s^{-1}) for catalysts at 443 K (left) and 473 K (right).

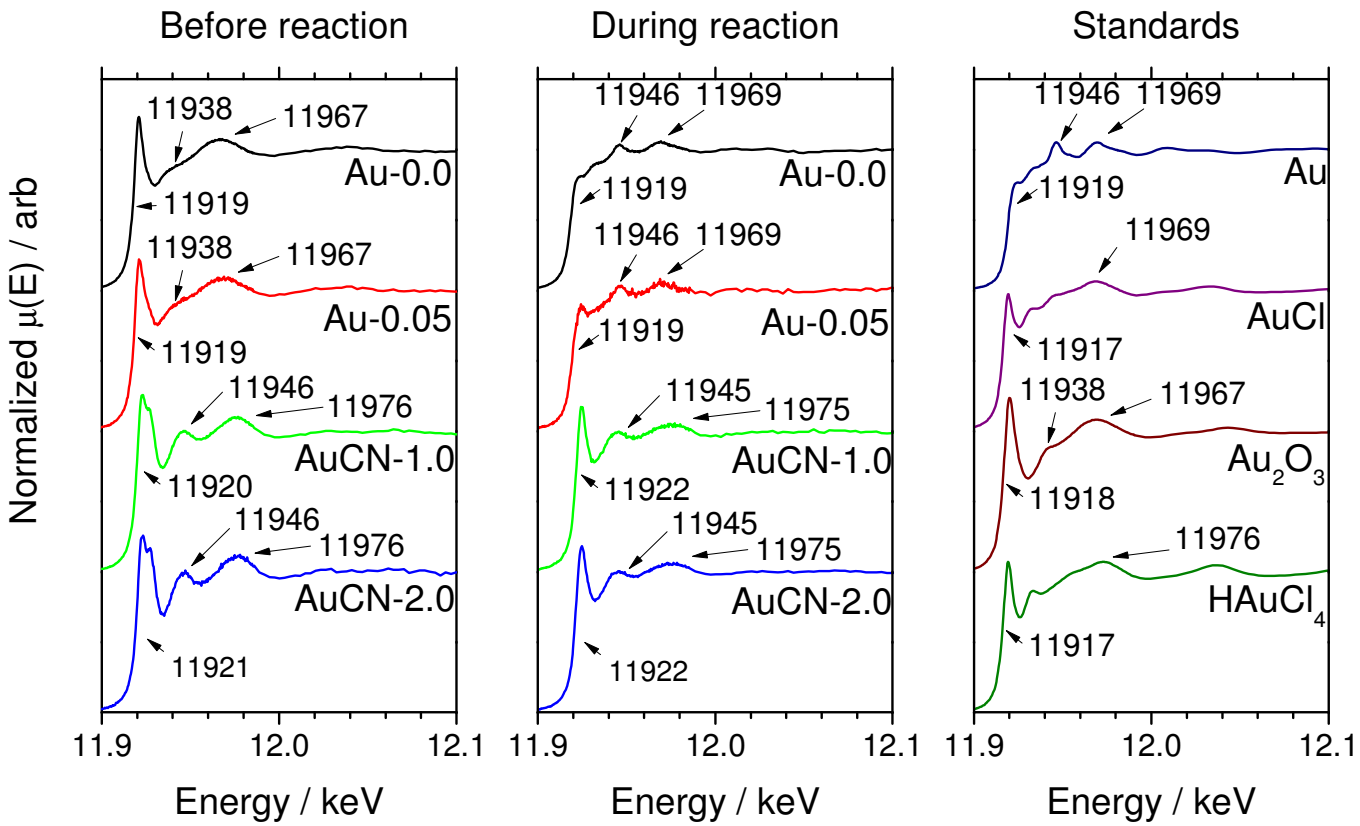

Figure 2.5. Au L_{III} x-ray absorption spectra. Background-subtracted and normalized XANES spectra of samples before reaction and during reaction, along with gold standards.

2.3.3 X-ray absorption near edge structure

In situ x-ray absorption near edge structure (XANES) spectroscopy of the gold L_{III} edge (11919 eV) was used to probe the electronic structure of the samples. Comparison of XANES spectra, normalized to edge jump, (Fig. 2.5) indicated the Au-0.0 and Au-0.05 samples before reaction (left panel) corresponded to Au_2O_3 (right panel), with an edge position at 11917 eV and a sharp peak known as the white line, followed by the main post-edge feature consisting of a wide adsorption peak at 11969 eV with a shoulder peak at 11938 eV. The Au-0.0 and Au-0.05 samples during reaction (middle panel) had metallic gold, with an edge at 11919 eV, and a dramatically reduced white line feature. In addition, both samples and the standard had two small post-edge features at 11946 and 11969 eV. The AuCN-1.0 and AuCN-2.0 XANES spectra are very similar before reaction (left panel) and during reaction (right panel), as both samples had edges at 11920-11922 eV, strong white lines, and post-edge features at 11945-11946 and 11975-11976 eV. These spectra do not match the standards measured, but correspond well to gold (+1) cyanide spectra reported by Kim [43] and Pantelouris [44]. Before reaction, the AuCN-1.0 and AuCN-2.0 white line features each had a shoulder peak which was not present during reaction.

To calculate the white line area, the spectrum of metallic gold was subtracted from each XANES spectrum presented in Fig. 2.5, with proper normalization of the edge jump and matching of the edge position. A comparative scale of white line areas was set up by assigning the white line area of metallic gold to 0 and that of gold (+3) oxide to 2.5 units. Using this scale, the white line areas (Fig. 2.6) of the Au-0.0 and Au-0.05 samples

were 2.3 and 2.5 units before reaction and 0.3 and 0.5 units during reaction, respectively. The white line areas of the AuCN-1.0 and AuCN-2.0 samples were 3.8 and 3.9 units before reaction and 2.1 and 2.3 units during reaction, respectively.

The large white line areas of AuCN-1.0 and AuCN-2.0 before reaction indicate d occupancy much lower than any standard tested, and this may be due to electron withdrawl by the cyanide ligands. An analysis of a XANES spectrum from the literature [43] carried out in the same manner as described here gives a white line area of gold (+1) cyanide of 2.1 units. This is consistent with the white line area during reaction of the AuCN-1.0 and AuCN-2.0 samples.

A detailed comparison of the near edge region of the AuCN-1.0 and AuCN-2.0 samples before and during reaction (Fig. 2.7, left and center panels) shows a reduction in the white line peak and increase in the post-edge trough for both samples. The same behavior is obtained when comparing gold (+3) chloride to gold (+1) chloride (Fig. 2.7, right panel).

Prior to reaction, the white line in both samples AuCN-1.0 and AuCN-2.0 is split into a doublet with 4 eV separation (Fig. 2.5, left panel; Fig. 2.7, left and center panels). Density functional theory (DFT) calculations (Fig. 2.8) show a gold 5d valance orbital split of 3.8 eV for a modeled $Au(CN)_4^-$ structure, 0.8 eV for $Au(CN)_2^-$ and 14.3 eV for $AuCl_4^-$.

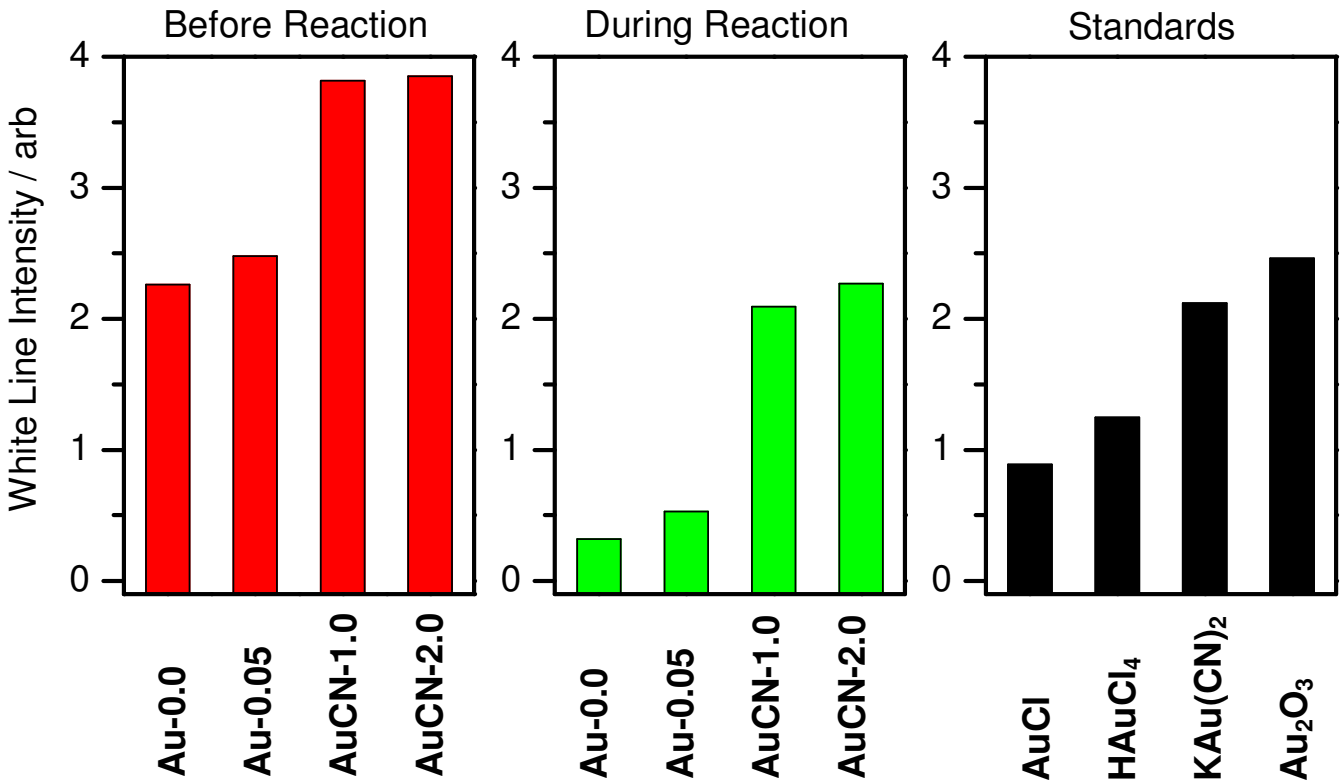

Figure 2.6. White line intensity of samples and standards. $KAu(CN)_2$ calculated from S.G. Kim, Y.-F. Hu, Y.M. Yiu, T.K. Sham, *J. Electron. Spectrosc. Relat. Phenom.* 144-147 (2005) 811-815.

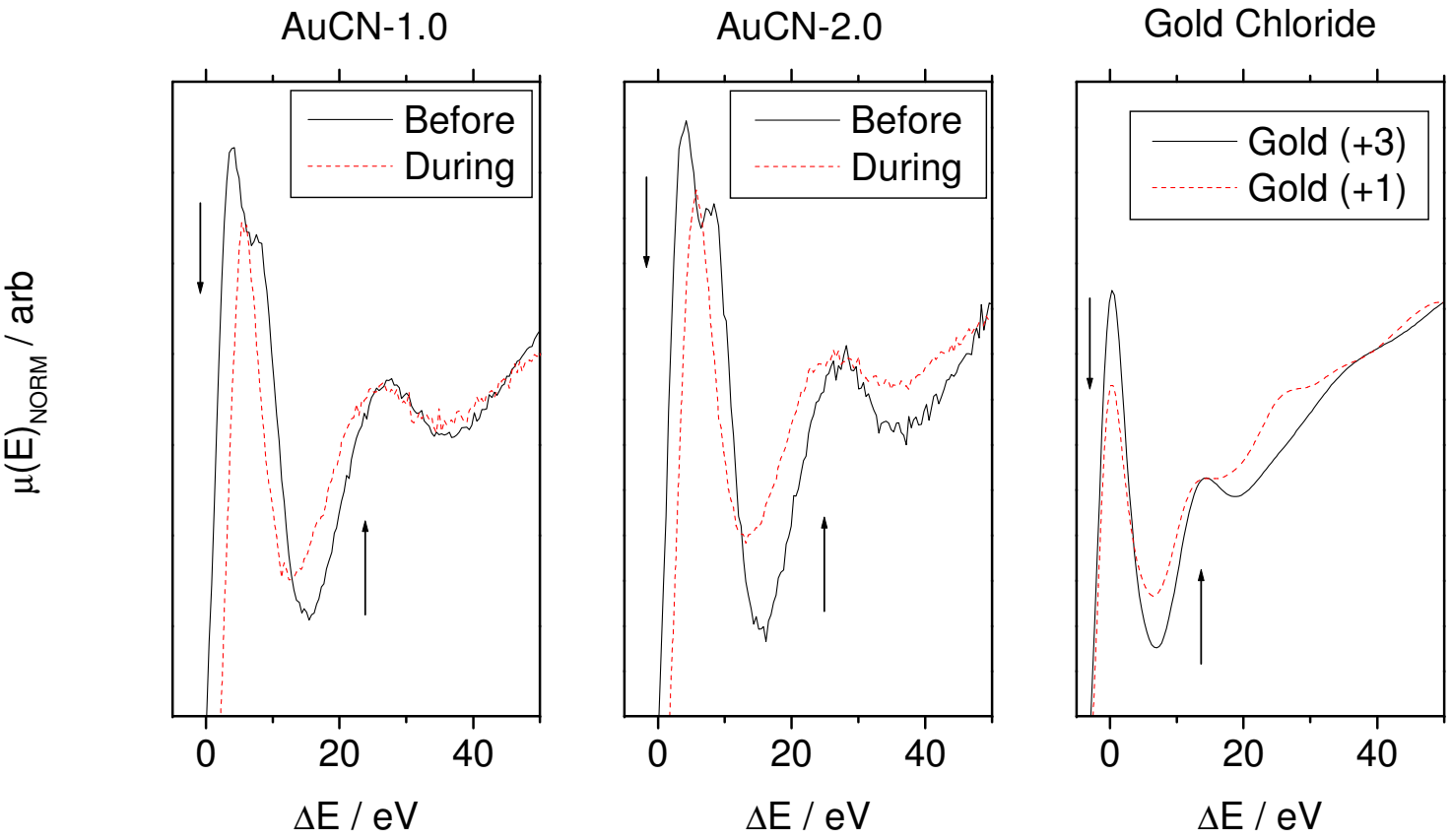

Figure 2.7. X-ray absorption spectra near edge detail for AuCN-1.0 (left) and AuCN-2.0 (center) before and during reaction, with comparison to gold (+1) chloride and gold (+3) chloride (right).

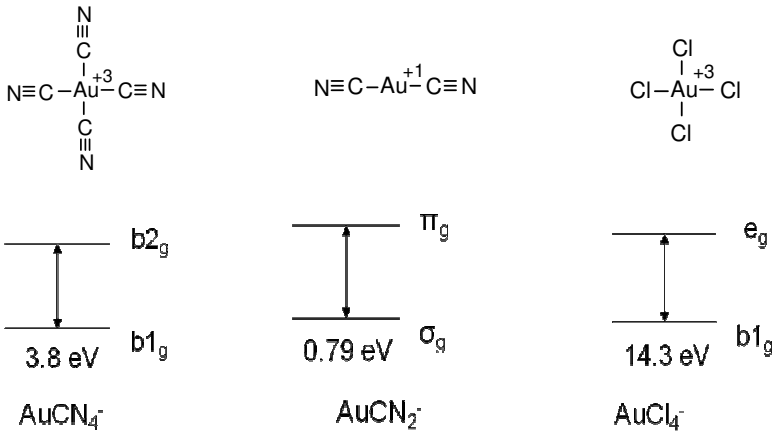

Figure 2.8. Gold 5d splitting for $Au(CN)_4^-$, $Au(CN)_2^-$, and $AuCl_4^-$ determined by density functional theory.

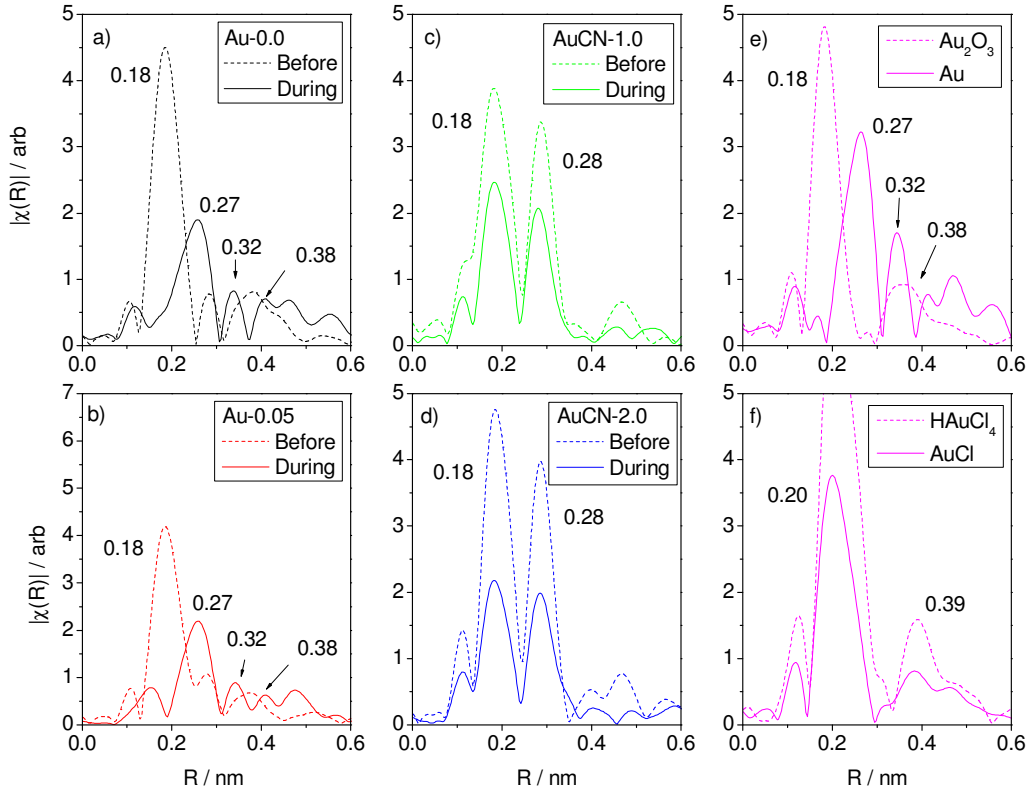

Figure 2.9. Phase-corrected |χ(R)| spectra of standards and Au/TS-1 catalysts. Samples are (a) Au-0.0, (b) Au-0.05, (c) AuCN-1.0, and (d) AuCN-2.0 at 298 K before reaction (dashed line) and 443 K during reaction (solid line). Standards are (e) gold foil (solid line) and Au_2O_3 (dashed line); (f) AuCl (solid line) and $HAuCl_4$ (dashed line).

Table 2.3. Extended x-ray absorption fine structure regression parameters for gold standard and samples

Sample	Rxn[a]	Bond	N_{idp}[b]	P[c]	χ^2[d]	R^2 (%)[e]	ε (nm)[f]	N[g]	ΔE (ev)[h]	R (nm)[i]	σ^2 (10^{-5} nm^2)[j]
FCC Au[k]	-	Au-Au	6	4	67	0.6	0.0024	12.0 ± 2.0	5.5 ± 1.1	0.2860 ± 0.0011	8.27 ± 2.10
Au-0.0	D	Au-Au	4	2	14	2.3	0.0068	9.4 ± 1.3	5.5 (set)	0.2813 ± 0.0022	12.30 (set)
Au-0.05	D	Au-Au	4	2	21	0.4	0.0024	10.8 ± 0.6	5.5 (set)	0.2846 ± 0.0009	12.30 (set)
AuCN-1.0	B	Au-C	12	10	35	1.5	0.0047	3.6 ± 1.4	7.3 ± 3.9	0.1978 ± 0.0031	1.24 ± 5.72
AuCN-2.0	B	Au-C	"	"	"	2.1	0.0047	4.6 ± 1.0	7.3 ± 3.9	0.1977 ± 0.0019	1.24 ± 5.72
AuCN-1.0	D	Au-C	"	"	"	2.2	0.0047	2.5 ± 1.0	7.3 ± 3.9	0.1976 ± 0.0040	1.85 ± 8.52
AuCN-2.0	D	Au-C	"	"	"	1.5	0.0047	2.2 ± 0.3	7.3 ± 3.9	0.1972 ± 0.0019	1.85 ± 8.52

[a]B=measurement before reaction, D=measurement during reaction; [b]number of independent data points; [c]number of fit parameters; [d]confidence limit; [e]residuals; [f]estimated measurement uncertainty in R; [g]Au coordination number; [h]energy correction factor; [i]bond distance; [j]Debye-Waller factor; [k]gold foil standard.

2.3.4 Extended x-ray absorption fine structure

The extended x-ray absorption fine structure (EXAFS) for the standards and samples are presented as $|\chi(R)|$ functions (Fig. 2.9). Prior to reaction, the Au-0.0 and Au-0.05 samples each have a narrow and intense peak at 0.18 nm and a wide feature at 0.38 nm, which is consistent with Au_2O_3 (Fig. 2.9, top right panel). During reaction, these samples develop a modest feature at 0.27 nm followed by a smaller peak at 0.32 nm, which is consistent with metallic gold. The AuCN-1.0 and AuCN-2.0 samples (Fig. 2.9, center panels) have EXAFS spectra very different from Au-0.0 and Au-0.05. Both AuCN-1.0 and AuCN-2.0 have strong, narrow features at 0.18 and 0.28 nm, which are more intense before reaction than during reaction. The presence of two peaks of similar intensity is not consistent with any of the standards tested (gold (0), gold (+1) chloride, gold (+3) chloride, gold (+3) oxide) (Fig. 2.9, right panels).

The EXAFS parameters determined by ab initio curve fitting are presented in Table 2.3. During reaction, the Au-0.0 sample has an Au-Au coordination number of 9.4 and an interatomic bond distance of 0.281 nm, while Au-0.05 has a coordination of 10.8 and bond distance of 0.285 nm. These values are less than those calculated for the gold standard, which has coordination of 12 and bond distance of 0.286 nm. Before reaction, the AuCN-1.0 and AuCN-2.0 samples have Au-C coordinations of 3.6 and 4.6, respectively. During reaction, the Au-C coordination is reduced to 2.5 and 2.2. Before and during reaction, both AuCN-1.0 and AuCN-2.0 have Au-C bond distances of 0.197-0.198 nm.

2.4 Discussion

In this work a method was used reported in the literature [24,45] which was claimed to form highly dispersed gold by leaching with cyanide solutions. The method was applied to gold supported on the titanosilicate, TS-1, a catalytic system that is known for the epoxidation of propylene with hydrogen/oxygen mixtures [5,6,7,8,9,13,14,15]. However, despite using a similar procedure (including a 2% sodium cyanide washing solution) the results differed substantially, and instead of producing atomically dispersed gold, precipitates of $NaAu(CN)_2$ were obtained.

Transmission electron micrographs show TS-1 particles as round-edged rectangular prisms approximately 300 to 1000 nm in size. Gold particles were found on the exterior surfaces of the microporous TS-1 support and were primarily between 1 and 7 nm but extended to tens of nanometers for the cyanide treated samples (Fig. 2.1). Cyanide treatment decreased the number of visible gold particles and increased their size. The Au-0.0 sample has a narrow particle size distribution with a peak at 3.0 nm (Table 2.1). The Au-0.05 sample retains some small particles but has a broader distribution centered around 10 nm. The AuCN-1.0 and AuCN-2.0 samples also have broad distributions with substantial numbers of large particles. It is evident that the cyanide treatment not only removes the smaller particles but also promotes growth of particles. Electron microscopy shows that the large particles are not agglomerates of smaller crystallites (Fig. 2.2). The interplanar distances and angles of the gold particles in the AuCN-1.0 sample indicate these particles are gold (+1) cyanide (Fig. 2.3).

Extended x-ray absorption fine structure (EXAFS), to be discussed later, confirms that the Au-0.0 and Au-0.05 samples start as gold (+3) oxide and are reduced to

gold (0) during reaction. The gold particles of the AuCN-1.0 and AuCN-2.0 samples are gold (+1) cyanide which has crystallized and deposited onto TS-1 during the cyanide treatment. In the case of Au-0.05 the particle size distribution and gold (+3) oxide x-ray absorption spectra suggest the larger particles were precipitated onto the surface during cyanide treatment.

The evidence presented earlier for the leaching of gold with cyanide solutions [24] was indirect, consisting of a lack of Au particles by scanning transmission electron microscopy (although no micrographs were shown) and x-ray photoelectron spectroscopy (XPS) evidence that showed that Au was primarily in the +1 (86%) and +3 states. In fact, the XPS measurements were repeated in the present study to check those results, and Au (+1) was duly observed (Table 2.2). This demonstrates that the previous XPS assignments could in fact have been indicative of gold cyanide, not highly dispersed gold.

Close examination of the small particles in the Au-0.0 sample reveals that many have a complex multifaceted structure with some consisting of twins (Fig. 2.2a-c). Thus, they show considerable amounts of defects, and this may be associated with their propensity to be dissolved in the cyanide solutions. The small particles (3.0 nm) that are formed in the cyanide treated samples tend not to be defective (Fig. 2.2d-f). As will be discussed, the defective nature of the small particles in the untreated sample may also be related to their high catalytic reactivity. Further structural confirmation can be gained by measuring interplanar distances and angles of representative Au-0.0 and AuCN-1.0 particles (Fig. 2.3). Metallic gold present on the Au-0.0 sample is identified by the interplanar distances of 0.144 nm and 0.235 nm and interplanar angles of 90^{o} and 70.5^{o},

while $Au(CN)_2^-$, present on the AuCN-1.0 sample, can be identified by interplanar distances of 0.306 nm and 0.312 nm and the interplanar angle of 59.3^o [46].

Treatment with cyanide reduces the gold content of the Au/TS-1 samples, with stronger cyanide solutions removing greater amounts of gold. With increasing severity of the treatment, there was a common trend of reduced gold content and wider particle size distribution (Table 2.1). While the weak cyanide treatment effectively shifted most gold particles from 2-4 nm (Au-0.0) to 7-14 nm (Au-0.05) without significantly changing their charge or structure, the strong treatments transformed all gold to gold cyanide. X-ray photoelectron spectroscopy (XPS) confirmed that gold was in a Au (0) state in the Au-0.0 sample and a Au (+1) state in the AuCN-1.0 sample (Table 2.2).

The Au/TS-1 samples in this study were studied in the reaction of propylene with H_2/O_2 mixtures, which is known to produce propylene oxide [47]. There is a striking change in selectivity for the samples prepared with different concentrations of cyanide in the leaching solution (Fig.4). The untreated sample with the small gold particles produces mainly PO. For the samples with increasingly strong cyanide washing, combustion is no longer evident and the production of PO and water decrease sharply. The production of propane is highest on the AuCN-1.0 sample, and the AuCN-2.0 sample produces propane but no water. Au-0.05 and AuCN-1.0 produce water but much less than Au-0.0, and the AuCN-1.0 demonstrates no temperature dependence for water production as well as no PO formation.

The reactivity results have certain mechanistic implications. Because carbon dioxide only appears where PO is a coproduct, and additionally, appears when PO TOF is 0.004 s^{-1} but not at 0.001 s^{-1}, carbon dioxide is most likely produced from PO under these

conditions. Further, water production increases tremendously with PO production, indicating that most water production is due to the decomposition of the same type of hydroperoxy intermediate responsible for producing PO, and that decomposition is more facile than the parallel epoxidation step. The AuCN-1.0 sample also produces water with little temperature dependence, indicating this water is formed by a different and much less active pathway.

It is generally understood that the role of gold is to form hydrogen peroxide from H_2 and O_2 [20,21,26]. It has been shown that gold nanoparticles are effective for this reaction [3]. From electron microscopy measurements it seems likely that the gold particles with surface defects are particularly active for hydrogen peroxide synthesis. The kinetics of hydrogen combustion, related to hydrogen peroxide synthesis, has been shown to require at least two types of gold sites [48]. It is also generally accepted that the hydrogen peroxide formed on gold migrates to the Ti sites in TS-1 to form hydroperoxide intermediates, which are the active epoxidizing agents. It has been shown that TS-1 is effective for PO formation with hydrogen peroxide [19]. Studies with in situ ultraviolet visible spectroscopy show the formation of the hydroperoxide, and measurements with in situ XANES demonstrate that they react at the same rate as the overall rate of reaction [20]. The observed products indicate the occurrence of the following reactions:

$$H_2 + O_2 \rightarrow H_2O_2 \qquad (2.1)$$

$$H_2O_2 + C_3H_6 \rightarrow C_3H_6O + H_2O \qquad (2.2)$$

$$C_3H_6O + 4\ O_2 \rightarrow 3\ CO_2 + 3\ H_2O \qquad (2.3)$$

$$H_2 + \tfrac{1}{2}\ O_2 \rightarrow H_2O \qquad (2.4)$$

The samples with larger gold particle size (Au-0.05) or oxidized gold (AuCN-1.0, AuCN-2.0) produce exclusively propane. Since the TS-1 support does not catalyze this reaction, the reaction must be taking place on the gold.

$$H_2 + C_3H_6 \rightarrow C_3H_8 \qquad (2.5)$$

The activity of the AuCN-2.0 sample is less than AuCN-1.0, indicating that when particle size is too large, the reactivity of gold cyanide decreases. The production of propane on nanoparticles of gold (+1) cyanide is an unusual discovery and will be addressed in greater detail.

In situ x-ray absorption near edge structure (XANES) spectroscopy of the gold L_{III} edge (11919 eV) was used to probe the electronic structure of the samples (Fig. 2.5). The discontinuity in x-ray absorbance which produces the L_{III} edge is due to the excitation of a $2p_{3/2}$ electron, and absorbance features in this range are due to excitation of these electrons to valence orbitals. In particular, the region in the immediate vicinity of the edge, known as the white line, is due to transitions from 2p levels to unoccupied 5d levels, such that increased intensity indicates greater 5d vacancies. The white line area is a useful quantity for determining gold oxidation state (Fig. 2.6) and here a relative scale is developed for comparing samples, where metallic gold has an area of 0 and gold (+3) oxide has an area of 2.5 units. Comparison indicates that the Au-0.0 and Au-0.05 samples before reaction had white line areas of 2.3 and 2.5 units, most similar to gold (+3) oxide, and during reaction had areas of 0.3 and 0.5 units, showing reduction to metallic gold. Similarly, the AuCN-1.0 and AuCN-2.0 samples before reaction had white line areas of 3.8 and 3.9 units, much higher than the areas of 2.1 and 2.3 during reaction, which are very similar to gold (+1) cyanide. It is proposed that prior to reaction the

AuCN-1.0 and AuCN-2.0 samples are primarily gold (+3) cyanide. As the white line is due to the presence of vacant 5d orbitals, the white line area is indicative of oxidation state only when comparing samples of similar electronic structure. It is not unexpected that linear $Au(CN)_2^-$ and tetrahedral Au_2O_3 have similar 5d vacancies, and similar white line areas, despite gold oxidation states of +1 and +3, respectively. A simple interpretation is that 5d electrons are promoted to orbitals of 6s character [49] in linear and square planar $Au(CN)_X$. In this interpretation the Au_2O_3 samples, including Au-0.0 and Au-0.05 before reaction, are in a [Xe] $4f^{14}$ $5d^8$ $6s^0$ state while gold (+1) cyanide is in a [Xe] $4f^{14}$ $5d^8$ $6s^2$ state, such that both structures have a d-vacancy of 2. Further, the AuCN-1.0 and AuCN-2.0 samples before reaction, indicated to be in a gold (+3) cyanide state, [Xe]$4f^{14}$ $5d^6$ $6s^2$, have a d-vacancy of 4 and, therefore, a larger white line area. Trivially, metallic gold, including the Au-0.0 and Au-0.05 samples during reaction, are in a [Xe] $4f^{14}$ $5d^{10}$ $6s^1$ state and have almost no d-vacancies.

The near edge region of the AuCN-1.0 and AuCN-2.0 samples show that, during reaction, the white line was reduced and the post edge trough was increased (Fig. 2.7, left and center panels), a difference that is also seen when comparing gold (+3) chloride to gold (+1) chloride (Fig. 2.7, right panel), and further evidence that these samples are reduced from Au (+3) to Au (+1) during reaction.

Close examination shows that the white line for these samples are split (Fig. 2.7, left and center panels). A white line multiplet on the AuCN-1.0 and AuCN-2.0 samples exists only before pretreatment. A core hole effect, where core-valance interaction allows core electron vacancies to reduce degeneracy in valance electrons, is precluded in gold L_{III} excitations due to the energy gap and charge screening of 2p and 5d shells [50].

Cyanide is a strong field ligand and a gold cyanide compound would be in a low spin state. A possibility was that the observed doublet was due to multiplet splitting, and this was investigated by carrying out density functional theory (DFT) calculations on square-planar $Au(CN)_4^-$, square-planar $AuCl_4^-$, and linear $Au(CN)_2^-$; specifically, the energy difference in the crystal field split of d-orbitals was examined (Fig. 2.8). For $AuCl_4^-$ this was a 14.3 eV ($b1_g \rightarrow e_g$), for $Au(CN)_2^-$ this was 0.79 eV ($\pi_g \rightarrow \sigma_g$), and for $Au(CN)_4^-$ this was 3.8 eV ($b1_g \rightarrow b2_g$). The large energy gap in the chloride complex favors transitions to the lowest level and produces no doublet, while the small gap in the $Au(CN)_2^-$ complex is below the energy resolution of XANES (1 eV) and results in a single line. The gap in the $Au(CN)_4^-$ complex, however, matches the energy split. The presence of these nondegenerate orbitals for gold (+3) cyanide is offered as a plausible reason for this gold L_{III} multiplet.

Further evidence regarding the character of these samples before and during reaction is provided by extended x-ray absorption fine structure (EXAFS). Bulk gold has a face centered cubic (FCC) structure (12-fold coordination) and a characteristic peak at 0.27 nm due to Au-Au nearest neighbors (Fig 2.9). Gold (+3) oxide, which has an orthorhombic structure with distorted tetrahedral gold centers (4-fold oxygen coordination) [51] has a sharp peak at 0.18 nm due to Au-O coordination and a wide feature at 0.36 nm. Both gold (+1) chloride (bent) and gold (+3) chloride (square planar) [41] have sharp Au-Cl features at 0.20 nm and a wider feature at 0.39 nm due to a Au-Au second shell. The difference in R position for the $|\chi(R)|$ feature of Au-O (0.18 nm), Au-Cl (0.20 nm), and Au-Au (0.27 nm) is large enough that they can be readily differentiated. The intensity of each first-shell $|\chi(R)|$ feature is proportional to the coordination of Au to

that specific absorbing atom; this can be seen for Au-Cl as the intensity of the 0.20 nm peak of 4-fold gold (+3) chloride is twice that of 2-fold gold (+1) chloride.

Fig. 2.9 shows that the Au-0.0 and Au-0.05 samples before reaction each have a narrow peak at 0.18 nm and a wide feature at 0.36 nm, confirming that these samples are gold (+3) oxide. During reaction, these samples develop the wide 0.27 nm Au-Au feature of metallic gold. The AuCN-1.0 and AuCN-2.0 samples, both before and during reaction, show features at 0.18 and 0.28 nm, which are assigned to Au-C and Au-N distances, respectively. The near-equal intensities of the first and second shells are characteristic of photoelectron focusing in a linear molecule [52], so that the AuCN-1.0 and AuCN-2.0 species before and after reaction can be identified as $Au(CN)_X$. The reduction of intensity during pretreatment indicates a significant decrease in coordination. Gold (+1) cyanide commonly exists as linear $Au(CN)_2^-$ anions, which form rhombohedral stacks with alternating layers of cations [42], although a -Au-C-N-Au-C-N- crystal structure may also exist [53,54]. Ab intio EXAFS fitting (Table 2.3) indicates a coordination of Au-C of 4 before reaction and 2 during reaction, which provides additional evidence that AuCN-1.0 and AuCN-2.0 are in a gold (+3) cyanide state before reaction and a gold (+1) cyanide state during reaction.

It is generally agreed that neutral gold nanoparticles supported on TS-1 produce a hydroperoxide intermediate responsible for propylene oxidation [55]. The hydrogenation of crotonaldehyde on Au/Fe_2O_3 is believed to occur on metallic gold, based on XANES edge measurements before reaction, but the signal was extremely low and could not be used to rule out oxidized Au in the periphery of the 5 nm particles [56]. Indeed, Au on a less reducible Al_2O_3 support was found to be less active. An early study on the

hydrogenation of propylene on Au/SiO_2 and Au/MgO found good activity only when the sample was exposed to molecular oxygen, suggesting that oxidized gold was active for hydrogenation. Isotopic exchange between $^{16}O_2$ and $^{18}O_2$ did not occur, indicating the formation of adsorbed peroxidic oxygen [57].

Here it is demonstrated that gold (+1) cyanide nanoparticles supported on TS-1 produce propane and do not oxidize propylene. Gold (+1) cyanide as a nanoscale heterogeneous hydrogenation catalyst is novel, but catalytic behavior of Au (+1) nanoparticles has been established in the literature. Supported nanoscale gold in an oxidized state was found to be active for CO oxidation [58], selective oxidation of alcohols [59], and water gas shift. Supported gold nanoparticles have not been as extensively studied as a hydrogenation catalyst [60]. Gold in a metallic state was found active for the selective hydrogenation of 1,3-butadiene [55] and acetylene [61], along with the reduction of NO_X [62]. A DFT study of atomic gold supported on zirconia indicated Au (+1) was active for 1,3-butadiene hydrogenation [63]. An experimental study of Au/ZrO_2 for 1,3-butadiene hydrogenation and CO oxidation found that gold with a higher ratio of Au (+3)/Au (0), as determined by Au 4f XPS, was more active for both hydrogenation and oxidation [64]. A study of an atomically dispersed Au complex found good activity in ethylene hydrogenation and evidence from XANES of a Au (+3) species [65]. An initial report [66] for epoxidation of propylene on Au/TiO_2 found the formation of propane on small Au particles and suggested that oxidized gold in the periphery of the particles was responsible for the hydrogenation. It was noted that the gold had platinum-like behavior, a view that is echoed here, with the specification that it is Au (+1).

However, none of these studies have clearly demonstrated a significant relationship between gold charge and hydrogenation /oxidation selectivity.

2.5. Conclusions

Treatment of Au/TS-1 catalysts with cyanide selectively removed small gold particles at low cyanide concentration and formed gold (+3) cyanide at high cyanide concentration. Nanoscale metallic gold was found to be active for propylene epoxidation and hydrogenation, as well as combustion of hydrogen. Larger gold particles (>4.5 nm) were less active for all reactions and had higher hydrogenation selectivity. Nanoscale gold (+1) cyanide was very active for hydrogenation, with significantly reduced hydrogen combustion and absolutely no propylene oxidation. Larger gold (+1) cyanide particles were less active for all reactions. It is hoped that the discovery will promote further studies in controlling oxidation/hydrogenation activity with gold charge.

2.6 References

[1] M. Haruta, Nature 437 (2005) 1098.

[2] G. J. Hutchings, J. Catal. 96 (1985) 292.

[3] J.K. Edwards, B. Solsona, E. Ntainjua, A.E. Carley, A.A. Herzing, C.J. Kiely, G.J. Hutchings, Science 323 (2009) 1037.

[4] A. Wittstock, V. Zielasek, J. Biener, C.M. Friend, M. Baumer, Science 15 (2010) 319.

[5] J. Lu, X. Zhang, J.J. Bravo-Suárez, S. Tsubota, J. Gaudet, S.T. Oyama, Catal. Today 123 (2007) 189

[6] J. Lu, X. Zhang, J.J. Bravo-Suárez, T. Fujitani, S.T. Oyama, Catal. Today 147 (2007) 186.

[7] J. Lu, X. Zhang, J.J. Bravo-Suárez, K.K. Bando, T. Fujitani, S.T. Oyama, J. Catal. 250 (2007) 350

[8] J.J. Bravo-Suárez, J. Lu, C.G. Dallos, T. Fujitani, S.T. Oyama, J. Phys. Chem. C 111 (2007) 17427.

[9] S.T. Oyama, X. Zhang, J. Lu, Y. Gu, T. Fujitani, J. Catal. 257 (2008) 1.

[10] J.F. Ng, Y. Nie, G.K. Chuah, S. Jaenicke, J. Catal. 269 (2009) 302.

[11] A.S.K. Hashmi, G.J. Hutchings, Angew. Chem. Int. Ed. 45 (2006) 7896.

[12] S. T. Oyama, in S.T. Oyama (Ed.), Mechanisms in Homogeneous and Heterogeneous Epoxidation, Elsevier, Amsterdam, 2008, p. 1.

[13] A.K. Sinha, S. Seelan, S. Tsubota, M. Haruta, Top. Catal. 29 (2004) 95.

[14] T. Alexander Nijhuis, T. Visser, B. M. Weckhuysen, Angew. Chem. Int. Ed. 44 (2005) 1115.

[15] E. Stangland, B. Taylor, R.P. Andres, W.N. Delgass, J. Phys. Chem. B 109 (2005) 2321.

[16] W. Cheng, X. Wang, G. Li, X. Guo, B. Du, Catal. Lett. 95 (2004) 185.

[17] X. Liu, X. Wang, X. Guo, G. Li, Catal. Today 93-95 (2004) 505.

[18] G. F. Thiele, E. Roland, J. Molec. Catal. A 117 (1997) 351.

[19] S. Bordiga, F. Bonino, C. Prestipino, A. Damin, C. Lamberti, Phys. Chem. Chem. Phys. 9 (2007) 4854.

[20] J.J. Bravo-Surez, K.K. Bando, J. Lu, M. Haruta, T. Fujitani, T. Oyama, J. Phys. Chem. C 112 (2008) 1115.

[21] J.J. Bravo-Suárez, K.K. Bando, T. Fujitani, S.T. Oyama, J. Catal. 257 (2008) 32.

[22] D.H. Wells Jr., W.N. Delgass, K.T. Thomson, J. Catal. 225 (2004) 69.

[23] A.M. Joshi, W.N. Delgass, K.T. Thomson, J. Phys. Chem. B 110 (2006) 16439.

[24] Q. Fu, W. Deng, H. Saltzburg, M. Flytzani-Stephanopoulos, Appl. Catal. B 56 (2005) 57.

[25] J.T. Calla, R.J. Davis, Catal. Lett. 99 (2005) 21.

[26] S. Tsubota, D.A.H. Cunningham, Y. Bando, M. Haruta, Stud. Surf. Sci. Catal. 91 (1995) 227.

[27] D.S. Su, T. Jacob, T.W. Hansen, D. Wang, R. Schlogl, B. Freitag, S. Kujawa, Angew. Chem. Int. Ed. 47 (2008) 5005.

[28] T. Kubota, N. Hosomi, K.K. Bando, T. Matsui, Y. Okamoto, Phys. Chem. Chem. Phys. 5 (2003) 4510.

[29] B. Ravel, M. Newville, J. Synchrotron Rad. 12 (2005) 537.

[30] K.H. Chae, S.M. Jung, Y.S. Lee, C.N. Whang, Y. Jeon, M. Croft, D. Sills, P.H. Ansari, K. Mack, Phys. Rev. B 53 (1996) 10328.

[31] Y.-S. Lee, K.-Y. Lim, Y.-D. Chung, C.-N. Whang, Y. Jeon, Surf. Interface Anal. 30 (2000) 475.

[32] G.K. Upadhyaya, G. Shah, S.N. Gupta, Physica B 208-209 (1995) 297.

[33] M. Newville, P. Livins, Y. Yacoby, E.A. Stern, J.J. Rehr, Phys. Rev. B 47 (1993) 14126.

[34] K. Asakura, in: Y. Iwasawa (Ed.), X-ray Absorption Fine Structure for Catalysts and Surfaces, World Scientific, River Edge, New Jersey, 1996, p. 34.

[35] C. Kittel, Introduction to Solid State Physics, eighth ed., John Wiley & Sons, Hoboken, New Jersey, 2005, p. 20.

[36] S.J. Hibble, A.C. Hannon, S.M. Cheyne, Inorg. Chem. 42 (2003) 4724.

[37] B. Ravel, J. Synchrotron Rad. 8 (2001) 314-316

[38] J.J. Rehr, R.C. Albers, Rev. Mod. Phys. 72 (2000) 621-654.

[39] A. L. Ankudinov, B. Ravel, J. J. Rehr, S. D. Conradson, Phys. Rev. B. 58 (1998) 7565.

[40] J. Prakash, M.P. Hemkar, J. Phys. Soc. Japan 34 (1973) 1583.

[41] E.S. Clark, D.H. Templeton, C.H. MacGillavry, Acta Cryst. 11 (1958) 284.

[42] A. Rosenzweig, D.T. Cromer, Acta Cryst. 12 (1959) 709.

[43] S.G. Kim, Y.-F. Hu, Y.M. Yiu, T.K. Sham, J. Electron. Spectrosc. Relat. Phenom. 144-147 (2005) 811.

[44] A. Pantelouris, G. Küper, J. Hormes, C. Feldmann, M. Jansen, J. Am. Chem. Soc. 117 (1995) 11749.

[45] Q. Fu, H. Saltsburg, M. Flytzani-Stephanopoulos, Science 301 (2003) 935.

[46] R.A. Penneman, E. Staritzky, L.H. Jones, J. Am. Chem. Soc. 78 (1956) 62.

[47] B. Taylor, J. Lauterbach, G.E. Blau, W.N. Delgass, J. Catal. 242 (2006) 142.

[48] D.G. Barton, S.G. Podkolzin, J. Phys. Chem. B 109 (2005) 2262.

[49] B.R. Orton, C.M. Stanton, N.A. Gulley, D.A. Vorsatz, R. Manaila-Devenyi, J. Non-Cryst. Solids 156-158 (1993) 133.

[50] F. de Groot, Coord. Chem. Rev. 249 (2005) 31.

[51] P.G. Jones, H. Rumpel, E. Schwarzmann, G.M. Sheldrick, Acta Cryst. B 35 (1979) 1435.

[52] K.H. Hallmeier, S. Sauter, R. Szargan, Inorg. Chem. Comm. 4 (2001) 153.

[53] G.A. Bowmaker, B.J. Kennedy, J.C. Reid, Inorg. Chem. 37 (1998) 3968.

[54] A.C. Hannon, Nucl. Instrum. Methods Phys. Res., Sect. A 551 (2005) 88.

[55] A. Hugon, L. Delannoy, C. Louis, Gold Bull. 41 (2008) 127.

[56] J. Lenz, B.C. Campo, M. Alvarez, M.A. Volpe, J. Catal. 267 (2009) 50.

[57] S. Naito, M. Tanimoto, J. Chem. Soc., Chem. Commun. (1998) 832.

[58] J.C. Fierro-Gonzalez, J. Guzman, B.C. Gates, Top. Catal. 44 (2007) 103.

[59] A. Abad, P. Concepción, A. Corma, H. García, Angew. Chem. Int. Ed. 44 (2005) 4069.

[60] S.A. Blankenship, A. Rokicki, J.A. Perkins, US Patent 6 936 568 (2005), to Sud-Chemie Inc.

[61] Jifei Jia, Kenta Haraki, Junko N. Kondo, Kazunari Domen, and Kenzi Tamaru, J. Phys. Chem. B 104 (2000) 11153.

[62] G. C. Bond, D. T. Thompson, Catal. Rev. Sci. Eng. 41 (1999) 319.

[63] Z.-P. Liu, C.-M. Wang, K.-N. Fan, Angew. Chem. 118 (2006) 7019.

[64] X. Zhang, H. Shi, B.-Q. Xu, Catal. Today 122 (2007) 330.

[65] J. Guzman, B.C. Gates, J. Catal. 226 (2004) 111.

[66] T. Hayashi, K. Tanaka, M. Haruta, J. Catal. 178 (1998) 566.

Chapter 3

Raman spectroscopic adsorption study of TS-1 and Au/TS-1 under propylene

3.1 Introduction

The Au/TS-1 catalytic system described in Chapter 2 has been studied extensively for propylene oxide (PO) production, with limited studies toward propane production. Several in situ spectroscopic studies have been used to investigate adsorbed species on Au/TS-1 and similar titanosilicate-supported gold catalysts such as Au/Ti-TUD, including Ti K-edge x-ray adsorption near edge spectroscopy (XANES) [1] and diffuse reflectance ultraviolet-visible absorption spectroscopy (UV-VIS) [2,3]. Raman spectroscopy (442 nm excitation) has been utilized to demonstrate the formation of a peroxide O-O band at 875 cm^{-1} when TS-1 was placed in contact with a H_2O_2/H_2O mixture [4]. However, in situ Raman spectroscopy of Au/TS-1 under gas-phase conditions similar to reaction has not previously been investigated.

The TS-1 UV-VIS spectrum is noted for high absorption in the 200-300 nm range, due primarily to a band near 220 nm [5] which is generally agreed to be a ligand-to-metal charge-transfer (LMCT) of a tetrahedral TiO_4 cluster within the silicalite framework [6]. The use of a UV excitation laser generates a more intense and complex Raman spectrum due to resonance [7], although many TS-1 features can still be seen at much lower excitation energies.

A previous in situ Raman spectroscopic study demonstrated how analysis of C-H features in the range of 3100-2800 cm^{-1} for propylene adsorbed on ZnO could be utilized to determine the adsorption mode, with the determination of an anionic C3 bonding mode over an anionic π-bonding mode [8].

In this study the excitation energy of 514.5 nm was found to be sufficient to generate TS-1 framework bands but low enough to not risk photodegredation of adsorbed alkyl hydrocarbons at the high photon flux necessary for Raman spectroscopy. A low-temperature ozone surface treatment was found to reduce surface fluorescence. Application of propylene produced an array of Raman alkene features. Although adsorbed oxygen and hydrogen were not directly observed, application of these gases resulted in reduction in intensity of these alkene features. Density functional theory (DFT) models of propylene indicated that π-adorbed propylene would be identical to gas-phase propylene, except for certain out-of-plane vibrations presenting at higher energy than gas phase propylene. The experimental Raman spectrum matched the predicted π-adsorbed propylene features more closely than the predicted gas-phase propylene features. Propylene isotherms of TS-1 and Au/TS-1 were found to conform to the Langmuir model, and experimentally-derived propylene uptake values were used to scale the intensity of a characteristic 1648 cm^{-1} C=C propylene peak to coverage of titanium.

3.2 Experimental

3.2.1 Synthesis and preparation

TS-1 support (atom Ti/Si = 1/100) and Au/TS-1 catalyst (atom Au/Ti/Si = 0.3/1/100) were synthesized in the manner described in Section 2.2.1 of this work. After

synthesis, the Au/TS-1 samples were further treated by placing each sample in a differential flow reactor (0.5 g catalyst, 5/5/5/35 cm^3_{NTP} min^{-1} $H_2/O_2/C_3H_6$), heating to 473 K over 6 h, and holding 2 h to reduce the gold.

3.2.2 Laser Raman spectroscopy

TS-1 and Au/TS-1 were analyzed using in situ laser Raman spectroscopy. The laser Raman spectrometer consisted of a reactor cell in which the sample was held, positioned so that the surface of the sample can be exposed to an excitation laser and light emitted by the sample can be captured by an optical array.

A gas delivery system consisting of mass flow controllers (Brooks 5850E and 5850C, nominal range ~1-100 cm^3_{NTP} min^{-1}) metered and mixed feed gases (hydrogen, Airgas ultra pure carrier (UPC) grade; oxygen, Airgas research grade; propylene, Airgas 99.99%; helium, Airgas UPC grade). Ozone was provided by a corona discharge ozone generator (Yanco Ozone Services OL80) attached to the oxygen feed line.

The reactor used for in situ Raman spectroscopy consisted of a quartz glass cell with ports to allow reactant gases to enter and effluent to exit. The catalyst was a powder sample that has been pressed into a 20 mm diameter self-supporting sample wafer, and was held at the end of a rod which positions the flat catalyst surface at a 45^o angle to both the excitation laser and the lenses which collect the scattered laser light. During experiments, the sample was rotated at 1500 revolutions per minute by an electric motor (Micropuma 415A, PentaPower controller) at the other end of the rod which supported the sample; this prevented localized heating by the laser and aided convection within the reactor. The reactor was surrounded by a resistance heater and a temperature probe was inserted at a point near where the catalyst sample was held, and temperature was

controlled with a RKC REX-P24 temperature controller. As the temperature probe was not in direct contact with the sample, sample temperature was measured using an infrared thermometer calibrated to the thermal emissivity of the sample (Fisher Scientific Traceable, 15-077-967). The conical body of the reactor cell was constructed of 1.5 mm thick high-temperature quartz glass, while the window which exposed the sample to the laser and the collection optics consisted of flat, circular optical glass 51 mm in diameter and 1.5 mm thick (GE 124, Thermal Glass Products) that was perpendicular to the sample and 10 mm from its surface.

Excitation light was provided by a Lexel 95 Ar-ion continuous wave laser tuned to 514.5 nm with a maximum output over 500 mW (Class IV), although all experiments were done at 100-400 mW. The laser was directed via mirrors to a SPEX 1450 Tunable Excitation Filter to removes UV plasma emissions, and then into a modified SPEX 1439 Sample Compartment to direct the beam upwards to pass through the reactor cell window and strike the catalyst sample.

After striking the sample, the scattered light (Raman and Rayleigh) was captured and collimated by a collecting lens (Thorlabs AC127-030-A1 Visible Achromatic Doublet, 12.7mm, f=30mm, BK7-SF2, f/2.4), sent through a filter to remove Rayleigh scattering (Kaiser Optical Systems SuperNotch Plus, HSPF 5380, 1.0 in.), and then to a focusing lens to focus the light onto the monochromater aperture (Thorlabs AC127-050-A1 Visible Achromatic Doublet, 12.7mm, f=50mm, BK7-SF2, f/4).

The monochromater was a SPEX 500M with electronics driven by a SPEX MSD2 controller. The light entering the aperture passed through a shutter and an adjustable width slit, and then spread onto a focusing mirror. This mirror focused the light onto a

diffraction grating, which subsequently reflected it off a collimating mirror and out the front port to the CCD. The spectrometer had a focal length is 0.5 meters and a f/4 aperture, while the diffraction grating was 110x100mm with 1200 grooves mm^{-1} and yielded wavelength dispersion of 1.6 nm mm^{-1} with 0.02 nm resolution. When properly focused the CCD was illuminated with a wavelength spread of 42.5 nm, or a Raman shift range of approximately 1400 cm^{-1}. To allow alignment of the laser, sample, and collection optics, a Metrologic HeNe laser (632.8 nm) was permanently mounted on the side port of the monochromater.

The detector was a liquid nitrogen cooled CCD head and electronics package (SPEX CCD-1024x256-OPEN-3LS, Horiba Jobin Yvon Symphony) which communicated with a PC via an Ethernet cable. The CCD chip was 26.6 x 6.7 mm and segmented into 1024 x 256 pixels, so that each pixel is 26 microns. The CCD was supported by an optical extension tube from the monochromater and by two vertical stages beneath the body of the camera, and it was focused so that the CCD chip is in the same optical plane as the entrance port.

To reduce surface fluorescence, each sample was surface-treated by exposing it to 1.5/8/40 cm^3_{NTP} min^{-1} O_3/O_2/He, heated to 473°C at 10 K min^{-1}, and held 2 h, except where indicated otherwise. The gold on the Au/TS-1 samples was activated as indicated in Section 3.2.1 prior to ozone treatment. Measurements were taken with the spectrometer aperture open 2 mm vertically and 0.2 mm horizontally. Each spectral image was made using between 3 and 30 60 second exposures, with 10 scans typical. An Excel macro was used to remove electronic noise from each spectra, average the spectra, and convert the x-axis from horizontal position (pixel) to Raman shift (cm^{-1}). This

conversion was facilitated by a calibration formula determined by the position of the doublet of a mercury vapor lamp at 577 and 579 nm. A calibration test was made by measuring the positions of 10 bands of *ortho*-MoO_3, indicating a maximum deviation from literature values [9] of ±2 cm^{-1}.

3.2.3 Computational molecular modeling

To aid in the study of the experimental results, propylene models were developed, which allowed the simulation of Raman frequencies of propylene in the gas phase and bound to a titanium site. Rough models of propylene and titanium hydroxide were generated using ACD/ChemSketch 8.17. These models were optimized and Raman frequencies generated at the B3LYP/6-311+G(d,p) level using Gaussian03 on a SGI ALTIX 3700 supercluster. Conversion between connection table format (CTF) molfile and Gaussian XYZ format, and generation of Raman spectra from Gaussian output, were facilitated using bash scripts written for this purpose.

3.2.4 Temperature programmed desorption

The TS-1 and Au/TS-1 samples were characterized using temperature programmed desorption (TPD) of hydrogen, oxygen, and propylene at 343 K, 393 K, and 443 K using a BEL-CAT-32 flow system. In a typical experiment, 35 mg of the sample was placed in a quartz tube and heated in 30 cm^3_{NTP} min^{-1} carrier gas (nitrogen for hydrogen desorption experiments, otherwise helium) to 573 K over 0.5 h and held 2 h to clean the surface. The sample was cooled to adsorption temperature, and 5% of the test gas in the carrier gas was introduced to the sample for 1 h, followed by a purge with carrier for 1 h. The samples were then heated from adsorption temperature to 800 K at a rate of 5 K min^{-1}. Gases used were propylene (Takachiho Chemical, >99.8%), oxygen

(Tomoe Shokai, >99.5%) helium (Suzuki Shokan, >99.999%) and hydrogen (Shimadzu OPGU-2100S hydrogen generator, >99.99%). A thermal conductivity detector (TCD) cell downstream of the sample was used to determine the concentration of test gas leaving the sample. The TCD cell was calibrated by flowing pure test gas and to determine a sensitivity factor SF (mV^{-1}). The area of the desorption peaks on a chart of TCD signal (mV) vs. time (s) was determined (A [=] mV s) and was converted to uptake using the sensitivity factor, the molar flowrate of the carrier (n), and the sample mass (n) in Eqn. 3.1.

$$\text{Uptake } [\mu\text{mol g}^{-1}] = (\text{Area [mV s]})\,(n\ [\mu\text{mol s}^{-1}])\,(\text{SF } [\text{mV}^{-1}])\,/\,(m\ [\text{g}]) \qquad (3.1)$$

3.2.5 Propylene uptake

Propylene uptake for TS-1 and Au/TS-1 at 343 K was also determined using a chemisorption method. In this method, 0.5 g of the sample was loaded into a quartz tube and heated in carrier gas (50 cm^3_{NTP} min^{-1} He, Airgas, ultra pure carrier grade) to 573 K over 1 h, held 1 h, and then cooled to 443 K. Propylene (Airgas, 99.99%) was injected into the reactor every 60 s in discrete pulses of 4.49 μmol while the effluent was measured with a quadrupole mass spectrometer (AMETEK Dycor MA100MF). Propylene which was not adsorbed by the sample was observed as spikes on the m/z = 41 channel, and pulses were continued until these spikes were uniform, indicating saturation of the sample. A chart of mass spectrometer signal vs. time was recorded (Dell Optiplex GX1 running LABTECH Notebook). The area of each peak was integrated (A [=] torr s) and the saturation (uniform) peaks were averaged (A_{sat}). The propylene uptake was thus

determined using Eqn. 3.2, where uptake is in μmol g-1, m is in g, and n is the number of pulses before saturation.

$$Uptake = \sum_{i=1}^{n} \left(\frac{A_{sat} - A_i}{A_{sat}} \right) \frac{4.49}{m} \qquad (3.2)$$

3.3. Results and discussion

3.3.1 Initial Raman spectroscopy

Spectroscopic analysis of TS-1 and Au/TS-1 was accomplished using a laser Raman spectrometer flow system (Fig. 3.1). Both the TS-1 and Au/TS-1 surfaces showed high degrees of fluorescence, most likely due to adsorbed water and other contaminants, resulting in an intense and sharply-sloping background which completely obscures surface features. It was determined that Au/TS-1 fluorescence could be removed by flowing 1.5/8/40 cm^3_{NTP} min^{-1} O_3/O_2/He and heating the sample to 473 K for 2 h (Fig. 3.2). The TS-1 surface could also be cleaned by this treatment, or alternatively, by flowing 10/40 cm^3_{NTP} min^{-1} O_2/He and heating the sample to 773 K for 2 h (Fig. 3.3). Either treatment results in a substantially similar TS-1 Raman spectrum, and as the Au/TS-1 surface may be irreversibly altered by heating above 473 K, the low-temperature ozone treatment was used for all further experiments of both TS-1 and Au/TS-1 to maintain consistency. For both TS-1 and Au/TS-1, silicalite framework vibrations are observed at 800 and 376 cm^{-1}, and Ti^{IV} vibrations are observed at 1135 and 980 cm^{-1} (Fig. 3.3) [10]. The 376 cm^{-1} framework feature is the strongest feature observed, but it is very wide and difficult to quantify with precision. The 1135 cm^{-1} titanium peak, however, is very sharp despite being a very weak feature. No TS-1 or

Au/TS-1 surface features were observed above 1135 cm^{-1}. Au/TS-1 surface features were very similar to TS-1, and the only noticeable effect of gold was increased background noise. Resonance Raman scattering is not observed at this excitation energy (514.5 nm) as this is far below the observed TS-1 UV-VIS adsorption energy of 220 nm [11]. Gold phonons were also not observed.

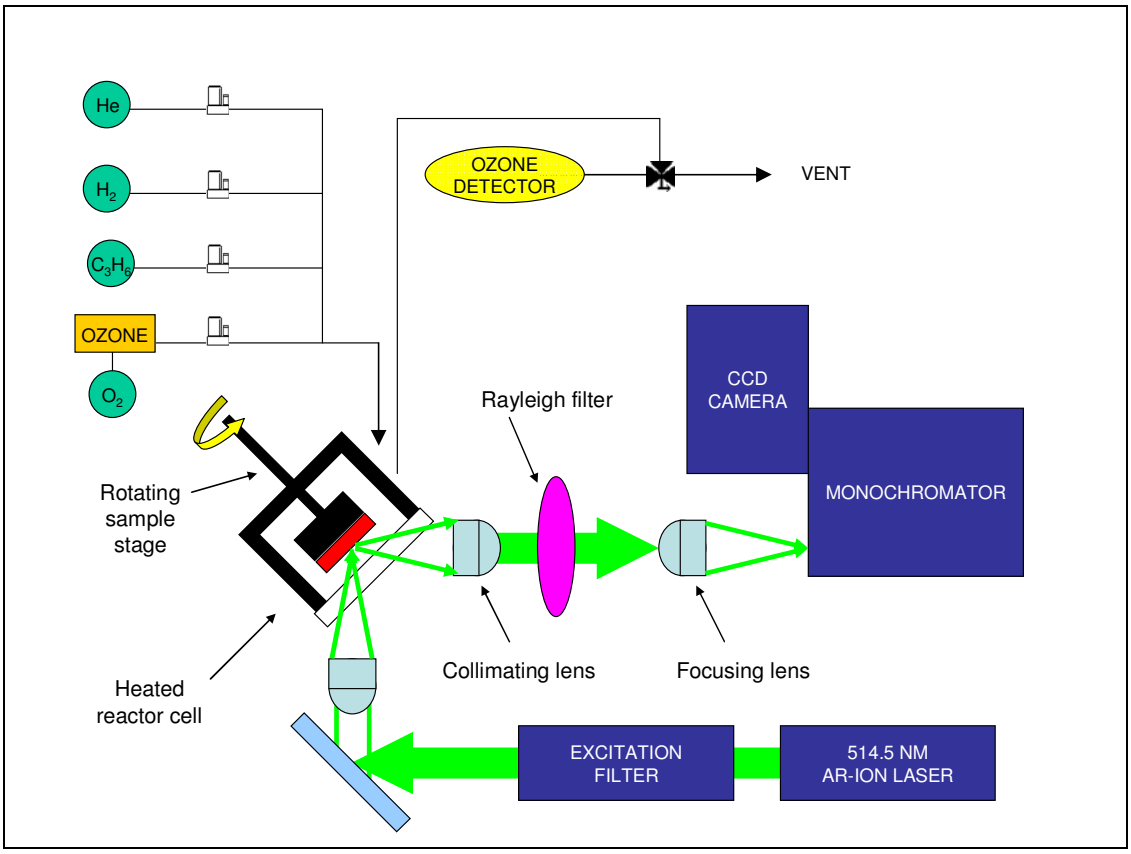

Figure 3.1. Laser Raman spectrometer diagram.

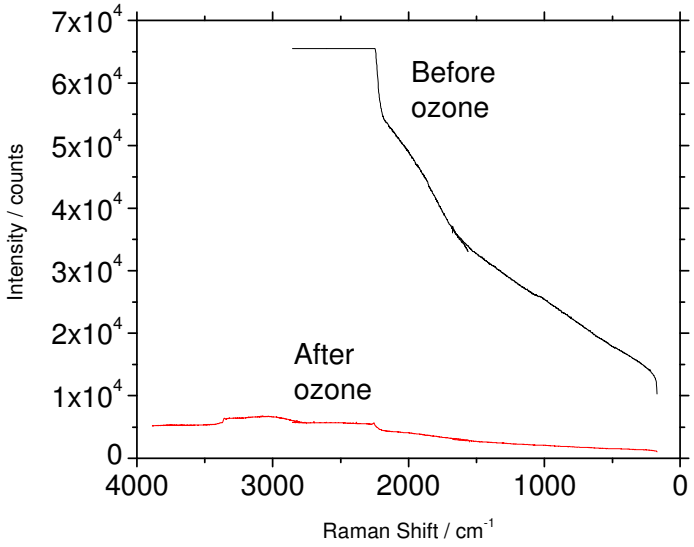

Figure 3.2. Au/TS-1 surface fluorescence at 200 mW laser intensity before before and after ozone treatment.

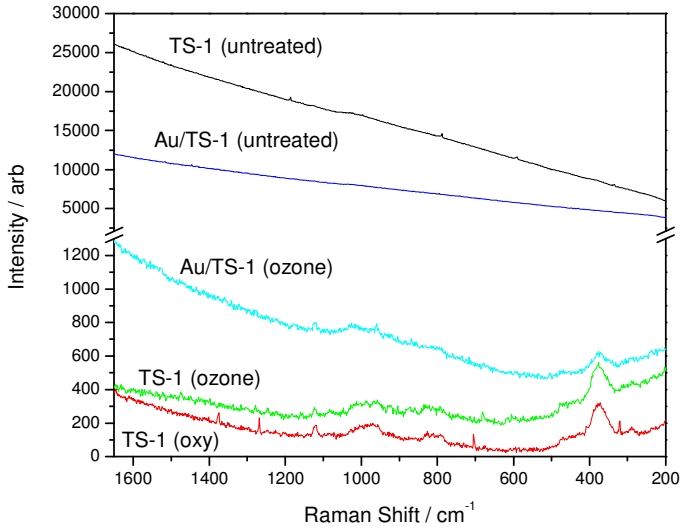

Figure 3.3. TS-1 and Au/TS-1 surfaces at 298 K, both without surface treatment (untreated) and with ozone treatment (1.5/8/40 cm^3_{NTP} min^{-1} O_3/O_2/He, 473 K). TS-1 was also exposed to high temperature oxygen treatment (10/40 cm^3_{NTP} min^{-1} O_2/He,773 K) which revealed the same surface features as ozone treatment. All spectra are given without background correction, to illustrate fluorescence of the untreated surfaces.

Raman spectra were investigated over the range of 4300 to 170 cm^{-1} by setting the monchromator to low (1700-170 cm^{-1}), intermediate (2800-1500 cm^{-1}) high (3800-2700 cm^{-1}) and very high (4300-3300 cm^{-1}) wavenumber regimes. Propylene C-H stretch features were observed at high wavenumber (3100 to 2700 cm^{-1}) while propylene C-C stretch, C-H bend, and TS-1 structural features were observed at low wavenumber (1800-200 cm^{-1}). The low wavenumber regime (Fig. 3.4, right panel) shows silicalite framework bonds indicative of S-1 and TS-1 at 800 and 376 cm^{-1} as well as Ti-O features indicative of TS-1 specifically at 1135 and 980 cm^{-1}. Propylene features are much sharper than these surface features. The strongest peak at 1648 cm^{-1} was attributed to a C=C stretch, and the feature at 918 cm^{-1} was attributed to a C-C stretch. The remaining features at 1455, 1416, 1297, and 430 cm^{-1} were attributed to C-H bending deformations. In the high-wavenumber regime (Fig. 3.4, left panel), there are no TS-1 features but many C-H stretching modes. The most energetic features at 3080 and 3012 cm^{-1} were assigned to asymmetric and symmetric CH_2 vinyl stretches. Shoulder peaks of the 3012 cm^{-1} feature at 2998 and 2980 cm^{-1} were assigned to C-H stretches of the C3 carbon. Additional features at 2917, 2885, 2853, 2818, and 2727 cm^{-1} were asymmetric and symmetric CH_3 stretches and C-H stretches of the C2 carbon [12,13]. Weak features near 3200 cm^{-1} are likely an overtone of the 1648 cm^{-1} C=C stretch.

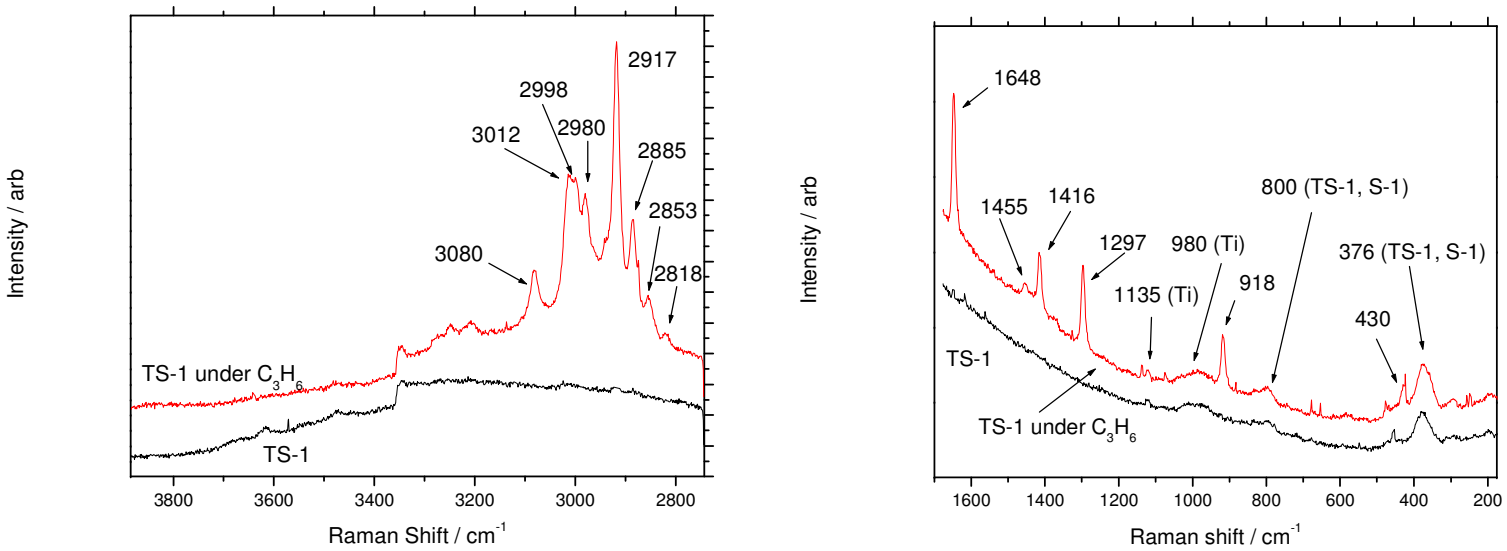

Figure 3.4. TS-1 surface at 298 K under air and propylene. Spectra are propylene features except where indicated as silicalite features (TS-1, S-1) and titanium features (Ti).

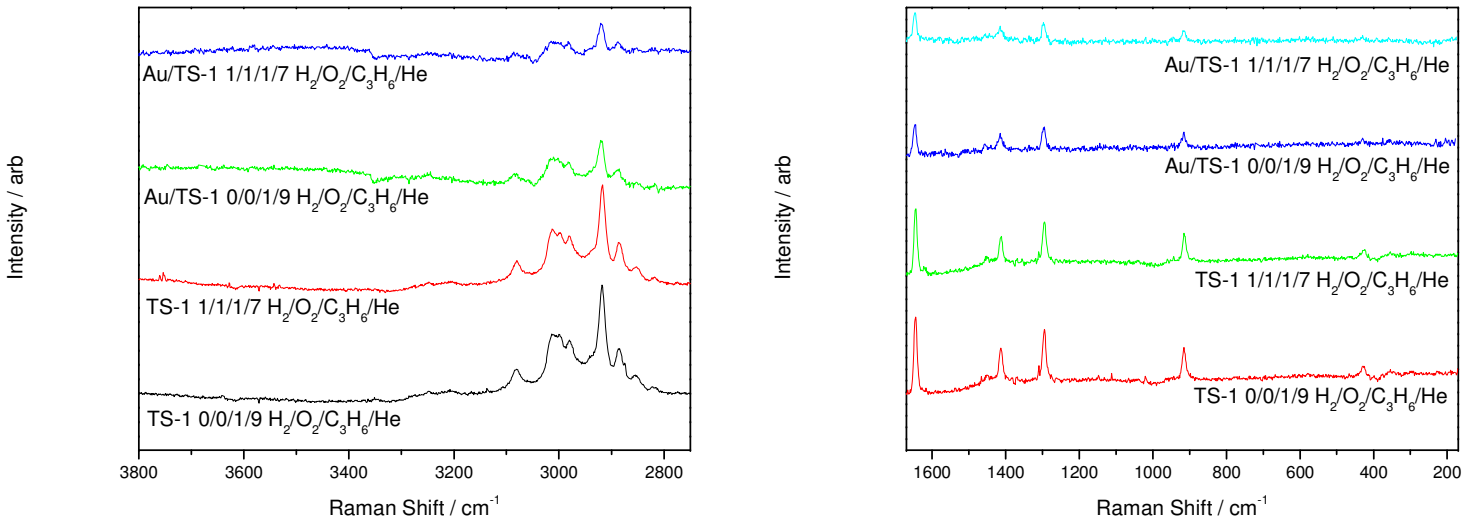

Figure 3.5. Background-subtracted Raman spectra presents stronger propylene signals under 10% C_3H_6 than 10% each H_2, O_2, and C_3H_6, on both TS-1 and Au/TS-1.

Background subtracted spectra of the TS-1 and Au/TS-1 samples (Fig. 3.5) under propylene and hydrogen/oxygen/propylene show that the addition of hydrogen and oxygen produces no new features. However, the intensity of propylene features, such as the size of the 1648 cm^{-1} C=C feature, is significantly reduced, despite the fact the partial pressure of propylene is unchanged. For TS-1, addition of hydrogen and oxygen reduces the area of the C=C feature by 18%, and for Au/TS-1 addition of hydrogen and oxygen reduces the area of the C=C feature by 34%. This reduction in C=C signal represents a proportional decrease in propylene adsorption, due to competition for adsorption sites by hydrogen and oxygen or some other reversible effect of hydrogen and oxygen on the TS-1 and Au/TS-1 surface. Although the direct observation of hydrogen and oxygen adsorbing to the surface could not be made, the reduction in propylene adsorption indicated this adsorption, as well the effect of gold increasing hydrogen and oxygen adsorption.

3.3.2 Density functional theory

Computational chemistry allows the mathematical simulation of chemical systems, which can serve as a powerful tool to predict or explain experimental results of those systems. The equations necessary to describe the electronic structure of the hydrogenic atom were Erwin Schrödinger and further formalized by Paul Dirac in the late 1926-1928; however, the direct solution of multi-electron wavefunctions is so complex that chemical properties can be modeled only by application of carefully constructed approximations [14,15].

Density functional theory (DFT), first published by Pierre Hohenberg, W. Kohn, and Lu J. Sham in 1964-1965, demonstrated that electronic models could be

tremendously simplified, yet still produce high accuracy, by approximating electronic wavefunctions in Hilbert space as electronic density in three-dimensional space, as well as isolating electron-electron interaction from other energy operators. Energy of the electronic system is expressed in terms of non-interacting kinetic energy (T_S) and coulombic pontential (J), with electron interaction accounted for using an exchange-correlation term (E_{XC}). [16]. The non-interacting terms may be easily solved, but the means by which the exchange correlation term may be solved must be selected based on the nature and purpose of the model, normally described as a "method" or "level" of computation. For this study, the Becke 3-parameter Lee-Yang-Parr (B3LYP) method was selected. The B3LYP method is a hybrid functional which comprises of a linear combination of three energy terms. An ab initio functional consisting of a partial Hartree-Fock (HF) exchange correlation functional is complemented with two semi-empirical density functional terms: a Vosko-Wilk-Nusair semi-empirical local density approximation (LDA, an energy term dependent only on electron density) [17], and a Becke, Lee-Yang-Parr general gradient approximation (GGA, an energy term dependent only on electron density gradient). The B3LYP hybrid functional is commonly used in organic systems [18].

A basis set for electron population must be selected along with a method to initiate a computation. Several of John Pople's 6-31G and 6-311G split-valence basis sets were investigated, with the 6-311+G(d,p) basis set selected for all final calculations. In this basis set, electron orbitals are constructed using primitive Gaussian-type radial functions, which are linearly combined into contracted Gaussians. The 6-311+G(d,p) is a triple-zeta valance set, where the valence electrons are described by a linear combination

of three contracted Gaussians, one of which consists of three primitive Gaussians and the other two consisting of one primitive Gaussian each. Polarization functions (d,p) allow s-orbitals to distort to p-orbitals, and p-orbitals to distort to d-orbitals, while a diffuse function (+) smooths the radial energy function for all atoms except hydrogen. The entire set of core (non-bonding) electrons are described by a single contracted Gaussian formed by six primitive Gaussians.

Several chemical models were simulated. For simplicity, the Ti center to which the propylene is assumed to adsorb is modeled as a tetravalent $Ti(OH)_4$ cluster. A total of eight propylene orientations were simulated: a single propylene molecule (C_3H_6), a propylene molecule adsorbed to $Ti(OH)_4$ at C1, C2, and C3 positions ($Ti(OH)_4$-C_3H_6 [C1], $Ti(OH)_4$-C_3H_6 [C2], $Ti(OH)_4$-C_3H_6 [C3]), a propylene molecule adsorbed to $Ti(OH)_4$ at C1, C2, and C3 positions with one hydrogen dissociated ($Ti(OH)_4$-C_3H_5 [C1], $Ti(OH)_4$-C_3H_5 [C2], $Ti(OH)_4$-C_3H_5 [C3]), and a propylene molecule adsorbed to $Ti(OH)_4$ via π bond ($Ti(OH)_4$-C_3H_6 [π]). All systems were investigated using the 6-31+G(d), 6-311+G(d), 6-311++G(d), and 6-311++G(d,p) basis sets. The $Ti(OH)_4$-C_3H_6 [C1,C2,C3] sets were unstable; however, the three dissociatively adsorbed propylene sets (C_3H_5-) were found to be stable ($Ti(OH)_4$-C_3H_5 [C1,C2,C3]). Gas-phase propylene (C_3H_6 [gas]) and π-adsorbed propylene ($Ti(OH)_4$-C_3H_6 [π]) also resolved to stable energy minima. Presented here are the predicted spectra at the B3LYP/6-311+G(d,p) level for gas-phase propylene, propylene adsorbed to $Ti(OH)_4$ along the π-bond, and, for illustration, dissociatively-adsorbed propylene adsorbed to $Ti(OH)_4$ at the C1, C2, and C3 positions. Calculated vibration energies were adjusted using an energy calibration of 0.97 [19] and

Ti-O and O-H bands were removed. Bash scripts were used to generate Raman spectra and to assist in identifying vibration modes.

As was found in the experimental results, vibrations were predicted in the range of 1800-200 cm^{-1} and C-H stretches were observed in the range of 3200-2700 cm^{-1} (Fig. 3.6). In the low-wavenumber range, the C=C feature near 1650 cm^{-1} is significantly reduced for C1 and C2 bound propylene, while for all other spectra this feature is the most intense feature in the low-wavenumber range. Further, the C3 bound propylene has a strong feature at 1020 cm^{-1} which does not appear for any other sample. The spectra for π-bound propylene, propylene gas, and the experimental results all show the same features at 1648 (carbon-carbon double bond stretch), 1416 ($C(1)H_2$ symmetric in-plane bend), 1297 (C(2)H in-plane bend), and 918 cm^{-1} (carbon-carbon single bond stretch), matching both position and relative intensities. In the high-wavenumber regime, all spectra except C1-adsorbed propylene predict the 3080 cm^{-1} feature, and only the π-adsorbed propylene and propylene gas predict the features at 3080 ($C(1)H_2$ in-plane asymmetric stretch), 3012 ($C(1)H_2$ in-plane symmetric stretch), 2998 (C(3)H out-of-plane stretch), 2980 (C(3)H out-of-plane stretch), and 2917 cm^{-1} ($C(3)H_3$ asymmetric stretch).

Three important peaks are observed for π-adsorbed and gas-phase propylene. The peaks at 2998, 2980, and 2917 cm^{-1} are the only out-of-plane features observed, and these features are shifted to higher energy when propylene is π-bound to a titanium center. All in-plane vibrations are not affected by adsorption.

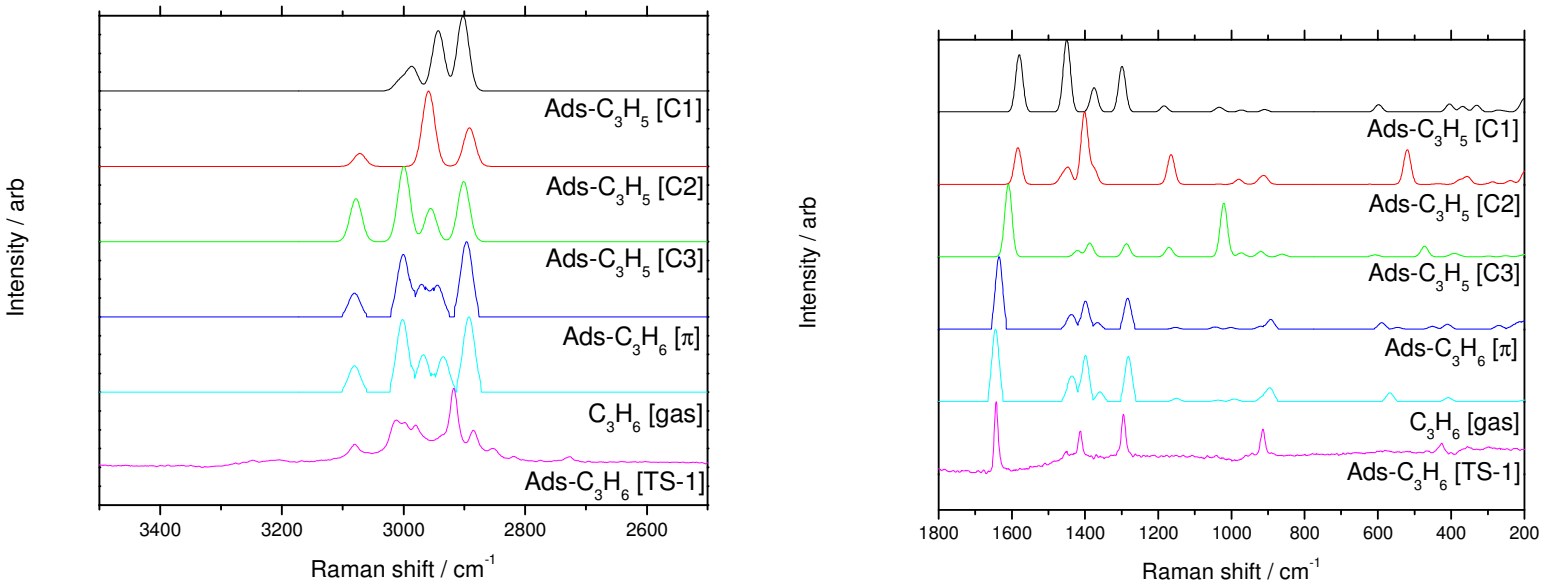

Figure 3.6: Propylene in gas phase ([gas]) and dissociated propylene (C_3H_5-) adsorbed to $Ti(OH)_4$ at C1,C2,C3 and at π bond, determined by density functional theory. Raman spectra determined experimentally (Ads-C_3H_6 [TS-1]) is most similar to π-adsorbed propylene.

3.3.3 Temperature programmed desorption and C_3H_6 uptake

Surface analysis of TS-1 and Au/TS-1 was accomplished using temperature programmed adsorption (TPD) of H_2, O_2, and C_3H_6 as well as measuring uptake of C_3H_6. At 343 K, all species are more tightly bound to Au/TS-1 than TS-1, as indicated by the higher desorption temperature (Fig. 3.7). On Au/TS-1, the propylene desorption trace at 343 K shows two peaks, indicating dual adsorption sites, most likely Ti at lower temperature and Au at higher temperature. This is not observed for H_2 or O_2, which may indicate that adsorption on gold is not activated at this temperature. Studies using Au L_{III} x-ray absorption near edge spectroscopy (XANES) have indicated that propylene may also adsorb to gold on the Au/TS-1 catalyst [20].

Integrating the TPD traces allowed calculation of adsorption, and these values were compared to adsorption determined by dosing a cleaned surface with propylene (Table 3.1). Adsorption values were presented as μmol g^{-1}. As propylene adsorption is of particular interest, this adsorption was also presented in terms of coverage of Ti sites ($\theta^{(Ti)} = N_{C3H6} / N_{Ti}$), coverage of Au sites ($\theta^{(Au)} = N_{C3H6} / N_{Au}$), and coverage of both Ti and Au sites ($\theta^{(Au+Ti)} = N_{C3H6} / (N_{Au} + N_{Au})$), with the simplifying assumption that both Ti and Au are so disperse that all atoms are active sites. Propylene coverage over titanium was determined to be 12% for TS-1 and 51% for Au/TS-1 at 343 K as determined by propylene uptake.

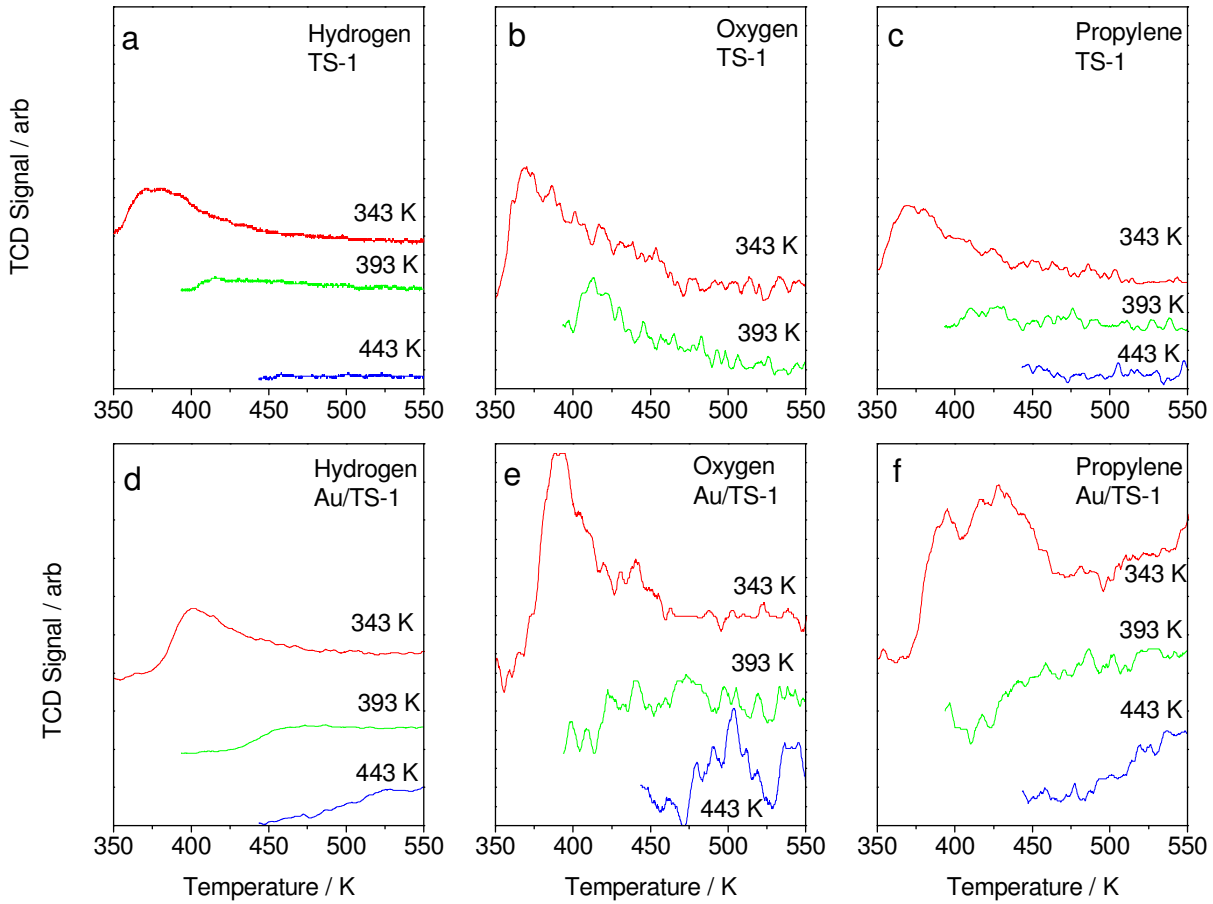

Figure 3.7. Temperature programmed desorption of TS-1 and Au/TS-1 samples at 5 K min^{-1}.

Table 3.1. The adsorption of hydrogen, oxygen, and propylene determined by temperature programmed desorption (TPD) and propylene uptake

Sample	T	Surface stoichiometry (μmol g^{-1})			Adsorption (μmol g^{-1})				C_3H_6 coverage (θ_{C3H6}) (%)					
					TPD			Uptake	TPD			Uptake		
	(K)	Ti	Au	Au+Ti	H_2	O_2	C_3H_6	C_3H_6	$\theta^{(Ti)}$	$\theta^{(Au)}$	$\theta^{(Au+Ti)}$	$\theta^{(Ti)}$	$\theta^{(Au)}$	$\theta^{(Au+Ti)}$
TS-1	343	167	-	167	16.2	47.2	14.8	20.4	9	-	9	12	-	12
	393	"	-	"	5.1	5.9	1.3	-	1	-	1	-	-	-
	443	"	-	"	0.1	0.0	0.1	-	<1	-	<1	-	-	-
Au/TS-1	343	167	51	218	18.7	54.1	67.1	84.6	40	132	31	51	167	39
	393	"	"	"	8.5	21.3	33.2	-	20	65	15	-	-	-
	443	"	"	"	7.1	16.4	18.7	-	11	37	9	-	-	-

3.3.4 Adsorption isotherms calculated by Raman spectroscopy

Using the area of the Ti peak at 1135 cm^{-1} as an internal standard, it was determined that the area of the C=C peak at 1648 cm^{-1} may be proportional to the propylene coverage θ_{PR}, as in Eqn. 3.3, where β is a constant to be determined.

$$A_{SCALE} = \frac{A_{1648}}{A_{1135}} = \frac{1}{\gamma}\frac{N_{C3H6}}{N_{Ti}} = \frac{\theta_{C3H6}}{\gamma} \qquad (3.3)$$

The sensitivity factor γ was estimated as γ=0.322, as at this value, the calculated propylene coverage θ_{C3H6} under 100% propylene at 343 K matches the measured uptake value of 51% for Au/TS-1. Applying the same sensitivity factor to TS-1 results in a coverage of 20%, which is greater than the measured uptake value of 12% of TS-1 but within the estimated uncertainty of 10%. Raman spectra of TS-1 and Au/TS-1 at 298 K and 343 K were measured at a range of propylene concentrations, and the 1648 cm^{-1} and 1135 cm^{-1} features were integrated and introduced into Eqn. 3.3 to calculate propylene coverage θ_{C3H6} for each point (Fig. 3.8). The calculated isotherms follow Langmuir profiles, indicating very little interaction of adsorption sites, most likely due to these sites being isolated titanium sites. The Langmuir isotherm is determined as detailed in Eqns. 3.4-3.8. A simple, reversible adsorption of C_3H_6 onto an empty adsorption site (*) (Eqn. 3.4) is described as two equal rates (Eqn. 3.5) which can be manipulated so that the ratio of adsorbed propylene (C_3H_6*) and empty sites (*) is equal to the gas-phase propylene concentration multiplied by an equilibrium constant K (Eqn. 3.6). Propylene coverage is described as the ratio of adsorbed propylene to the total number of sites (N_{SITES}), which is

the sum of both empty (*) and occupied (C_3H_6*) sites (Eqn. 3.7). Propylene coverage is therefore equal to a rational function of propylene gas concentration and the equilibrium constant K (Eqn. 3.8).

$$C_3H_6 + * \leftrightarrow C_3H_6 * \quad (3.4)$$

$$r_{ads} = k_1(C_3H_6)(*) = r_{des} = k_2(C_3H_6*) \quad (3.5)$$

$$\frac{k_1}{k_2}(C_3H_6) = K(C_3H_6) = \frac{(C_3H_6*)}{(*)} \quad (3.6)$$

$$\theta_{C3H6} = \frac{(C_3H_6*)}{N_{SITES}} = \frac{(C_3H_6*)}{(C_3H_6*)+(*)} = \frac{(C_3H_6*)/(*)}{(C_3H_6*)/(*)+1} \quad (3.7)$$

$$\theta_{C3H6} = \frac{K(C_3H_6)}{K(C_3H_6)+1} \quad (3.8)$$

Equation 3.8 was fit to the adsorption isotherms in Fig. 3.8 to determine the values of the equilibrium constant K. The TS-1 equilibrium constant was 85±6 at 298 K and 0.6±0.1 at 343 K, while the Au/TS-1 equilibrium constant was 71±22 at 298 K and 1.6±0.1 at 343 K. Using these values, coverage at 298 K is estimated as 99% for both TS-1 and Au/TS-1, although coverage at 343 K is significantly overestimated at 35% for TS-1 and 61% for Au/TS-1.

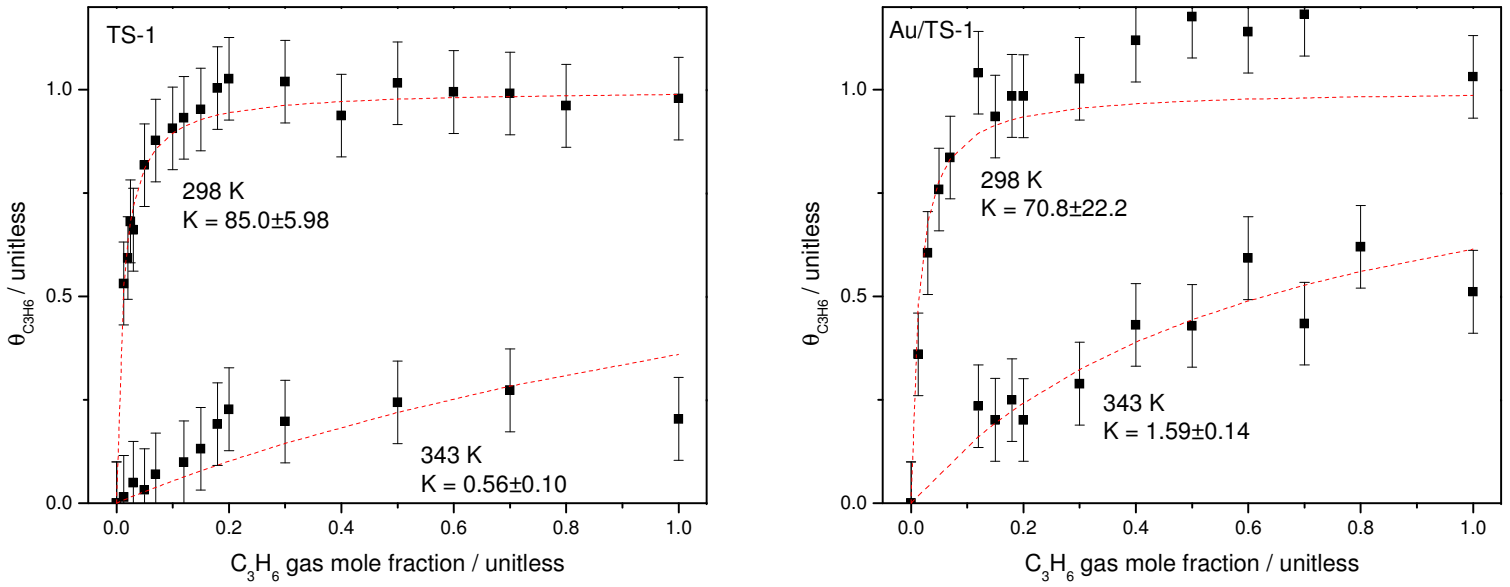

Figure 3.8. Langmuir adsorption isotherms of TS-1 (left panel) and Au/TS-1 (right panel) at 298 K and 343 K.

3.4 Conclusions

Laser Raman spectroscopy of a titanisilicate support (TS-1) and a titanosilicate-supported gold catalyst (Au/TS-1) was accomplished using a low-temperature ozone treatment to substantially reduce surface fluorescence. TS-1 framework vibrations were observed in the range of 1135-200 cm^{-1}, although no gold excitation was observed at the low excitation energy used. Propylene Raman spectra were observed at 3100-2700 cm^{-1} and 1650-430 cm^{-1}. Although adsorbed hydrogen and oxygen were not observed directly, the addition of these gases, without altering propylene partial pressure, resulted in significantly reduced intensity of the 1648 cm^{-1} propylene C=C feature.

Density functional theory (DFT) was utilized to support frequency assignments as well as provide evidence for adsorbed propylene by demonstrating a shift of out-of-plane vibrations to energies slightly higher than expected for gas-phase propylene.

Temperature programmed desorption (TPD) and propylene uptake were utilized to further characterize the surface of TS-1 and Au/TS-1. Evidence for dual-site adsorption of propylene on Au/TS-1 was indicated by a split desorption peak. Titanium uptake of propylene was determined to be 9-12% for TS-1 and 40-51% for Au/TS-1 at 343 K.

Adsorption isotherms for propylene on TS-1 and Au/TS-1 at 298 K and 343 K showed Langumir adsorption profiles. Application of an internal standard along with the experimentally-derived propylene uptake values allowed these isotherms to be described in terms of titanium coverage.

3.5 Appendix

Bash scripts used to manipulate CTF Molfile and Gaussian opt-freq data.

3.5.1 Generation of Gaussian input file from CTF Molfile

FILE: MOL2GAU.SH

A script which extracts the XYZ table from a CTF Molfile and combines it with a Gaussian input header to form a Gaussian input file

```
01 #!/bin/bash
02 ### This script converts MOL files to GAUSSIAN tables
03 ### Input format is ./molgaush "Molfile" "Gaussian input header"
04 STR1='   '
05 FILE=$1
06 GAU=$2
07 echo Combining Molfile $1 with Gaussian input header $2
08 grep "$STR1" $FILE | sed '/\(M  \)/d' | cut -c 1-34 >$FILE.1
09 cat $FILE.1 | sed 's/\(.*\)\([A-Z].*\)/\2\1/' >$FILE.2
10 cat $GAU $FILE.2 > $FILE.inp
11 rm $FILE.1 $FILE.2
12 echo $FILE.inp written.
13 exit
```

3.5.1 Updating a CTF Molfile with coordinate corrections of a Gaussian OPT-FREQ output file

FILE: Gaussian-Molfile table

A list of Gaussian output files and matching CTF Molfiles for use by gau2mol.sh

```
01 GaussianOutputFile1 CTFMolfile1
02 GaussianOutputFile2 CTFMolfile2
03 GaussianOutputFile3 CTFMolfile3
...
```

FILE: GAU2MOL.SH

A script which updates the XYZ coordinates of a CTF Molfile with the optimized geometry in a Gaussian OPT-FREQ output file using a Gaussian-Molfile table

```
01 #!/bin/bash
02 ### This script extracts a Cartesian table from a Gaussian .out file
03 ### using the freq input for an opt-freq analysis
04 ### Molfiles are connected to files using the list outfile
05 echo "GAUMOL script by Jason Gaudet."
06 echo "This script will replace the atom position table of a CTF
MOLFILE"
07 echo "with the optimized atom positions from a Gaussian opt-freq
output"
```

```
08 echo "using the Gausian - MOLFILE table in this directory."
09 read -p "Enter filename of Gaussian-Molfile table: " -e OUTFILE
10 NLINES=$(wc -l $OUTFILE | awk '{print $1}')
11 echo $OUTFILE contains $NLINES GAU-MOL file entries
12 for i in $(seq 1 $NLINES); do
13  FILE=$(cat $OUTFILE | sed -n ''$i'p' | awk '{print $1}')
14  MOL=$(cat $OUTFILE | sed -n ''$i'p' | awk '{print $2}')
15  echo Combining MOLFILE $MOL and GAUSSIAN $FILE ...
16  ###
17  ### FIRST GENERATE FORMATTED CARTESIAN BLOCK
18  ### Remove all but the block surrounding the atom table
19  cat $FILE | sed -n '/Differentiate/,/Distance/p' >$FILE.1
20  ### Remove first 7 and last 2 lines
21  cat $FILE.1 | sed '1,7d' | sed 'N;$!P;$!D;$d'>$FILE.2
22  ### Remove first 33 characters in each line
23  cat $FILE.2 | sed 's/^.\{34\}//' >$FILE.3
24  ### Round each number to 4 decimal places
25  cat $FILE.3 | perl -pe 's/\d*\.\d{5,}/sprintf"%.4f",$&/ge' >$FILE.B
26  ### $FILE.B is the properly formatted xyz table for the molfile
27  ###
28  ### NEXT GENERATE RIGHTSIDE BLOCK FROM MOLFILE
29  grep "   " $MOL | sed '/\(M  \)/d' | cut -c 31-69 >$MOL.B
30  rm $FILE.1
31  rm $FILE.2
32  rm $FILE.3
33  ### And combine rightside molfile block with leftside Gaussian
block
34  cat $MOL.B | paste -| paste $FILE.B -| tr "\t" "\n"
35  paste $FILE.B $MOL.B | sed -e 's/     //g' > $FILE.BLOCK2
36  ### NOW GENERATE START BLOCK AND END BLOCKS
37  head -4 $MOL > $FILE.BLOCK1
38  cat $MOL | sed '/[A-Z]/d' | sed '1,2d' >$FILE.BLOCK3
39  ### cat $MOL | sed -n '/\(^\)\( *[0-9]*\{7\}\)\($\)/p'
>$FILE.BLOCK3
40  cat $MOL | sed -n '/^M/p' >$FILE.BLOCK4
41  ### FINALLY, combine all blocks
42  cat $FILE.BLOCK1 $FILE.BLOCK2 $FILE.BLOCK3 $FILE.BLOCK4
>$FILE.gau.mol
43  rm $FILE.BLOCK1 $FILE.BLOCK2 $FILE.BLOCK3 $FILE.BLOCK4
44  rm $FILE.B $MOL.B
45  echo Molfile $MOL has been updated with optimized structure from
$FILE.
46  echo Optimized molfile has been saved as $FILE.gau.mol
47 done
48 exit
```

3.5.3 Generation of Raman frequency charts from Gaussian OPT-FREQ output

FILE: GAU2FREQ.SH

This script runs the input file through six compartmentalized programs with the final output of an Intensity (arb) vs. Frequency (cm-1) chart

```
01 #!/bin/bash
```

```
02 echo Running gau2freq.sh on file $1
03 echo running xltab.sh rftab.sh sftab.sh tcomb.sh tcomp.sh
cleanfreq.sh
04 echo Output will be x,y chart for $1
05 echo RUNNING XLTAB.SH TO GENERATE EXCEL TABLES
06 ./xltab.sh $1
07 echo RUNNING RFTAB.SH TO GENERATE ROUNDED FREQ AND RAMAN AREA TABLES
08 ./rftab.sh $1
09 echo RUNNING SFTAB.SH TO GENERATE NORMAL DISTRIBUTION CHARTS
10 ./sftab.sh $1
11 echo RUNNING TCOMB.SH TO COMBINE FILES INTO MULTICOLUMN FILE
12 ./tcomb.sh $1
13 echo RUNNING TCOMP.SH TO ADD UP ALL COLUMNS AND MAKE FINAL X,Y
SPECTRA
14 ./tcomp.sh $1
15 echo RUNNING CLEANFREQ.SH TO REMOVE ALL INTERMEDIATE FILES
16 ./cleanfreq.sh $1
17 echo RUN COMPLETE
18 exit
```

FILE:GVAR

This file stores the variables used in generating Raman spectra

```
01 SIGMA 10
02 XMIN 100
03 XMAX 4100
04 NSIG 2
05 GAIN 1000
06 LOFREQ 100
07 HIFREQ 4100
```

FILE: GZROUND.SH

This file rounds all non-negative numbers to the nearest integer and is used in generating Raman spectra

```
01 #!/bin/bash
02 ### gzround
03 num=$1
04  int=$(echo $num | sed 's/\..*//')
05  if [ -z $int ]
06  then
07   round=$((0))
08  else
09   dec=$(echo $num | sed 's/\(.*\.\)\([0-9]\)\(.*\)/\2/')
10   if [ "$dec" -lt "5" ];
11    then
12    round=$int
13    else
14    round=$[ $int + 1 ]
15   fi
16  fi
17 echo $round
18 exit
```

FILE: XLTAB.SH

This file extracts the frequencies and Raman activities from the Gaussian output file

into a single table

```
01 #!/bin/bash
02 ### This script generates frequency tables for the given input file
03 echo "Extracting frequencies, Raman, and IR Intensities"
04 FREQ="Frequencies --"
05 RAMA="Raman Activ --"
06 IRIN="IR Inten    --"
07 FILE=$1
08 echo file: $1
09 grep "$FREQ" <"$FILE" | tr -d '\r\n' | tr "$FREQ" '\40' >$FILE.frq
10 grep "$RAMA" <"$FILE" | tr -d '\r\n' | tr "$RAMA" '\40' >$FILE.rmn
11 grep "$IRIN" <"$FILE" | tr -d '\r\n' | tr "$IRIN" '\40' >$FILE.iai
12 cat $FILE.frq | sed 's/^/ FREQ /' >$FILE.fr1
13 cat $FILE.rmn | sed 's/^/\r\n RAMN /' >$FILE.rm1
14 cat $FILE.iai | sed 's/^/\r\n IRIN /' >$FILE.ia1
15 cat $FILE.fr1 $FILE.rm1 $FILE.ia1 > $FILE.freq
16 rm $FILE.frq $FILE.rmn $FILE.iai $FILE.fr1 $FILE.rm1 $FILE.ia1
17 echo "Job complete"
18 exit
```

FILE: RFTAB.SH

This file locates frequencies in the range of interest and creates one table of frequencies and another table of peak areas of those frequencies

```
01 #!/bin/bash
02 ### Generate frequency charts using Gaussian output
03 ### Establish math variables and input file
04 ### load global variables from file gvar
05 SIGMA=$(grep SIGMA gvar | awk '{print $2}')
06 XMIN=$(grep XMIN gvar | awk '{print $2}')
07 XMAX=$(grep XMAX gvar | awk '{print $2}')
08 NSIG=$(grep NSIG gvar | awk '{print $2}')
09 GAIN=$(grep GAIN gvar | awk '{print $2}')
10 LOFREQ=$(grep LOFREQ gvar | awk '{print $2}')
11 HIFREQ=$(grep HIFREQ gvar | awk '{print $2}')
12 OUT=$1
13 FILE=$(echo $OUT.freq)
14 echo $FILE
15 ### Make column of FREQ and RAMAN so they are easier to work with
16 grep FREQ $FILE | sed 's/\(\.[0-9]\{4\}\)/\1\n/g' | tr -d " " | tr -
d FREQ | sed '/^$/d' >$FILE.ft
17 grep RAMN $FILE | sed 's/\(\.[0-9]\{4\}\)/\1\n/g' | tr -d " " | tr -
d RAMN | sed '/^$/d' >$FILE.rt
18 NFREQ=$(wc -l $FILE.ft | awk '{print $1}')
19 echo $NFREQ frequencies identified
20 if [ -f $FILE.ftab ];
21 then
22  rm $FILE.ftab
23 fi
24 if [ -f $FILE.atab ];
25 then
26  rm $FILE.atab
27 fi
28 for i in $(seq 1 $NFREQ); do
29  MU=$(cat $FILE.ft | sed -n ''$i'p')
30  MU=$(./gzround.sh $MU)
31  RAMINT=$(cat $FILE.rt | sed -n ''$i'p')
```

```
 AREA=$(echo "scale=0; $GAIN*$RAMINT" | bc)
 AREA=$(./gzround.sh $AREA)
 if [ "$MU" -gt "$LOFREQ" ];
 then
  if [ "$MU" -lt "$HIFREQ" ];
  then
   echo Freq $MU and Intensity $AREA is number $i of $NFREQ
   echo $MU >> $FILE.ftab
   echo $AREA >> $FILE.atab
  else
   echo Freq $MU is too high and will be ignored
  fi
 else
  echo Freq $MU is too low and will be ignored
 fi
done
rm $FILE.ft $FILE.rt
echo Frequency and Area Tables complete and saved as $FILE.ftab and
$FILE.atab
exit
```

FILE: SFTAB.SH

Using the frequencies and peak areas generated in the last file,
this file generates a Normal distribution chart for each frequency

```
#!/bin/bash
### Generate frequency charts using Gaussian output
### Establish math variables and input file
SIGMA=$(grep SIGMA gvar | awk '{print $2}')
XMIN=$(grep XMIN gvar | awk '{print $2}')
XMAX=$(grep XMAX gvar | awk '{print $2}')
NSIG=$(grep NSIG gvar | awk '{print $2}')
GAIN=$(grep GAIN gvar | awk '{print $2}')
LOFREQ=$(grep LOFREQ gvar | awk '{print $2}')
HIFREQ=$(grep LOFREQ gvar | awk '{print $2}')
OUT=$1
FILE=$(echo $OUT.freq)
MINDIST=$[$NSIG*$SIGMA]
IEXP=$(echo "scale=3; -1/(2*$SIGMA^2)" | bc)
ZERO=$((0))
### Input the number of frequencies and number of areas as variables
NFREQ=$(wc -l $FILE.ftab | awk '{print $1}')
NAREA=$(wc -l $FILE.atab | awk '{print $1}')
if [ "$NFREQ" != "$NAREA" ]
then
 echo Files $FILE.ftab and $FILE.atab do not match, $NFREQ , $NAREA
else
 for i in $(seq 1 $NFREQ); do
  SAV=$(echo $FILE.$i)
  if [ -f $SAV ]
  then
   rm $FILE.$i
  fi
  MU=$(cat $FILE.ftab | sed -n ''$i'p')
  AREA=$(cat $FILE.atab | sed -n ''$i'p')
  XSTART=$(echo "scale=0; $MU-$MINDIST" | bc)
  XEND=$(echo "scale=0; $MU+$MINDIST" | bc)
  if [ "$XSTART" -lt "$XMIN" ]
```

```
34   then
35    XSTART=$XMIN
36   fi
37   if [ "$XEND" -gt "$XMAX" ]
38   then
39    XEND=$XMAX
40   fi
41   for X in $(seq $XSTART $XEND); do
42    Y=$(echo "scale=8; $AREA*e($IEXP*($X-$MU)^2)" | bc -l)
43    Y=$(./gzround.sh $Y)
44    echo "$X $Y" >> $FILE.$i
45    echo Calculated $X,$Y for Freq $MU, $i of $NFREQ
46   done
47  echo  FILE $FILE.$i COMPLETED
48  done
49 fi
50 echo Job Complete.  $i files created
51 exit
```

FILE: TCOMB.SH

Using the Normal distribution charts generated with the last file, this file aligns each table and combines them into one large multicolum table

```
01 #!/bin/bash
02 ### Generate frequency charts using Gaussian output
03 ### Establish math variables and input file
04 ### File form of *.out.freq.ftab
05 SIGMA=$(grep SIGMA gvar | awk '{print $2}')
06 XMIN=$(grep XMIN gvar | awk '{print $2}')
07 XMAX=$(grep XMAX gvar | awk '{print $2}')
08 OUT=$1
09 FILE=$(echo $OUT.freq)
10 ### Make column of FREQ and RAMAN so they are easier to work with
11 NFREQ=$(wc -l $FILE.ftab | awk '{print $1}')
12 echo $NFREQ is nfreq
13 for i in $(seq 1 $NFREQ); do
14  cat $FILE.$i | awk '{print $2}' > $FILE.b.$i
15 done
16 for i in $(seq 1 $NFREQ); do
17  if [ -f lead ]
18  then
19   rm lead
20  fi
21  if [ -f follow ]
22   then
23   rm follow
24  fi
25  XSTART=$(cat $FILE.$i | awk 'NR==1 {print $1}')
26  XEND=$(cat $FILE.$i | awk 'END {print $1}')
27  LEAD=$(echo "scale=0; $XSTART-$XMIN" | bc)
28  FOLLOW=$(echo "scale=0; $XMAX-$XEND" | bc)
29  echo lead $LEAD follow $FOLLOW xstart $XSTART xend $XEND file $i of
$NFREQ
30  for b in $(seq 1 $LEAD); do
31   echo "0" >> lead
32  done
```

```
33  for b in $(seq 1 $FOLLOW); do
34   echo "0" >> follow
35  done
36  if [ -f lead ]
37   then
38   if [ -f follow ]
39   then
40    cat lead $FILE.b.$i follow > $FILE.c.$i
41   else
42    cat lead $FILE.b.$i > $FILE.c.$i
43   fi
44  else
45   if [ -f follow ]
46   then
47    cat $FILE.b.$i follow > $FILE.c.$i
48   else
49    cat $FILE.b.$i > $FILE.c.$i
50   fi
51  fi
52  rm $FILE.b.$i
53  NL=$(wc -l $FILE.c.$i)
54  echo Written $NL
55 done
56 if [ -f lead ]
57 then
58  rm lead
59 fi
60 if [ -f follow ]
61 then
62  rm follow
63 fi
64 echo $i files processed.  Consolidating...
65 TFIL=$(ls $FILE.c.*)
66 paste $TFIL > $FILE.d
67 for i in $(seq 1 $NFREQ); do
68  rm $FILE.c.$i
69 done
70 echo Job Complete. File $FILE.d generated
71 exit
```

FILE: TCOMP.SH

Using the above multicolum table, this file adds the values of all y-columns to generate a final table of Frequency vs. Intensity

```
01 #!/bin/bash
02 ### Generate x,y freq chart using files from talign.sh
03 XMIN=$(grep XMIN gvar | awk '{print $2}')
04 XMAX=$(grep XMAX gvar | awk '{print $2}')
05 OUT=$1
06 FILE=$(echo $OUT.freq)
07 ### number of lines is
08 NLINE=$(wc -l $FILE.d | awk '{print $1}')
09 NCOL=$(cat $FILE.d | sed -n '1p' | awk '{print NF}')
10 echo nline $NLINE
11 echo ncol $NCOL
12 cat $FILE.d | awk '{x=0; for(i=1; i<=NF; i++) {x+=$i}; print x }' >
$FILE.ye
```

```
13 if [ -f $FILE.xe ]
14 then
15  rm $FILE.xe
16 fi
17 for i in $(seq $XMIN $XMAX); do
18  echo $i >> $FILE.xe
19 done
20 paste $FILE.xe $FILE.ye > $FILE.comp
21 rm $FILE.xe $FILE.ye
22 echo Job Complete.  $FILE.comp written.
23 exit
```

FILE: CLEANFREQ.SH

This file removes any intermediate files left by the previous scripts

```
01 #!/bin/bash
02 ### Generate frequency charts using Gaussian output
03 ### Establish math variables and input file
04 XMIN=$(grep XMIN gvar | awk '{print $2}')
05 XMAX=$(grep XMAX gvar | awk '{print $2}')
06 OUT=$1
07 FILE=$(echo $OUT.freq)
08 NFREQ=$(wc -l $FILE.ftab | awk '{print $1}')
09 ### Make sure the output file has the correct number of lines before
proceeding
10 REQLINE=$(echo "scale=0; $XMAX-$XMIN+1" | bc)
11 LINE=$(wc -l $FILE.comp | awk '{print $1}')
12 if [ "$REQLINE" -eq "$LINE" ]
13 then
14  for i in $(seq 1 $NFREQ); do
15   SAV=$(echo $FILE.$i)
16   if [ -f $SAV ]
17   then
18    rm $SAV
19   fi
20  done
21   SAV=$(echo $FILE.$i)
22  SAV=$(echo $FILE.d)
23  if [ -f $SAV ]
24  then
25   rm $SAV
26  fi
27  SAV=$(echo $FILE)
28  if [ -f $SAV ]
29  then
30   rm $SAV
31  fi
32  SAV=$(echo $FILE.ftab)
33  if [ -f $SAV ]
34  then
35   rm $SAV
36  fi
37  SAV=$(echo $FILE.atab)
38  if [ -f $SAV ]
39  then
40   rm $SAV
41  fi
42  echo $FILE.comp intermediate files have been cleaned up.
```

```
43 else
44  echo $FILE.comp is invalid
45 fi
46 exit
```

3.6 References

[1] J.J. Bravo-Suárez, K.K. Bando, J. Lu, M. Haruta, T. Fujitani, S.T. Oyama, J. Phys. Chem. C 112 (2008) 1115.

[2] C. Li, J. Catal. 216 (2003) 203.

[3] B. Chowdhury, J.J. Bravo- Suárez, N. Mimura, J. Lu, K.K. Bando, S. Tsubota, M. Haruta, J. Phys. Chem. B 110 (2006) 22995.

[4] S. Bordiga, A. Damin, F. Bonino, G. Ricchiardi, C. Lamberti, A. Zecchina, Angew. Chem. Int. Ed. 41 (2002) 4734.

[5] F.-Z. Zhang, X.-W. Guo, X.-S. Wang, G. Li, J.-C. Zhou, J.-Q. Yu, C. Li, Catal. Lett 72 (2001) 235.

[6] F. Bonino, A. Damin, G. Ricchiardi, M. Ricci, G. Spanò, R. D'Aloisio, A. Zecchina, C. Lamberti, C. Prestipino, S. Bordiga, J. Phys. Chem. B 108 (2004) 3573.

[7] C. Li, G. Xiong, J. Liu, P. Ying, Q. Xin, Z. Feng, J. Phys Chem. B 105 (2001) 2993.

[8] Tam T. Nguyen, Norman Sheppard, J.C.S. Chem. Comm 596 (1978) 868.

[9] L. Seguin, M. Figlarz, R. Cavagnat, J.-C. Lassegues, Spectrochim. Acta A 51 (1995) 1323.

[10] S. Bordiga, A. Damin, F. Bonino, G. Ricchiardi, A. Zecchina, R. Tagliapietra ,C. Lamberti, Phys. Chem. Chem. Phys. 5 (2003) 4390-4393.

[11] Can Li, Guang Xiong, Jianke Liu, Pinliang Ying, Qin Xin, and Zhaochi Feng, J. Phys. Chem. B 105 (2001) 2993.

[12] L.M Sverdlov, M.A. Kovner, E.P. Krainov, Vibrational Spectra of Polyatomic Models, John Wiley & Sons, New York, 1974. Translation of Kolebatel'nye Spektry Mnogoatomnykh Molekul, Moscow, 1970.

[13] George Socrates, Infrared and Raman Characteristic Group Frequencies, 3rd ed., John Wiley & Sons, New York, 2001.

[14] S. Fraga, J.M.G. de la Vega, E.S. Fraga, The Schrodinger and Riccati Equations, Springer-Verlag, Berlin, 1999.

[15] D. Shriver, P. Atkins, Inorganic Chemistry, 3rd ed., W. H. Freeman and Company, New York, 1999.

[16] W.Kohn, Rev. Mod. Phys. 71 (1999) 1253.

[17] S. H. Vosko, L. Wilk, M. Nusair, Can. J. Phys. 58 (1980) 1200.

[18] W. Koch, M.C. Holthausen, A Chemist's Guide to Density Functional Theory, Wiley-VCH, Weinheim, 2000.

[19] K.K. Irikura, R.D. Johnson III, R.N. Kacker, J. Phys. Chem. A 109 (2005) 8430.

[20] T.A. Nijhuis, E. Sacaliuc, A.M. Beale, A.M.J. van der Eerden, J.C. Schouten, B.M. Weckhuysen, J. Catal. 258 (2008) 256.

Chapter 4
Conclusions

This thesis presents studies of ethylene and propylene epoxidation catalysts, including the preparation, characterization, and activity testing of these catalysts. The main conclusions of this work are as follows:

- A model for the formation of silver clusters on oxide supports formulated in this thesis appears to accurately predict dispersion as a function of silver loading and support surface area for a range of supports.
- A surface-modified β-SiC-supported silver catalyst demonstrated ethylene oxidation activity far higher than silver on other β-SiC and α-SiC supports, but not as high as α-Al_2O_3.
- Ethylene epoxidation and total combustion rates were experimentally derived and conform to reasonable rational rate laws derived from simple Langmuir-Hinshelwood models
- Treatment of Au/TS-1 propylene epoxidation catalysts with cyanide selectively removes small particles but also produces persistent gold cyanide clusters at high cyanide concentrations.
- Larger gold particles (>4.5 nm) were more selective toward propylene hydrogenation than epoxidation, and had an overall reduced activity.
- Previous studies have shown that Au/TS-1 contains gold in a (+3) state immediately after synthesis, and the gold is reduced to a (+0) state as the gold

is heated in hydrogen and oxygen prior to reaction. X-ray absorption spectroscopy (XAS) was used to demonstrate a similar effect for nanoscale gold cyanide clusters, where were reduced from (+3) to (+1) under the same conditions.

- Nanoscale gold (+1) cyanide clusters, which have not been previously studied as a catalyst, are surprisingly active for propylene hydrogenation.
- Raman spectroscopy of the TS-1 and Au/TS-1 surfaces can be accomplished by using a surface treatment of low-temperature ozone to reduce fluorescence.
- A rich adsorption spectrum of propylene on TS-1 and Au/TS-1 can be observed using a 514.5 nm excitation laser.
- Reduction in intensity of propylene spectral features was used to demonstrate competition of hydrogen and oxygen for propylene sites.
- Density functional theory (DFT) was used to validate the adsorption of propylene by π-bond, by demonstrating increased energy of out-of-plane vibrations.
- Langmuir adsorption isotherms were observed for propylene on TS-1 and Au/TS-1, and a scaling factor derived from propylene uptake experiments allowed these isotherms to be presented in terms of propylene coverage of titanium.